A Direct Epitaxial Approach to Achieving Ultrasmall and Ultracompact III-Nitride Micro-LED Arrays

Peng Feng

The University of Sheffield

Department of Electronic and Electrical Engineering

Centre for GaN Materials and Devices

Supervisor: Professor Tao Wang

20 Oct 2022

Die Luft der Freiheit weht

Abstract

III-nitride semiconductor-based light-emitting diodes (LEDs) with a typical dimension larger than 300 μm have been widely used in indicators, lighting, large area displays, and other similar applications. With a significantly increasing demand of developing visible LEDs with a reduced dimension used in applications of smartwatches, smartphones, augmented reality (AR) and virtual reality (VR), the dimension of LEDs is required to be below 100 μm (ideally <5 μm for AR/VR) to achieve high-resolution microdisplays. These so-called 'micro-LEDs' (μLEDs) have many advantages over other display technologies. In comparison with liquid crystal displays (LCDs), μLEDs have the benefits of high resolution due to the high pixel density. The contrast ratio of μLEDs is > 1000000:1 while that of LCD is 5000:1. μLEDs also have two to three times higher luminance than OLED and better efficiency. Moreover, LCDs are non-emissive and require additional backlight units, leading to increased costs. Compared with organic LEDs (OLEDs), μLEDs have a longer lifetime around 100000 hours while the lifetime of OLEDs is around 10000 hours. The contrast ratio of OLEDs is > 10000:1, lower than μLEDs. Additionally, μLEDs also have higher brightness and more stable material properties. Because of these advantages, III-nitride-based μLEDs have attracted significant interest as the next generation of display technology.

The traditional approaches to the fabrications of μLEDs involve dry-etching processes, where sidewall damages introduced during dry-etching processes cannot be avoided, resulting in enhanced non-radiative recombination and thus reduced internal quantum efficiency (IQE). In this thesis, a special selective epitaxial overgrowth approach which we called "confined selective epitaxy" (CSE) has been developed to achieve ultrasmall, high-efficient, high-brightness and ultracompact InGaN-based μLEDs in the visible spectra region of up to red.

Chapter 4 demonstrates that green InGaN-based μLEDs with a diameter of 3.6 μm and an interpitch of 2 μm have been achieved using the CSE approach. The green μLEDs exhibit a high IQE of 28%, as measured by temperature-dependent photoluminescence (TDPL). High luminance of 10^7 cd/m^2 and high external quantum efficiency (EQE) of 6% at 515 nm have been obtained on a bare μLED array chip without any device packaging such as coating, passivation or reflector.

Chapter 5 illustrates the integration of green μLEDs and nanoporous GaN distributed Bragg reflectors (DBRs). This combination enhances the EQE of green μLEDs to 9% from 6%. The spectral line width of green μLEDs is also decreased from 31 nm to 25 nm.

Chapter 6 reports that red μLEDs with a dimension of 2 μm and an interpitch of 1.5 μm were achieved by the CSE approach. The bare red μLED array chip shows a high EQE of 1.75% and high luminance of 3.5×10^7 cd/m^2. Through a comparison with a planar LED grown under identical conditions with μLEDs, it is shown that higher indium content in the active region can be achieved by the CSE. The indium content in the active region of μLEDs is 31% while it is only 24% in a planar LED. This work provides a potentially effective approach to achieving full-colour microdisplay in the future.

Acknowledgements

Looking back on the four years of my PhD career, I have gained so many unforgettable experiences which have become the most essential treasures of my whole life. It is never easy to get a PhD degree, especially suffers the pandemic and other accidents. Fortunately, with many people' encourage and help, I finally reach the last stage of my PhD life. Many thanks for everyone who helped me in this journey.

First, I would like to thank Professor Tao Wang, who is my supervisor. Many thanks for teaching me what is the correct way to do academic research. With your selfless guidance and support on my project, I finally finish my PhD. Most importantly, with your generous help on shaping my personality, I have become a more confident and stronger man than before. I will never forget everything you help me in the past four years.

I would like to specially thank Dr. Ian Farrer who taught me so much about the XRD analyzations.

Many thanks for Dr. Jie Bai, Dr. Yuefei Cai, and Dr. Xiangyu He who helped a lot on the device fabrication and manuscript writing.

Especially, I would also like to thank my friends Mr. Chenqi Zhu, Mr. Ce Xu, Mr. Xinchi Chen, Mr. Guillem Martínez de Arriba, and Mr. Peter Fletcher. Many thanks for everyone's encourage and generous help.

At last, I want to thank my parents' mental and financial support during my PhD even whole life. When I was most vulnerable, it was your encouragement that kept me going. Words cannot express my deepest appreciate and love for both of you. Love both of you forever.

Publications

1. Fletcher, P.; Martínez de Arriba, G.; Tian, Y.; Poyiatzis, N.; Zhu, C.; ***Feng, P.***; Bai, J.; Wang, T. Optical Characterisation of InGaN-Based Microdisk Arrays with Nanoporous GaN/GaN DBRs. *Journal of Physics D: Applied Physics* **2022**, *55* (46), 464001.
2. Zhu, C.; Xu, C.; ***Feng, P.***; Chen, X.; Martínez de Arriba, G.; Bai, J.; Wang, T. A Comparison Study of InGaN/GaN Multiple Quantum Wells Grown on (111) Silicon and (0001) Sapphire Substrates under Identical Conditions. *Journal of Physics D: Applied Physics* **2022**, *55* (44), 444003.
3. Esendag, V.; ***Feng, P.***; Zhu, C.; Ni, R.; Bai, J.; Wang, T. Influence of a Two-Dimensional Growth Mode on Electrical Properties of the GaN Buffer in an AlGaN/GaN High Electron Mobility Transistor. *Materials* **2022**, *15* (17), 6043.
4. Martínez de Arriba, G.; ***Feng, P.***; Xu, C.; Zhu, C.; Bai, J.; Wang, T. Simple Approach to Mitigate the Emission Wavelength Instability of III-Nitride μLED Arrays. *ACS Photonics* **2022**, *9* (6), 2073–2078.
5. ***Feng, P.***; Xu, C.; Bai, J.; Zhu, C.; Farrer, I.; Martínez de Arriba, G.; Wang, T. A Simple Approach to Achieving Ultrasmall III-Nitride Microlight-Emitting Diodes with Red Emission. *ACS Applied Electronic Materials* **2022**, *4* (6), 2787–2792.
6. Tian, Y.; ***Feng, P.***; Zhu, C.; Chen, X.; Xu, C.; Esendag, V.; Martínez de Arriba, G.; Wang, T. Nearly Lattice-Matched GaN Distributed Bragg Reflectors with Enhanced Performance. *Materials* **2022**, *15* (10), 3536.

7. Esendag, V.; Bai, J.; Fletcher, P.; ***Feng, P.***; Zhu, C.; Cai, Y.; Wang, T. Investigation of Electrical Properties of InGaN-Based Micro-Light-Emitting Diode Arrays Achieved by Direct Epitaxy. *physica status solidi (a)* **2021**, *218* (24), 2100474.
8. Cai, Y.; Zhu, C.; Zhong, W.; ***Feng, P.***; Jiang, S.; Wang, T. Monolithically Integrated μLEDs/HEMTs Microdisplay on a Single Chip by a Direct Epitaxial Approach. *Advanced Materials Technologies* **2021**, *6* (6), 2100214.
9. Cai, Y.; Haggar, J. I. H.; Zhu, C.; ***Feng, P.***; Bai, J.; Wang, T. Direct Epitaxial Approach to Achieve a Monolithic On-Chip Integration of a HEMT and a Single Micro-LED with a High-Modulation Bandwidth. *ACS Applied Electronic Materials* **2021**, *3* (1), 445–450.
10. Coulon, P.-M.; ***Feng, P.***; Wang, T.; Shields, P. Impact of Inductively Coupled Plasma Etching Conditions on the Formation of Semi-Polar (11-22) and Non-Polar (11-20) GaN Nanorods. *Nanomaterials* **2020**, *10* (12), 2562.
11. Zhao, X.; Huang, K.; Bruckbauer, J.; Shen, S.; Zhu, C.; Fletcher, P.; ***Feng, P.***; Cai, Y.; Bai, J.; Trager-Cowan, C.; Martin, R. W.; Wang, T. Influence of an InGaN Superlattice Pre-Layer on the Performance of Semi-Polar (11–22) Green LEDs Grown on Silicon. *Scientific Reports* **2020**, *10* (1).
12. Bai, J.; Cai, Y.; ***Feng, P.***; Fletcher, P.; Zhu, C.; Tian, Y.; Wang, T. Ultrasmall, Ultracompact and Ultrahigh Efficient InGaN Micro Light Emitting Diodes (μLEDs) with Narrow Spectral Line Width. *ACS Nano* **2020**, *14* (6), 6906–6911.

13. Coulon, P.-M.; ***Feng, P.***; Damilano, B.; Vézian, S.; Wang, T.; Shields, P. A. Influence of the Reactor Environment on the Selective Area Thermal Etching of GaN Nanohole Arrays. *Scientific Reports* **2020**, *10* (1).
14. Jiang, S.; Cai, Y.; ***Feng, P.***; Shen, S.; Zhao, X.; Fletcher, P.; Esendag, V.; Lee, K.-B.; Wang, T. Exploring an Approach toward the Intrinsic Limits of GaN Electronics. *ACS Applied Materials & Interfaces* **2020**, *12* (11), 12949–12954.
15. Bai, J.; Cai, Y.; ***Feng, P.***; Fletcher, P.; Zhao, X.; Zhu, C.; Wang, T. A Direct Epitaxial Approach to Achieving Ultrasmall and Ultrabright InGaN Micro Light-Emitting Diodes (μLEDs). *ACS Photonics* **2020**, *7* (2), 411–415.

Contents

Chapter 7 Conclusion and Future Work 131

Chapter 1

Introduction

III-nitride semiconductors consist of aluminium nitride (AlN), gallium nitride (GaN), indium nitride (InN) and their alloys, which are all direct bandgap semiconductors. Because of the wide bandgap range, a broad spectral range from ultraviolet (UV) to infrared radiation (IR) can be covered by the ternary alloys of aluminium gallium nitride (AlGaN) and indium gallium nitride (InGaN).[1] III-nitride semiconductors have many advantages compared with other semiconductors, such as silicon (Si) and gallium arsenide (GaAs). For instance, III-nitride semiconductors have high breakdown voltage, high frequency, and high working temperatures.[2] Consequently, III-nitride semiconductors have attracted significant research interest in the application of optoelectronics, including LEDs, laser diodes (LDs), photodetectors (PDs) and high electron mobility transistors (HEMTs). It is well worth noting that the 2014 Nobel Prize in Physics was awarded to Isamu Akasaki, Hiroshi Amano and Shuji Nakamura for the invention of high-efficiency III-nitride-based blue LEDs.[3]

1.1 History of III-Nitrides

In 1932, Johnson et al. achieved the first synthetic powder GaN by flowing ammonia (NH_3) into hot liquid metallic gallium.[4] Although only tiny amounts of GaN were synthesised through this method, it demonstrated that GaN material was an extremely stable compound semiconductor by investigating the physical and chemical properties. A new research field was thus established, and in 1969, single-crystal GaN film was first synthesised on sapphire substrates by Maruska and Tietjen through Hydride Vapour Phase Epitaxy (HVPE) technology.[5] In their research, gallium monochloride (GaCl) was used as the gallium source, and NH_3 was used as the nitrogen source. However, the Hall coefficient and resistivity measurements indicated that the undoped

GaN film achieved was n-type doped. The doping concentration was between 1×10^{19} cm^{-3} and 5×10^{19} cm^{-3}, and the room temperature electron mobility was as high as 150 cm^2/V sec.[5] The high density of native nitrogen-vacancy defects is one potential explanation for this phenomenon.

In 1971, Manasevit et al. first reported a GaN thin film achieved by metal–organic chemical vapour deposition (MOCVD) technology.[6] In this experiment, trimethylgallium (TMGa) and NH_3 were used as gallium source and nitrogen source, respectively. The mixture was heated to 925–975 °C in the reactor and formed a 6 μm single-crystal GaN film with a growth rate of 100 nm/min on a sapphire substrate.[6] Similarly to Maruska's results, the undoped 6 μm GaN film achieved was also n-type GaN. Van der Pauw measurements determined an n-type doping concentration of more than 10^{19} cm^{-3}.[6] This work extended the MOCVD technology to the III-nitride semiconductor area, and this technology became an essential growth tool for GaN films in the following decades.

To enhance the quality of GaN films, in 1986, Amano et al. demonstrated a two-step growth technique to first achieve GaN thin films with a smooth surface (mirror-like) and improved crystal quality by MOCVD.[7] In this approach, a thin low-temperature AlN film was initially grown on a sapphire substrate as a buffer layer, followed by a 4 μm high-temperature GaN layer. Then, in 1991, Shuji Nakamura used a low-temperature GaN buffer layer, also commonly known as the 'nucleation layer', to replace the low-temperature AlN buffer layer and thereby further improve the crystal quality of GaN film.[8] The sample with a GaN buffer layer showed a carrier concentration of 4×10^{16} cm^{-3} at room temperature, which was lower than that of the GaN grown on an AlN buffer (around $2 - 5 \times 10^{17}$ cm^{-3}).[8] The full width at half maximum (FWHM) of the X-ray diffraction rocking curve (XRC) measurement for the GaN on an AlN buffer was 1.9 minutes, but only 1.6 minutes for the GaN grown on a GaN buffer, indicating enhanced crystal quality due to the GaN buffer.[8]

1.2 Development of III-Nitride-Based Light-Emitting Diodes

The global economy has developed rapidly since the second industrial revolution. This growth has benefited from the widespread use of fossil fuels such as oil, coal and natural gas. However, with the rise of human living standards and increasing energy demand, fossil fuels, being a non-renewable energy source, will inevitably be exhausted. In addition, carbon dioxide, sulphur dioxide and other gases produced in the process of fossil fuel combustion will also have a profoundly negative impact on the environment, leading to global warming and climate change. One effective method to overcome the impending energy crisis and improve environmental quality is to enhance energy utilisation efficiency.

Lighting is one of the most essential energy applications in human activities, consuming some 20% of total electricity consumption.[9] To reduce energy consumption, solid-state lighting, like III-nitride-based LEDs, has been developed. Compared with incandescent lamps and fluorescent lamps, III-nitride-based LEDs have the advantages of high durability, long lifetime, low power consumption and low heat generation, leading to increased energy efficiency.[10] However, there are still many challenges in the development of LEDs in terms of efficiency, the ‘green gap’, etc. Therefore, further improvement of III-nitride-based LEDs is imperative.

The development of III-nitride-based LEDs can be tracked back to 1971. Pankove first illustrated the III-nitride-based blue metal-insulator-semiconductor (MIS)-type LEDs instead of p–n junction LEDs due to the difficulty in synthesising p-type GaN at that time.[11] However, the efficiency of MIS-LEDs was limited to 0.03%.[11] Therefore, the III-nitride-based MIS-LEDs were not widely manufactured or commercialised. The synthesis of p-type GaN is an exciting breakthrough in the development of III-nitride-based LEDs.

The low-energy electron beam irradiation (LEEBI) treatment was first involved in Zn-doped GaN in 1988 by Amano et al.[12] After the LEEBI treatment, the photoluminescence (PL) intensity of Zn-doped GaN was significantly increased, but the p-type performance was still not observed. Then, Amano et al. creatively doped magnesium (Mg) into GaN to form p-type GaN in 1989.[13] A 500 nm Mg-doped GaN film demonstrated a resistivity of 35 Ω·cm, a hole concentration of 2×10^{16} cm^{-3}, and mobility of 8 $cm^2/V \cdot s$ after LEEBI treatment, while the resistivity of the as-grown sample was as high as 10^8 Ω·cm.[13] Through this method, researchers realised that the LEEBI treatment could activate the Mg-doped GaN. Unfortunately, only the top surface of Mg-doped GaN film can be activated via LEEBI treatment, thus limiting the electronic performance.

Then, in 1992, the thermal annealing method was shown to be effective for p-GaN activation. Nakamura et al. illustrated that after thermal annealing under 700℃ in nitrogen ambient, the Mg-doped GaN film obtained a low resistivity of 2 Ω·cm, a high hole concentration of 3×10^{17} cm^{-3}, and high mobility of 10 $cm^2/V \cdot s$.[14] Most importantly, the entire p-GaN layer was totally activated, rather than a limited shadow area as via the LEEBI method. Therefore, thermal annealing technology has become a common operation for p-GaN activation in the fabrication of III-nitride-based LEDs.

Benefiting from the advancement of p-GaN, the first p-GaN/n-InGaN/n-GaN double heterostructure (DH) blue (440 nm) LEDs with an external quantum efficiency (EQE) of 0.22% were reported by Nakamura et al. in 1993.[15] The output power of 125 μW at an injection current of 20 mA was twice as high as that of conventional II–VI blue LEDs.[15] The first green and yellow DH LEDs were discovered in 1995. The III-nitride-based green LEDs with an emission wavelength of 525 nm in this work showed a high EQE of 2.1% and high luminous intensity of 4 cd.[16]

In the following decades, the involvement of multi-quantum wells (MQWs), electron block layer (EBL), and patterned sapphire substrate (PSS) significantly enhanced the performance of III-nitride-based LEDs even further.[17–19] As a result, the peak EQE of blue LEDs was enhanced as high as 70%.[20] However, the EQE of long-wavelength III-nitride-based LEDs, such as green LEDs, remained limited due to the quantum-confined Stark effect (QCSE). Thus, there is a need to improve long-wavelength III-nitride-based LEDs.

Toshiba Corporation conducted a great deal of research into this area in the early 21st century. In 2012, Shioda et al. reported an MQWs structure with an AlGaN interlayer, demonstrating an enhanced EQE of 25.4% for 532 nm green LEDs.[21] The optimisation of AlGaN composition and thickness was reported in this work as well. Additionally, Hashimoto et al. employed a high-temperature GaN barrier combined with an AlGaN interlayer, achieving a high EQE of 19.3% for 570 nm yellow LEDs in 2014.[22] In the same year, Hwang et al. demonstrated 639 nm red LEDs with $Al_{0.90}Ga_{0.10}N$ interlayer, showing a high EQE of 2.9%.[23] All these works were funded by Toshiba Corporation and aroused research interest in long-wavelength III-nitride-based LEDs. Furthermore, the involvement of the AlGaN interlayer has become an effective and necessary technique for achieving long-wavelength III-nitride-based LEDs.

1.3 Development of III-Nitride-Based Micro-LEDs

The concept of micro light-emitting diodes (micro-LEDs, or μLEDs) was first demonstrated by Jin et al. in 2000.[24] The structure and SEM image of the first micro-LEDs in the world is illustrated in Figure 1.1a and Figure1.1b. In their research, III-nitride-based μLEDs with a dimension of 12 μm and an interpitch of 50 μm were fabricated, achieving 408 nm blue emission.[24] Compared with conventional 240 μm × 240 μm LEDs, μLEDs showed enhanced quantum efficiency per unit area. This paper claimed that this phenomenon might be an inherent attribute of μLEDs because of the micro size effect and the enhanced injection current usage efficiency.. After that, a large number of researchers were involved in the development of micro-LEDs. The number of publications related to ‘micro-LEDs’ and ‘μLEDs’ from the last two decades in Google Search is illustrated in Figure 1.1c, which shows a significantly increased trend for the development of μLEDs.

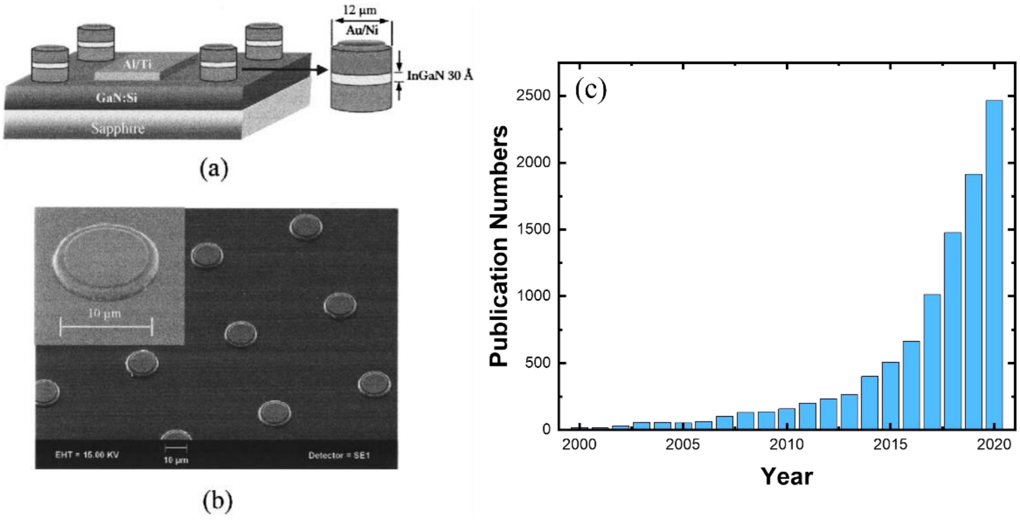

Figure 1.1. *(a) The schematic diagram of 1st micro-LEDs, (b) the SEM image of 1st micro-LEDs, and (c) the number of publications related to micro-LEDs from 2000 to 2020.*

Tian et al. initially introduced the size-dependent electrical and optical performance of μLEDs in 2012, where μLED devices with dimensions from 6 μm to 105 μm were fabricated to make a comparison.[25] With the reduction of the diameter of μLED pixels, the peak EQE was dramatically decreased. The primary mechanism of this phenomenon is the sidewall damage introduced during the ICP dry-etching processes. The ratio of the sidewall area to the LED active area is increased with the reduction of μLED dimension, leading to enhanced non-radiative recombination. The increase of non-radiative recombination can dramatically reduce IQE.[25] Tian also showed that an increase in thermal annealing time from 2 minutes to 3 minutes could significantly reduce the effect of the sidewall damage while slightly increasing the external quantum efficiency (EQE).[25] The peak EQE of 6 μm μLEDs with 3 minutes of thermal annealing was 30% higher than that with 2 minutes of thermal annealing. This was also the first reported passivation treatment in the fabrication of μLEDs. However, because the enhancement achieved by this technique is relatively minor, it is not widely used in the μLED fabrication process.

To effectively reduce the influence of sidewall damage, SiO_2 sidewall passivation has been developed. Chen et al. showed that the optical and electrical performance of μLEDs was enhanced by using SiO_2 sidewall passivation deposited by plasma-enhanced chemical vapour deposition (PECVD) in 2015.[26] In 2018, Wong et al. used advanced atomic layer deposition (ALD) technology to deposit SiO_2 on the sidewall of μLEDs for passivation, thereby achieving enhanced EL characteristics.[27] Their research compared μLEDs without passivation (LED-1), μLEDs with ALD passivation and inductively coupled plasma (ICP) etching (LED-2), μLEDs with PECVD deposition and HF etching (LED-3), and μLEDs with ALD passivation and HF etching (LED-4). For each type of μLEDs, the dimensions were designed from 10 μm to 100 μm. As shown in Figure 1.2, after the ALD passivation, the ICP etching used for the fabrication of the contact windows caused extra damage to the indium tin oxide (ITO), leading to increased current leakage density. While using HF to etch the contact area, the ITO surface was still smooth, generating higher light output power. Meanwhile, the SiO_2 deposited by PECVD had worse material quality than that of SiO_2 deposited by ALD. Additionally, when the size was reduced to 60 μm × 60 μm, the SiO_2 passivated by PECVD could not further reduce current leakage. The μLEDs with ALD passivation and HF etching also displayed the highest EQE of 33%, whereas the μLEDs without passivation was only 24%.[27]

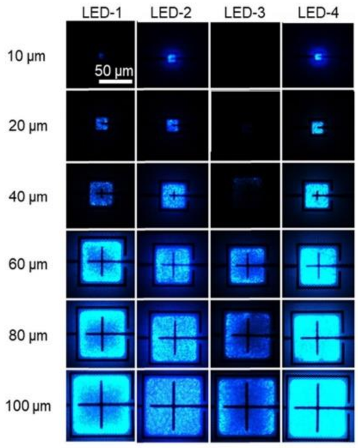

Figure 1.2. *EL images of micro-LEDs with different sizes, sidewall passivation and etching technologies.*

Although ALD passivation can enhance the optical performance of μLEDs, the sidewall damages still cannot be entirely eliminated. Our group has invented a confined selective epitaxy approach to achieve μLEDs with a dimension of less than 5 μm.[28–30] This approach does not employ any ICP dry-etching processes in the formation of μLEDs, which entirely avoids the sidewall damages and achieves high-efficiency μLEDs.

One of the challenges of μLEDs is current crowding, which further exacerbates efficiency droop.[25,27] Tian et al. discussed this phenomenon in 2012 and found that the μLEDs with smaller dimensions showed better current spreading.[25] In 2018, Konoplev et al. further discussed the relationship between current crowding and the dimension of LEDs.[31] In this research, two flip-chip LEDs were designed with dimensions of 300 μm and 30 μm, respectively. The n-electrode was placed in the centre of the LED pixel. According to the simulation results, at an injection current of 16 mA/cm^2, the current densities of both LEDs were mainly distributed near the n-electrode.[31] It is worth highlighting that the 30 μm μLEDs showed better current uniformity than conventional broad-area LEDs. This research gave further evidence that the reduction of LED dimensions could dramatically reduce current crowding.

To further enhance the current spreading in μLEDs, a tunnel junction was employed in the μLED structure in 2017 by Hwang et al.[32] The tunnel junction was formed by a combination of 17 nm high-doped p-GaN and 10 nm high-doped n-GaN, following a 400 nm n-GaN current-spreading layer, and a 10 nm high-doped n-GaN contact layer as illustrated in Figure 1.3.[32] In theory, the electrons in the valence band of high-doped p-GaN can tunnel to the conduction band of high-doped n-GaN, and the current uniformity is enhanced via the current-spreading layer. This technology can effectively improve EQE performance. However, due to the increase in resistance, the threshold voltage increases significantly as well.

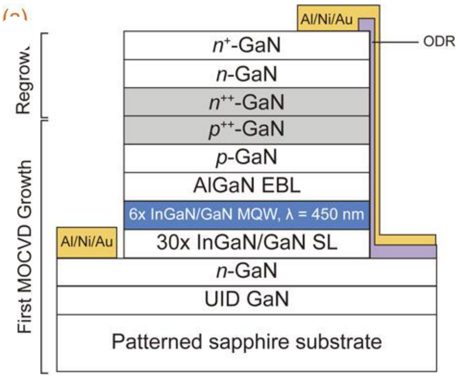

Figure 1.3. *The structure of tunnel junction LED.*

In the same year (2017), Olivier reported an effective method to improve current-spreading.[33] Firstly, a softer plasma was involved during the fabrication processes of p-contact and hybridisation pad connection. The p-contact was also fabricated with higher reflectivity and lower resistance. These improvements successfully improve current spreading, leading to higher peak EQE value and lower efficiency droop.[33]

The enhancement of extraction efficiency is also a challenge for μLEDs. A flip-chip design had already been used in 2001 for the fabrication of μLEDs to enhance extraction efficiency and has since become a common technique in the fabrication of μLEDs.[34] Choi et al. demonstrated a micro-ring-LED, which also potentially enhances extraction efficiency.[35] In theory, the micro-ring design can allow more light to emit from the sidewall to enhance the extraction efficiency. Nevertheless, the sidewall damage area was also increased, leading to increased non-radiative recombination and greater efficiency loss.

In 2004, micro-lenses were integrated with μLEDs to enhance extraction efficiency.[36] First, a 7 μm-thick photoresist was coated on the polished backside of sapphire. Then, through photolithography, only the photoresist on the back of the μLED pixels was retained. Next, the sample was heated to form spherical caps using the thermal reflow method. Finally, through ICP etching, the spherical pattern is transferred to the sapphire, and micro-lenses are thus formed.

Another technology reported in 2019 can also increase extraction efficiency. Tan et al. compared flat, concave, and various concave–convex sidewalls with different radii. Both experimental results and FDTD simulation results showed that the 2 μm radius concave–convex sidewall structure could effectively enhance extraction efficiency.[37] However, this operation can also involve more sidewall damage. Furthermore, this sidewall structure would be very difficult to fabricate for μLEDs with ultrasmall dimensions.

Finally, in 2018, Hong et al. reported that the employment of ZnO nanorods on the backside of μLEDs could effectively enhance light output power by 16.0% and EQE by 16.4% due to the reduction of total internal reflection.[38] Thus, a reflector below a μLED can enhance efficiency. Our group integrated nanoporous DBR with μLEDs in 2020, enhancing the peak EQE from 6% to 9% and the spectral line width is reduced from 31 nm t 25 nm.[29]

1.4 Motivation and Aims

Today, III-nitride-based LEDs have significantly improved solid-state lighting and are gradually replacing traditional lighting sources such as fluorescent lamps. In display applications, unlike LCDs or OLEDs, LEDs have the advantages of high efficiency, low power consumption, high brightness and long lifetime, making LEDs an ideal display technology. LEDs are also self-emission devices without any backlight, leading to high flexibility and low manufacturing cost. With the size reduction of portable and wearable devices such as AR/VR, smartphones and smartwatches, display technology must meet the criteria of high resolution, high brightness, lower power cost, and longer lifetime. Thus, III-nitride-based μLEDs have been developed for micro-displays to overtake the state of the art.

However, the efficiency of μLEDs remains very low due to the sidewall damages of μLED pixels during the dry-etching processes, leading to enhanced non-radiative recombination. To eliminate these damages, ultrasmall (less than 5 μm), high brightness, and high-efficient μLEDs achieved using confined selective epitaxy have been demonstrated in this PhD thesis. Additionally, red LEDs still currently rely on AlGaInP semiconductors. When they are fabricated into μLEDs by the traditional etch-down process, efficiency decreases dramatically. Thus, III-nitride-based red μLEDs with high efficiency (peak EQE ~ 1.75%) and ultrasmall (2 μm) dimension are also developed in this thesis.

1.5 Thesis Organisation

This thesis is organised into seven chapters.

Chapter 1 presents a brief introduction to III-nitrides, including the history and development of III-nitride-based materials, LEDs, and μLEDs. The motivation and aims are also introduced in this chapter.

Chapter 2 introduces the physical background of semiconductors. III-nitride-based optoelectronics are described as well.

Chapter 3 illustrates all experimental equipment used in this project. In terms of fabrication technology, plasma-enhanced chemical vapor deposition (PECVD), photolithography and ICP-RIE are introduced. Then, MOCVD is described as the key growth technology. The characterization technology, including the Normarski microscope, high-resolution X-ray diffraction (HRXRD), PL, scanning electron microscope (SEM) and electroluminescence (EL), are briefly presented.

Chapter 4 demonstrates green μLEDs with a diameter of 3.6 μm and an interpitch of 2 μm achieved by confined selective epitaxy. In this work, I did the growth of n-GaN on sapphire, the CSE of μLEDs, the PL, XRD and SEM measurements and analysed. The μLEDs template fabrication, device fabrication and EL measurements are done by Dr. Jie Bai and Dr, Yuefei Cai.

Chapter 5 demonstrates green µLEDs with enhanced EQE and narrow spectral line width achieved by a combination of confined selective epitaxy and nanoporous DBRs. In this work, I did the growth and analyse of DBR template, the CSE of µLEDs, the PL, XRD and SEM measurements. Dr. Jie Bai and Dr. Yuefei Cai fabricated the µLEDs templates and µLEDs devices and did the EL measurements. The EC caching was done by Dr. Jie Bai and Mr. Ye Tian.

Chapter 6 demonstrates red µLEDs with a diameter of 2 µm and an interpitch of 1.5 µm achieved by confined selective epitaxy. In this work, the growth of n-GaN on sapphire, the CSE of µLEDs, the XRD and SEM measurements were done by me. Dr, Ian Farrer provided advise on the XRD measurements. Dr, Jie Bai and Mr. Guillem Martínez de Arriba fabricated the µLEDs templates and µLEDs devices and did the EL measurements.

Chapter 7 provides the conclusion and proposes future work.

Reference

1. Arteev, D. S.; Sakharov, A. V.; Zavarin, E. E.; Lundin, W. V.; Smirnov, A. N.; Davydov, V. Y.; Yagovkina, M. A.; Usov, S. O.; Tsatsulnikov, A. F. Investigation of Statistical Broadening in InGaN Alloys. *Journal of Physics: Conference Series* **2018**, *1135*, 012050.

2. Ahi, K. Review of GaN-Based Devices for Terahertz Operation. *Optical Engineering* **2017**, 56 (09), 1.

3. The Nobel Prize in Physics 2014 https://www.nobelprize.org/prizes/physics/2014/press-release/.

4. Johnson, W. C.; Parson, J. B.; Crew, M. C. Nitrogen compounds of gallium. iii. *The journal of physical chemistry* **1993**, *36*(10), 2651-2654.

5. Maruska, H. P.; Tietjen, J. J. THE PREPARATION and PROPERTIES of VAPOR-DEPOSITED SINGLE-CRYSTAL-LINE GaN. *Applied Physics Letters* **1969**, *15* (10), 327–329.

6. Manasevit, H. M.; Erdmann, F. M.; Simpson, W. I. The Use of Metalorganics in the Preparation of Semiconductor Materials. *Journal of The Electrochemical Society* **1971**, *118* (11), 1864.

7. Amano, H.; Sawaki, N.; Akasaki, I.; Toyoda, Y. Metalorganic Vapor Phase Epitaxial Growth of a High Quality GaN Film Using an AlN Buffer Layer. *Applied Physics Letters* **1986**, *48* (5), 353–355.

8. Nakamura, S. GaN Growth Using GaN Buffer Layer. *Japanese Journal of Applied Physics* **1991**, *30* (Part 2, No. 10A), L1705–L1707.

9. Waide, P.; Satoshi, T. Light's Labour's Lost: Policies for Energy-Efficient Lighting; OECD Publications Centre, 2006.

10. Shur, M. S.; Zukauskas, R. Solid-State Lighting: Toward Superior Illumination. *Proceedings of the IEEE* **2005**, *93* (10), 1691–1703.

11. Pankove, J. I.; Miller, E. A.; Berkeyheiser, J. E. GaN Electroluminescent Diodes. 1971 International Electron Devices Meeting 1971.

12. Amano, H.; Akasaki, I.; Kozawa, T.; Hiramatsu, K.; Sawaki, N.; Ikeda, K.; Ishii, Y. Electron Beam Effects on Blue Luminescence of Zinc-Doped GaN. *Journal of Luminescence* **1988**, 40-41, 121–122.

13. Amano, H.; Kito, M.; Hiramatsu, K.; Akasaki, I. P-Type Conduction in Mg-Doped GaN Treated with Low-Energy Electron Beam Irradiation (LEEBI). *Japanese Journal of Applied Physics* **1989**, *28* (Part 2, No. 12), L2112–L2114.

14. Nakamura, S.; Mukai, T.; Senoh, M.; Iwasa, N. Thermal Annealing Effects on P-Type Mg-Doped GaN Films. *Japanese Journal of Applied Physics* **1992**, *31* (Part 2, No. 2B), L139–L142.

15. Nakamura, S.; Senoh, M.; Mukai, T. P-GaN/N-InGaN/N-GaN Double-Heterostructure Blue-Light-Emitting Diodes. *Japanese Journal of Applied Physics* **1993**, *32* (Part 2, No.1A/B), L8–L11.

16. Nakamura, S.; Senoh, M.; Iwasa, N.; Nagahama, S. High-Brightness InGaN Blue, Green and Yellow Light-Emitting Diodes with Quantum Well Structures. *Japanese Journal of Applied Physics* **1995**, *34* (Part 2, No. 7A), L797–L799.

17. McCluskey, M. D.; Romano, L. T.; Krusor, B. S.; Bour, D. P.; Johnson, N. M.; Brennan, S. Phase Separation in InGaN/GaN Multiple Quantum Wells. *Applied Physics Letters* **1998**, *72* (14), 1730–1732.

18. Ru-Chin Tu; Chun-Ju Tun; Shyi-Ming Pan; Chang-Cheng Chuo; Sheu, J. K.; Ching-En Tsai; Te-Chung Wang; Gou-Chung Chi. Improvement of Near-Ultraviolet InGaN-GaN Light-Emitting Diodes with an AlGaN Electron-Blocking Layer Grown at Low Temperature. *IEEE Photonics Technology Letters* **2003**, *15* (10), 1342–1344.

19. Chang, S. J.; Lin, Y. C.; Su, Y. K.; Chang, C. S.; Wen, T. C.; Shei, S. C.; Ke, J. C.; Kuo, C. W.; Chen, S. C.; Liu, C. H. Nitride-Based LEDs Fabricated on Patterned Sapphire Substrates. *Solid-State Electronics* **2003**, *47* (9), 1539–1542.

20. Ryu, H. Y.; Jeon, K. S.; Kang, M. G.; Yuh, H. K.; Choi, Y. H.; Lee, J. S. A Comparative Study of Efficiency Droop and Internal Electric Field for InGaN Blue Lighting-Emitting Diodes on Silicon and Sapphire Substrates. *Scientific Reports* **2017**, *7* (1).

21. Shioda, T.; Yoshida, H.; Tachibana, K.; Sugiyama, N.; Nunoue, S. Enhanced Light Output Power of Green LEDs Employing AlGaN Interlayer in InGaN/GaN MQW Structure on Sapphire (0001) Substrate. *physica status solidi (a)* **2012**, *209* (3), 473–476.

22. Hashimoto, R.; Hwang, J.; Saito, S.; Nunoue, S. High-Efficiency Yellow Light-Emitting Diodes Grown on Sapphire (0001) Substrates. *physica status solidi (c)* **2014**, *11* (3-4), 628–631.

23. Hwang, J.-I.; Hashimoto, R.; Saito, S.; Nunoue, S. Development of InGaN-Based Red LED Grown on (0001) Polar Surface. *Applied Physics Express* **2014**, *7* (7), 071003.

24. Jin, S. X.; Li, J.; Li, J. Z.; Lin, J. Y.; Jiang, H. X. GaN Microdisk Light Emitting Diodes. *Applied Physics Letters* **2000**, *76* (5), 631–633.

25. Tian, P.; McKendry, J. J. D.; Gong, Z.; Guilhabert, B.; Watson, I. M.; Gu, E.; Chen, Z.; Zhang, G.; Dawson, M. D. Size-Dependent Efficiency and Efficiency Droop of Blue InGaN Micro-Light Emitting Diodes. *Applied Physics Letters* **2012**, *101* (23), 231110.

26. Chen, W.; Hu, G.; Lin, J.; Jiang, J.; Liu, M.; Yang, Y.; Hu, G.; Lin, Y.; Wu, Z.; Liu, Y.; Zhang, B. High-Performance, Single-Pyramid Micro Light-Emitting Diode with Leakage Current Confinement Layer. *Applied Physics Express* **2015**, *8* (3), 032102.

27. Wong, M. S.; Hwang, D.; Alhassan, A. I.; Lee, C.; Ley, R.; Nakamura, S.; DenBaars, S. P. High Efficiency of III-Nitride Micro-Light-Emitting Diodes by Sidewall Passivation Using Atomic Layer Deposition. *Optics Express* **2018**, *26* (16), 21324.

28. Bai, J.; Cai, Y.; Feng, P.; Fletcher, P.; Zhao, X.; Zhu, C.; Wang, T. A Direct Epitaxial Approach to Achieving Ultrasmall and Ultrabright InGaN Micro Light-Emitting Diodes (μLEDs). *ACS Photonics* **2020**, *7* (2), 411-415.

29. Bai, J.; Cai, Y.; Feng, P.; Fletcher, P.; Zhu, C.; Tian, Y.; Wang, T. Ultrasmall, Ultracompact and Ultrahigh Efficient InGaN Micro Light Emitting Diodes (μLEDs) with Narrow Spectral Line Width. *ACS Nano* **2020**, *14* (6), 6906-6911.

30. Feng, P.; Xu, C.; Bai, J.; Zhu, C.; Farrer, I.; Martinez de Arriba, G.; Wang, T. A Simple Approach to Achieving Ultrasmall III-Nitride Microlight-Emitting Diodes with Red Emission. *ACS Applied Electronic Materials* **2022**, *4* (6), 2787–2792.

31. Konoplev, S. S.; Bulashevich, K. A.; Karpov, S. Yu. From Large-Size to Micro-LEDs: Scaling Trends Revealed by Modeling. *physica status solidi (a)* **2017**, *215* (10), 1700508.

32. Hwang, D.; Mughal, A. J.; Wong, M. S.; Alhassan, A. I.; Nakamura, S.; DenBaars, S. P. Micro-Light-Emitting Diodes with III–Nitride Tunnel Junction Contacts Grown by Metalorganic Chemical Vapor Deposition. *Applied Physics Express* **2017**, *11* (1), 012102.

33. Olivier, F.; Daami, A.; Dupré, L.; Henry, F.; Aventurier, B.; Templier, F. 25-4: Investigation and Improvement of 10μm Pixel-Pitch GaN-Based Micro-LED Arrays with Very High Brightness. *SID Symposium Digest of Technical Papers* **2017**, *48* (1), 353–356.

34. Jiang, H. X.; Jin, S. X.; Li, J.; Shakya, J.; Lin, J. Y. III-Nitride Blue Microdisplays. *Applied Physics Letters* **2001**, *78* (9), 1303–1305.

35. Choi, H. W.; Jeon, C. W.; Dawson, M. D. InGaN Light Emitting Diodes of Micro-Ring Geometry. *physica status solidi (c)* **2003**, No. 7, 2185–2188.

36. Choi, H. W.; Liu, C.; Gu, E.; McConnell, G.; Girkin, J. M.; Watson, I. M.; Dawson, M. D. GaN Micro-Light-Emitting Diode Arrays with Monolithically Integrated Sapphire Microlenses. *Applied Physics Letters* **2004**, *84* (13), 2253–2255.

37. Tan; Zhou; Hu; Wang; Yao. Light Extraction Enhancement of InGaN Based Micro Light-Emitting Diodes with Concave-Convex Circular Composite Structure Sidewall. *Applied Sciences* **2019**, *9* (17), 3458.

38. Hong, I. Y.; Lee, J. H.; Cho, S. M.; So, J. B.; Kim, T. K.; Cha, Y.-J.; Kwak, J. S. Impact of Hydrothermally Grown ZnO Nanorods on External Quantum Efficiency of 32 × 32 Pixelated InGaN/GaN Micro-LED Array. *IEEE Transactions on Nanotechnology* **2019**, *18*, 160–166.

Chapter 2

Background

2.1 Semiconductors

The energy separation between the valence band and conduction band of electrons is defined by the bandgap, which represents the minimum energy required to excite an electron from the valence band to the conduction band.[1] In theory, materials with different bandgaps have different carrier concentrations, leading to different electrical conductivities.

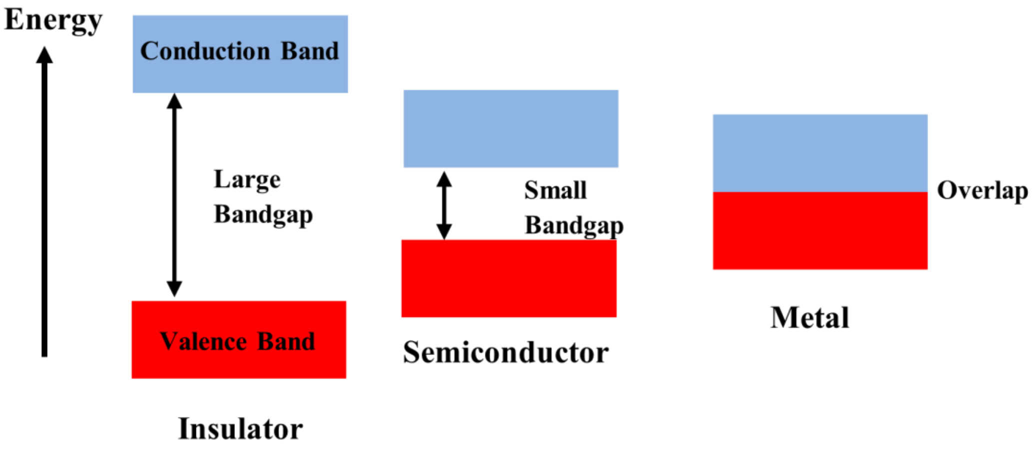

Figure 2.1. *Illustration of bandgaps for insulators, semiconductors and metals.*

Solid materials are classified as insulators, semiconductors or metals according to the difference in electrical conductivity. Generally speaking, the bandgap of an insulator is too large to generate adequate free electrons in the conduction band. Thus, the electrical conductivity of an insulator is very low, around 10^{-18}–10^{-8} S/cm.[2] For metals, the bandgap energy is very small, the conduction band and valanced band of some metals are even overlapped. Hence, metals usually have partially filled bands, leading to high conductivity of 10^{4}–10^{6} S/cm[2]. Some semimetals like Tin also have overlapping bands.

The bandgap energies and conductivities of semiconductors fall between those of metals and insulators. The band structures of insulators, semiconductors, and metals are illustrated in Figure 2.1.

2.1.1 Direct and Indirect Bandgap Structures

Depending on the difference in band structure, semiconductors are classified into two types: direct bandgap semiconductors and indirect bandgap semiconductors.[3] As shown in Figure 2.2, the top of the valence band and the bottom of the conduction band of direct bandgap semiconductors are located at identical momentum. Thus, electron-hole recombination occurs directly and without any momentum loss, resulting in short carrier lifetime and high optical efficiency. This is also one of the most important advantages of fabricating emitters by direct bandgap semiconductors. Unlike direct bandgap materials, the maximum of the valence band and minimum of the conduction band of indirect bandgap materials have different momenta. During the process of electron-hole recombination, the electron needs to change its crystal momentum by emitting or absorbing phonons, thereby enhancing the carrier lifetime and generating thermal virbation.[3] Therefore, the optical performance of indirect bandgap semiconductors is limited.

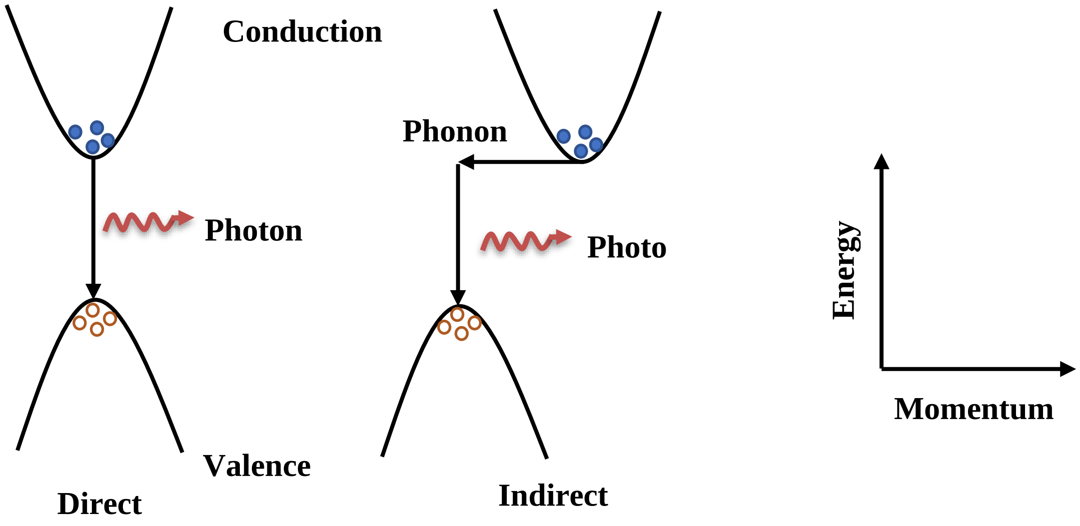

Figure 2.2. *Illustration of direct and indirect bandgap structures.*

2.1.2 Recombination

As illustrated in Figure 2.3, electron-hole recombination has three types: radiative recombination, Shockley–Read–Hall (SRH) recombination, and Auger recombination.[4] Radiative recombination occurs when an electron in the conduction band recombines with a hole in the valence band and generates a photon. For example, spontaneous emission and stimulated emission are both optical processes related to radiative recombination. SRH recombination and Auger recombination are both non-radiative recombination. SRH recombination occurs when an electron is trapped by a defect energy level and generates lattice vibration (thermal energy) rather than a photon in the recombination process.[5–6] In Auger recombination, the recombination of electron-hole pairs does not generate photons but instead excites another free carrier to a higher energy level.[7] The total recombination lifetime in a semiconductor material is given by:

$$\frac{1}{\tau} = \frac{1}{\tau_{rad}} + \frac{1}{\tau_{non}} \tag{2.1}$$

where τ_{rad} is the radiative recombination lifetime and τ_{non} is the non-radiative recombination lifetime.[8–10]

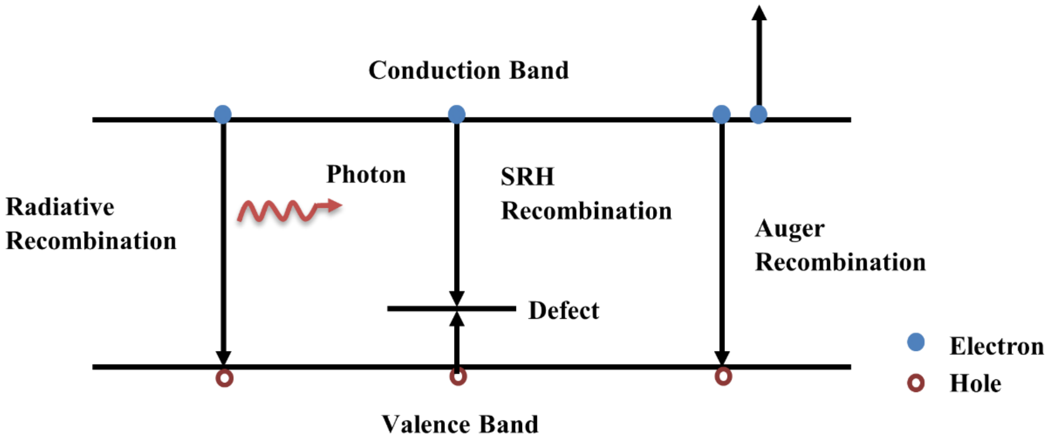

Figure 2.3. *Illustration of radiative recombination, SRH recombination, and Auger recombination.*

The ratio of radiative recombination to total recombination represents the IQE, as shown in the equation below:[10]

$$\eta_{IQE} = \frac{\tau_{rad}^{-1}}{\tau_{rad}^{-1} + \tau_{non}^{-1}} \tag{2.2}$$

2.1.3 Crystal Structures

Diamond, zinc blende, and wurtzite are three common crystal structures of semiconductor materials.[11] Silicon and germanium are both group IV elements and typical diamond structure semiconductors, as demonstrated in Figure 2.4a. The unit cell of the diamond structure semiconductor is a regular tetrahedron. If the centre of the tetrahedron unit is occupied by a different atom, the zinc blende structure semiconductor is formed (Figure 2.4b).[11] For example, GaAs and InP are both typical zinc blende structures. Figure 2.4c illustrates the wurtzite crystal structure, which has a hexagonal close packing (hcp).[12] To indicate different planes and orientations in the crystal, Miller indices (*h k i l*) are induced.[13] For the cubic structure, the three factors *h*, *k* and *l* are enough to indicate the orientations. However, in the wurtzite structure, factor *i* is also necessary due to the hexagonal structure.

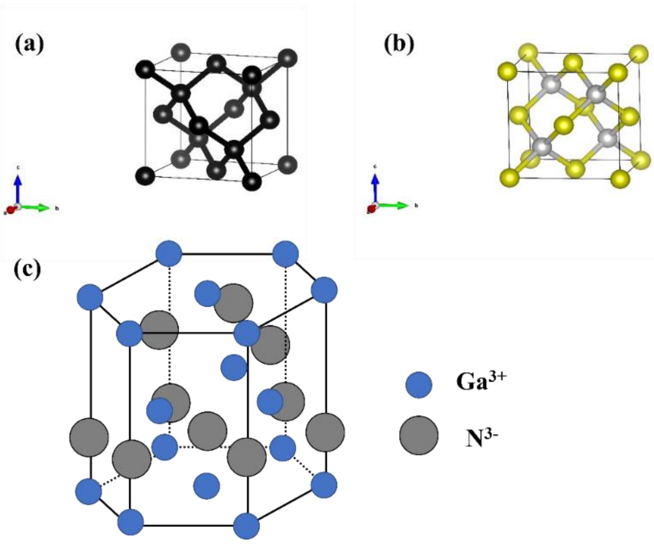

Figure 2.4. *The diamond structure (a), zinc blende structure (b) and wurtzite structure (c).*

2.1.4 Crystal Defect

Crystal defect is one of the essential problems of III-nitride-based semiconductors. For example, large lattice-mismatched substrates such as sapphire and silicon are generally used for the epitaxy of GaN, leading to high crystal defect density. Theoretically, crystal defects are classified into zero-dimensional (0D) defects, one-dimensional (1D) defects, two-dimensional (2D) defects and three-dimensional (3D) defects. 0D defects, also known as 'point defects', occur when an atom is lost (vacancy), located in the space of atoms (interstitial) or substituted by foreign atoms (substitutional impurity), as shown in Figure 2.5.[14]

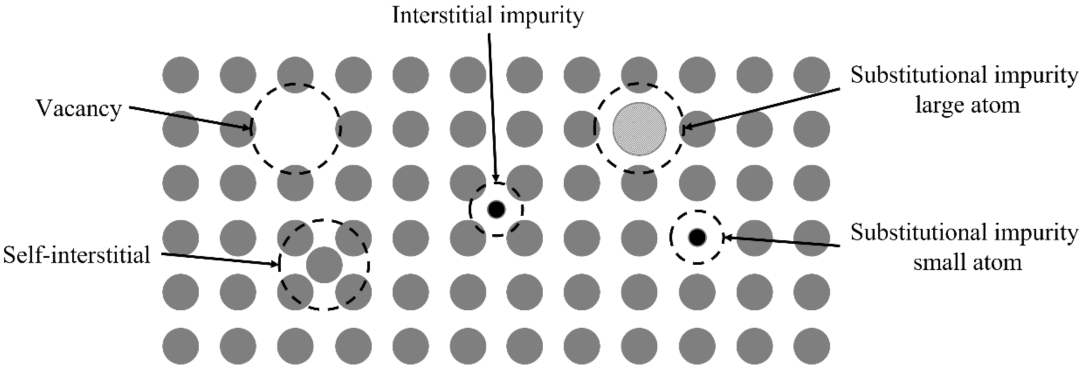

Figure 2.5. *Illustration of 5 types of point defects.*

1D defects are also called 'line defects', and they include edge dislocation and screw dislocation.[15,16] In general, these two types of dislocations always occur together, an event referred to as 'mixed dislocation'. Figure 2.6 illustrates these two dislocations. Dislocations are normally formed by the malposition of atoms along a line. The type of dislocation is defined by Burgers vector *b* and the dislocation line, which are both shown in Figure 2.6. Burgers vector represents the direction and magnitude of a dislocation. It is clear that the Burgers vector of an edge dislocation is vertical to the dislocation line, whereas it is parallel to the dislocation line in screw dislocation.

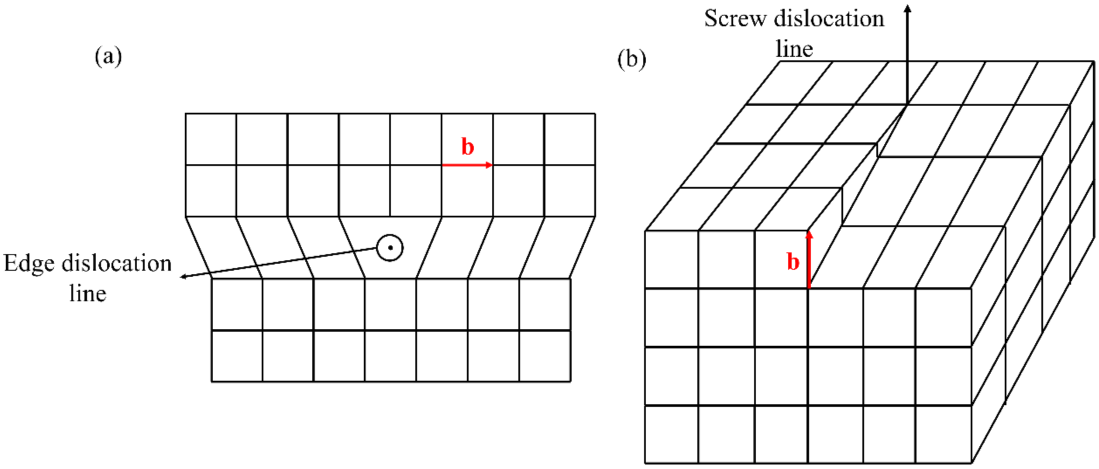

Figure 2.6. *Illustration of edge dislocation (a) and screw dislocation (b).*

2D defects are planar defects such as a stacking fault (SF), which is caused by errors in the sequence of atomic planes.[17] Figure 2.7 illustrates a typical stacking fault in the face-centred cubic structure. For III-nitride-based semiconductors, the normal stacking sequence is ABABAB. When *c*-plane GaN is grown on (0001) sapphire, a new plane C would be inserted and thereby change the stacking sequence to ABC, leading to SFs. However, these types of SF lie on the basal planes and are limited to the interface between sapphire and GaN, so-called 'basal-plane stacking faults' (BSFs). Volume defects such as pits, voids, hillocks and cracks are all typical 3D defects.

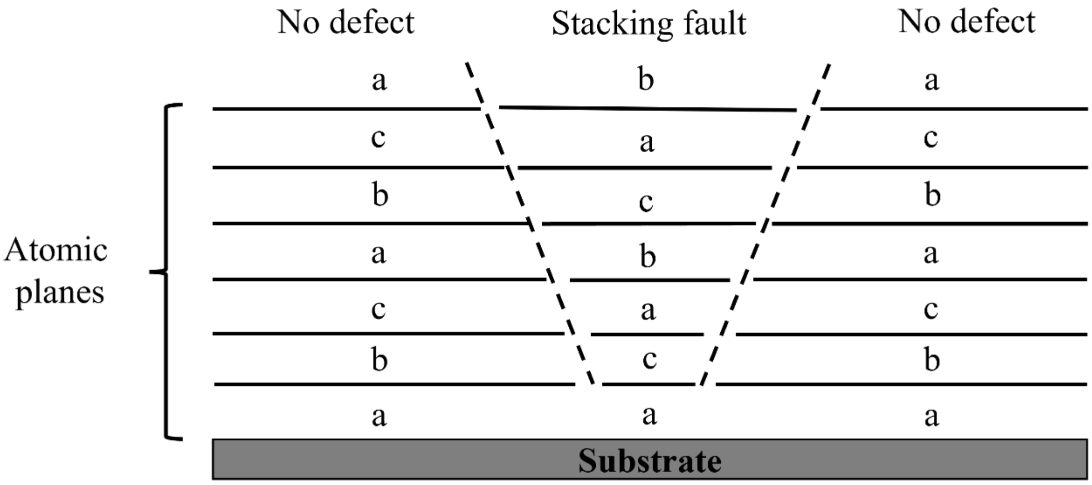

Figure 2.7. *Illustration of 2D defects (stacking fault).*

2.1.5 Doping

The number of free electrons and holes is limited in intrinsic semiconductors. To generate additional free electrons or holes, and to modify the conductivity of semiconductors, a technique of adding impurities (i.e. ‘doping’) is normally used. The doped semiconductor is referred to as an ‘extrinsic semiconductor’, and the impurities are called ‘dopants’. For instance, a small quantity of silicon atoms are commonly doped into gallium nitride to replace gallium atoms and provide extra free electrons to synthesise.[18] Similarly, doping a small quantity of magnesium atoms into gallium nitride can form p-type GaN.[19] Magnesium atoms are used to substitute gallium atoms and provide extra free holes. A typical doping level of Mg-doped GaN is around 10^{18} to 10^{19} /cm^3. The carrier concentration of an extrinsic semiconductor under thermal equilibrium can be given by:

$$n_0 \times p_0 = n_i^2 \tag{2.3}$$

where n_0 is the concentration of free electrons, p_0 is the concentration of free holes, and n_i is the intrinsic carrier concentration.

2.1.6 Structure of a Semiconductor Light-Emitting Diode

An LED is a kind of p–n junction that can emit light when a current flows through it, as shown in Figure 2.8.[20] At equilibrium, a depletion region forms due to the diffusion of electrons and holes. When a forward bias is applied, the electrons will move from the n-side to the p-side, and holes will move from the p-side to the n-side, leading to a reduction of the depletion region. Then, the electrons and holes recombine and generate photons in the active region. Under reverse bias, the movement of electrons and holes is opposite to that under forward bias, and the depletion region is increased. Thus, the p–n junction LED is unidirectional conducting.

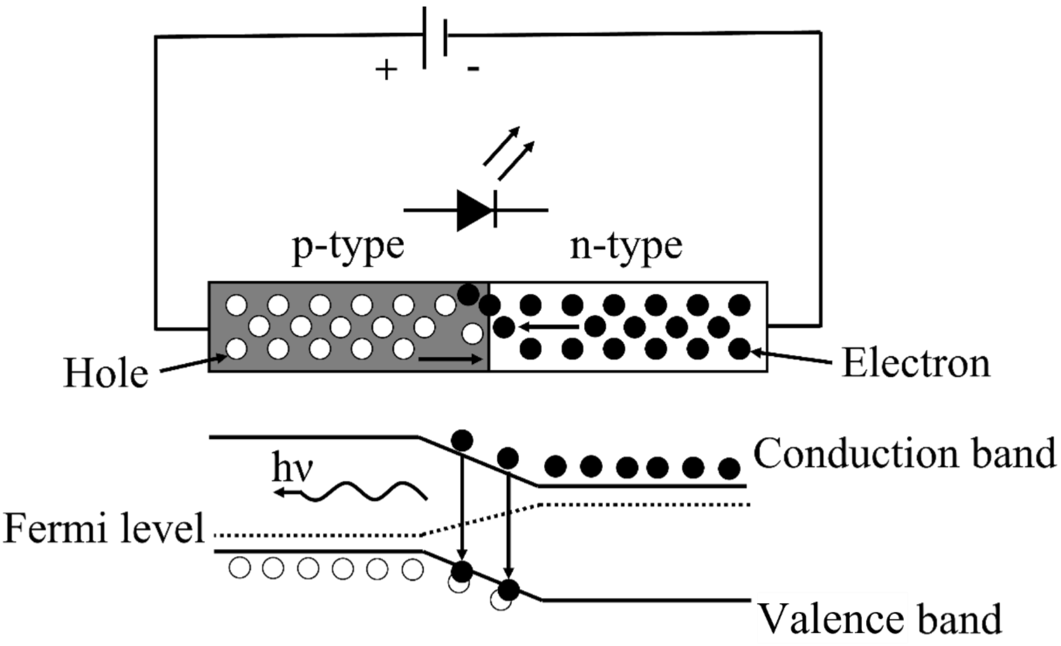

Figure 2.8. *Schematic of a p–n junction LED under forward bias.*

2.2 III-Nitride Semiconductors

2.2.1 Material Properties

GaN, AlN, InN and their ternary alloys are all included in III-nitride compound semiconductors. Figure 2.9 illustrates the bandgap energies of various semiconductor materials, including III-nitride-based semiconductors.[21] It is very clear that the bandgap energy of III-nitride-based semiconductors covers a broad range of emission wavelengths from deep UV (200 nm) to infrared (1590 nm). Additionally, III-nitride semiconductors are all direct bandgap materials. Therefore, III-nitride semiconductors are ideal for fabricating optoelectronics such as LEDs, laser diodes, and photodetectors. The lattice constants of III-nitride ternary alloys are almost linear with the alloy composition. The lattice constant is described by:

$$a_{MGaN} = xa_{MN} + (1-x)a_{GaN} \tag{2.4}$$

where x is the chemical composition of In or Al, a_{MN} is the lattice constant of InN or AlN, and a_{GaN} is the lattice constant of GaN.

The bandgap energy of III-nitride ternary alloys can be calculated by:

$$E_{g,MGaN} = xE_{g,MN} + (1-x)E_{g,GaN} - bx(1-x) \tag{2.5}$$

where $E_{g,MN}$ is the bandgap energy of InN or GaN, $E_{g,GaN}$ is the bandgap energy of GaN and b is the bowing parameter. The bandgap energy values of GaN, InN, and AlN are listed in Table 2.1.[22]

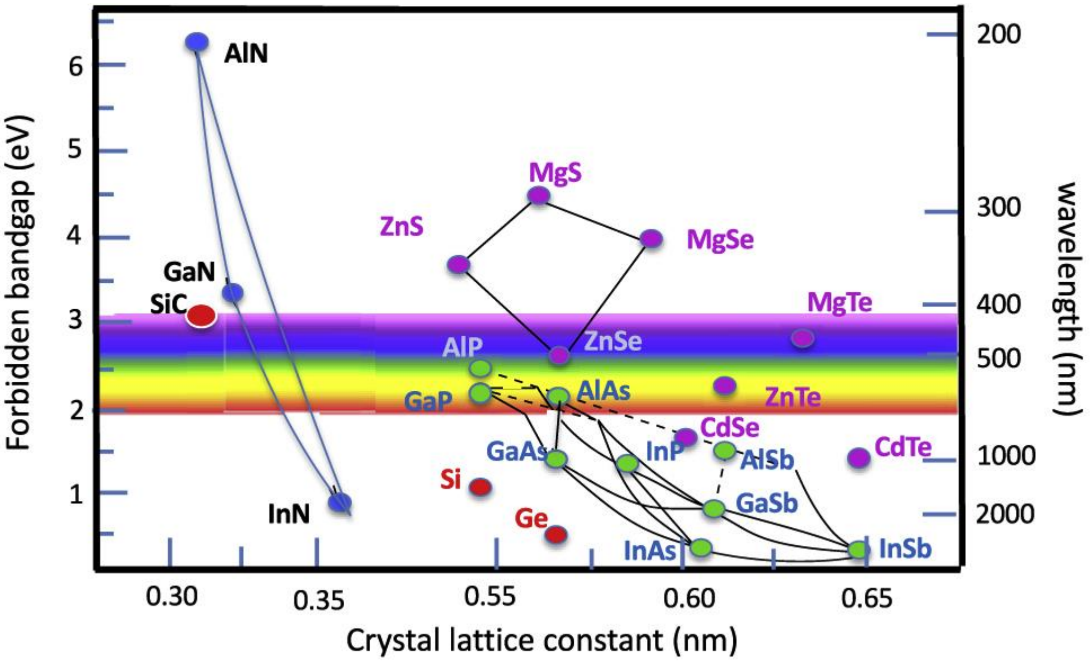

__Figure 2.9.__ Bandgaps and emission wavelengths of various semiconductors at room temperature.[21]

__Table 2.1.__ Crystal parameters of III-nitride semiconductors with wurtzite structure.[22]

III-nitrides	Lattice constant a (Å)	Lattice constant c (Å)	Bond length (Å)	Bandgap (eV)
GaN	3.1893	5.1851	1.94	3.42
AlN	3.112	4.982	1.89	6.2
InN	3.5446	5.4034	2.15	0.78

III-nitride semiconductors generally have one of three crystal structures: wurtzite, zinc blende, or rock-salt. However, the rock-salt phase GaN can be formed only under high pressure, and the zinc blende GaN is metastable under normal conditions.[23,24] Thus, GaN with wurtzite structure, being the most stable formation, is widely used in III-nitride semiconductors.[25,26] It should be mentioned that the III-nitride semiconductor materials involved in this project are all wurtzite structures. The lattice constants and other important material parameters of GaN, InN and AlN are listed in Table 2.1.[22]

Table 2.2 lists the electrical and thermal parameters of some common semiconductors, including GaN.[22,27–34] Electron mobility is an essential parameter by which to evaluate materials; it represents the moving speed of free electrons under the action of an electrical field. Moreover, electron mobility can be affected by defects, impurities and lattice vibrations (phonons). For this reason, the measured values of GaN electron mobility reported in many papers are different. The highest electron mobility of GaN is 1245 $cm^2 \cdot V^{-1}s^{-1}$ and was measured on a freestanding GaN grown by HVPE.[27] For high-crystal-quality GaN grown by MOCVD, the highest electron mobility value is around 1000 $cm^2 \cdot V^{-1}s^{-1}$.[35]

Table 2.2. *Electrical and thermal properties of semiconductor materials at room temperature.*[22,27–34]

III-nitrides	Electron mobility ($cm^2V^{-1}s^{-1}$)	Breakdown field ($MV \cdot cm^{-1}$)	Thermal conductivity ($W \cdot cm^{-1} \cdot K^{-1}$)	Melting point (℃)
GaN	1245	3.3	2.3	2500
GaAs	9400	0.4	0.55	1238
Si	1400	0.3	1.56	1414
InP	4000	0.5	0.68	1062

In Table 2.2, compared with other semiconductor materials sucha as GaAs, Si, and InP, GaN material has the highest breakdown voltage of 3.3 MV·cm-1, highest thermal conductivity of 2.3 W·cm-1·K-1and highest melting point of 2500 ℃. In addition, Ga-polar GaN has ideal chemical stability. It is very resistant to etching with acid or alkaline solutions.36 A potassium hydroxide (KOH) solution can etch Ga-polar GaN only through defects such as pits. However, the N-polar GaN is very easily etched with

KOH solution.36 Thus, KOH etching is an effective method to determine the polarity of III-nitride semiconductors.

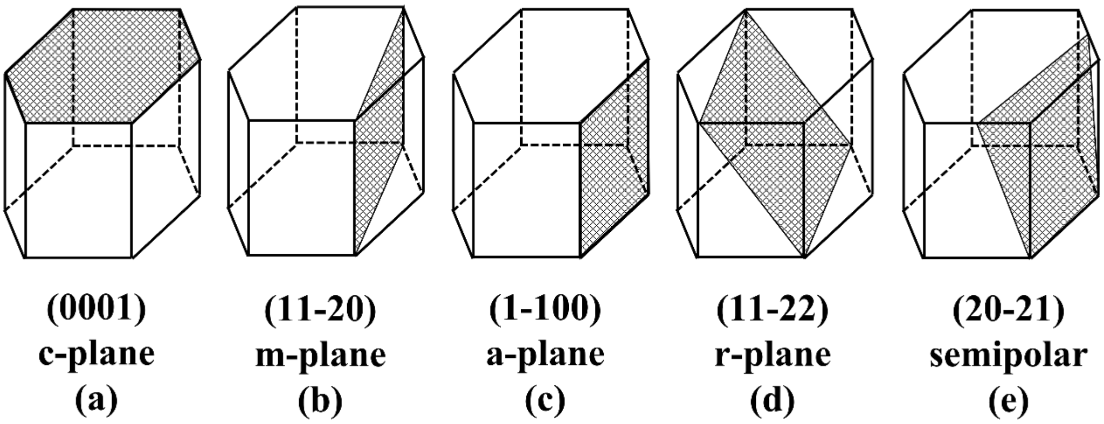

Figure 2.10. *Five common planes of wurtzite GaN.*

Polar GaN (*c*-plane), which has a strong polarisation along (0001), is the most widely used orientation of III-nitride semiconductor. Nonpolar and semipolar are the other two types of GaN polarisation, these have eliminated or reduced quantum-confined Stark effect (QCSE) compared with polar GaN. This phenomenon is attributed to the inclined angle to the (0001) plane in these orientations. Figure 2.10 illustrates some common planes of nonpolar and semipolar GaN. Both the *a*-plane and *m*-plane GaN are nonpolar planes that are vertical with the *c*-plane. The (11-22) plane with an inclined angle to a *c*-plane of 58.41^o and (20-21) plane with an inclined angle to a *c*-plane of 75.09^o are both widely used for semipolar III-nitride-based optoelectronics.[8]

2.2.2 Challenges in III-Nitride-Based Semiconductors

Quantum-confined Stark Effect

The quantum-confined Stark effect is defined as the shift of quantum-confined energy levels in a quantum well under an electric field.[3] In III-nitride heterostructure, because of the strong spontaneous and piezoelectric polarization, a built-in electric field is produced.[37–39] Generally, the dipole moments are cancelled out in semiconductors with symmetric crystal structure, such as diamond structure, rendering the system's dipole moment macroscopically zero. However, because of the asymmetry, the dipole moments are not fully cancelled in wurtzite GaN, leading to spontaneous polarisation along [000-1] direction. The spontaneous polarisation of unstrained GaN, AlN and InN are -0.029, -0.032 and -0.081 C/m^2, respectively.[40] The spontaneous polarisation of III-nitride ternary alloys without strain is given by:

$$P_{sp,MGaN} = xP_{sp,MN} + (1-x)P_{sp,GaN} \tag{2.6}$$

where $P_{sp,MN}$ represents the spontaneous polarisation of AlN or InN, $P_{sp,GaN}$ is the spontaneous polarisation of GaN, and x is the composition of Al or In.

Normally, the III-nitride heterostructure has large strain between layers. In this situation, piezoelectric polarisation is generated due to the displacement of atoms. The strain can be calculated by:

$$\varepsilon_{xx} = \varepsilon_{yy} = \frac{(a-a_0)}{a_0} \tag{2.7}$$

$$\varepsilon_{zz} = \frac{(c-c_0)}{c_0} \tag{2.8}$$

where ε_{xx} and ε_{yy} are both isotropic in-plane strains, ε_{zz} represents the out-of-plane strain, a and c are lattice constants under strain, and a_0 and c_0 are lattice constants under equilibrium. The piezoelectric polarisation is then given by:

$$P_{pz} = e_{31}\left(\varepsilon_{xx} + \varepsilon_{yy}\right) + e_{33}\varepsilon_{zz} \tag{2.9}$$

where e_{31} and e_{33} denote the piezoelectric constants.[40] The total polarisation can be expressed by the equation:

$$P = P_{sp} + P_{pz} \tag{2.10}$$

In a GaN/InGaN/GaN quantum well (QW), InGaN is under compressive strain, leading to a piezoelectric polarisation pointing along [0001]. Meanwhile, InGaN has a similar spontaneous polarisation coefficient and a larger lattice mismatch with GaN. As a result, the piezoelectric polarisation is stronger than spontaneous polarisation, resulting in a total polarisation along [0001] direction in the QW.

As shown in Figure 2.11, the band alignment of GaN/InGaN/GaN QW is distorted under the polarisation-induced built-in electric field. The electron and hole distributions are changed, and the overlap between the electron wave function and the hole wave function is dramatically reduced.[40] This phenomenon results in the decrease of radiative recombination, thereby limiting the IQE. Furthermore, to achieve long-wavelength green, yellow and even red LEDs, a high indium content of >20% in the InGaN quantum well is necessary. In this case, the QCSE is significantly increased, resulting in a further reduction of overlap between electron wave function and hole wave function, further decreasing the efficiency of LEDs. Compared with the case without polarisation, QCSE can generate a red shift because of the reduction in bandgap energy. Under large injection currents, the QCSE can be reduced and a blue shift can be generated, which causes emission wavelength instability in III-nitride-based LEDs.

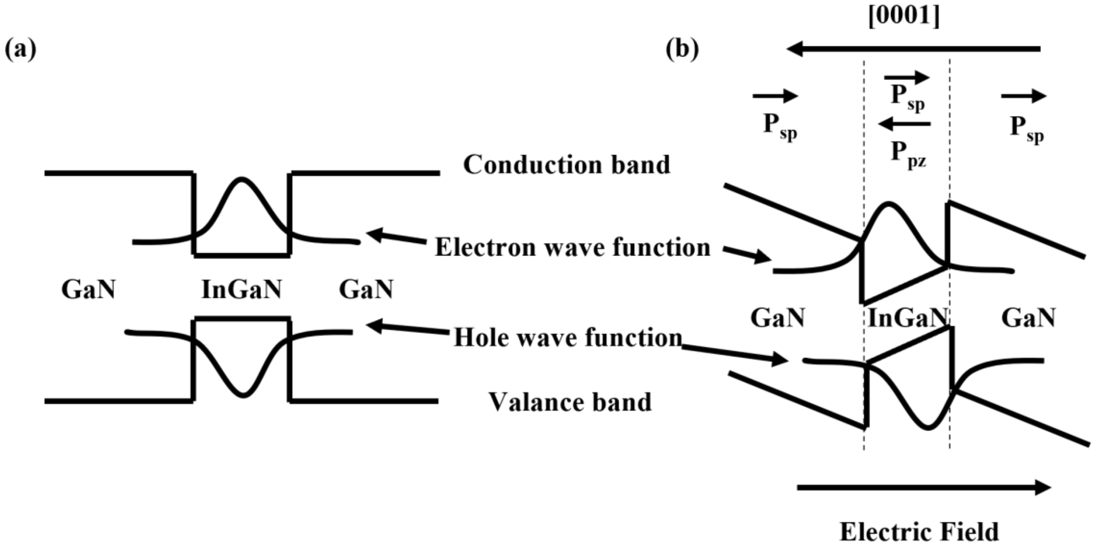

Figure 2.11. *Band alignment of the QW without a built-in electric field (a), and band structure of the QW with a built-in electric field (b).*

Green Gap

Today, blue III-nitride-based LEDs have achieved high brightness and efficiency (>70%). However, the quantum efficiency dramatically decreases with the increase of emission wavelength. This phenomenon is commonly known as the ‘green–yellow gap’.[41] In theory, higher indium composition of QWs is required to achieve long-wavelength emission. This can be achieved by reducing the growth temperature of QW during MOCVD growth. However, with the increase of indium composition, the QCSE is also enhanced, limiting the IQE of long-wavelength LEDs. Meanwhile, the crystal quality of QW is limited as well due to the increased defect density induced by the low growth temperature.[42] As a result, the radiative recombination efficiency is reduced, and the non-radiative recombination is enhanced. Thus, long-wavelength III-nitride-based LEDs generally show a limited light intensity and a low quantum efficiency, resulting in the green gap, as shown in Figure 2.12.

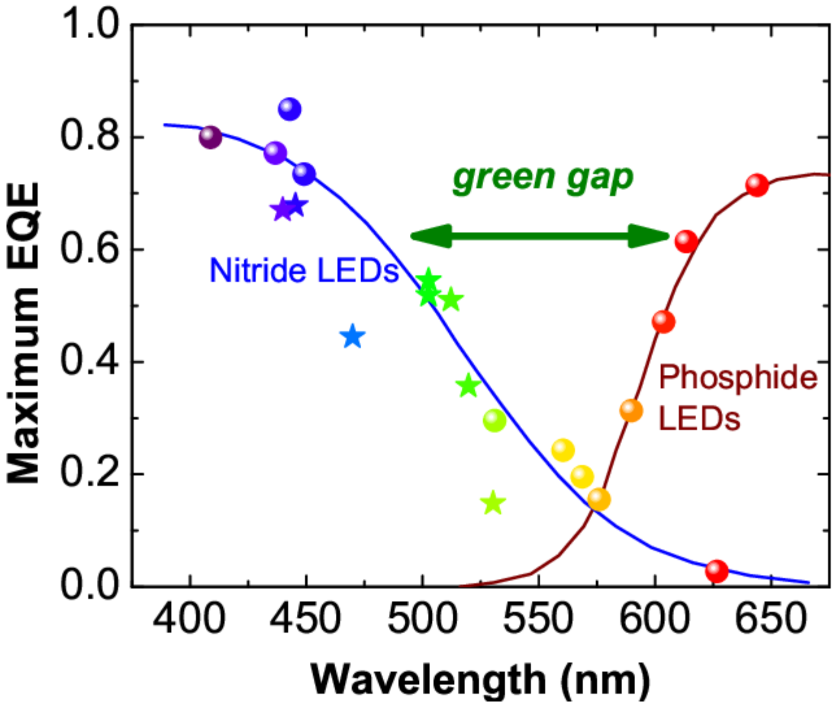

Figure 2.12. *Illustration of the green gap of III-nitride-based LEDs.*[41]

Efficiency Droop

In general, III-nitride-based LEDs exhibit peak EQE value at a low injection current, normally less than 10 A/cm^2. With the further increase of the injection current density, the EQE would be reduced gradually; this is known as 'efficiency droop'. Figure 2.13 indicates the efficiency droop of a typical blue LED at various temperatures.[43] Many researchers posit three potential reasons for efficiency droop. First, due to the presence of crystal defects in the GaN material, the SRH recombination cannot be avoided, and it is enhanced with the increase of the injection current density.[44] Second, the EQE of LEDs would also be reduced by the effect of Auger recombination.[44,45] The third important reason for efficiency droop may be electron leakage.[46–48] When the injection electrons overflow the active region, the extra electrons will leak from the active region, and it will not generate radiative recombination. Therefore, the quantum efficiency decreases with the increase of injection current.

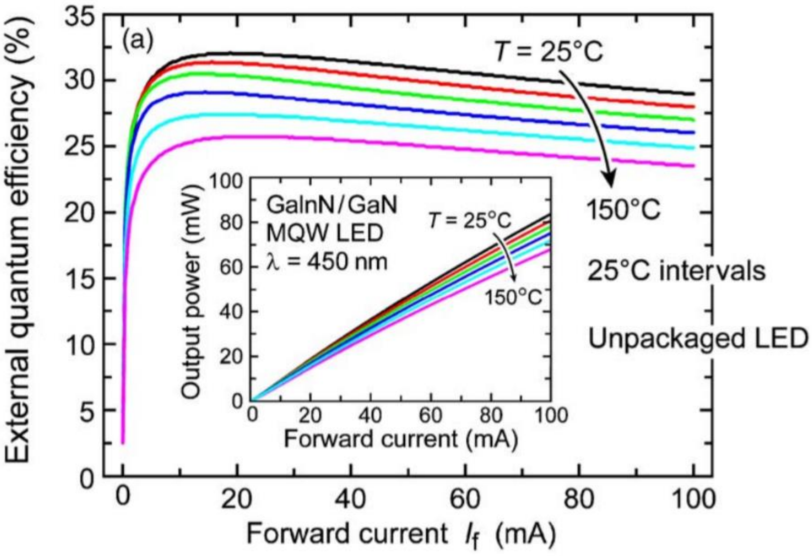

Figure 2.13. *Efficiency droop of the InGaN/GaN MQWs blue LED at different temperatures.*[43]

D. Hwang reported that efficiency droop is reduced with the decrease of μLED dimension.[49] In a sample of μLEDs with 100 μm dimensions, the current-spreading is not uniform due to the large device area. This situation is exacerbated when the LED is applied at a high current density, resulting in uneven light emission. Thus, efficiency droop is more serious at high current densities. For μLEDs with dimension <50 μm, current-spreading is more uniform, and efficiency droop is improved. Therefore, it has been shown that reducing the dimension of LEDs to make μLEDs is an effective method of decreasing efficiency droop.

Epitaxial Substrates

The most common epitaxial substrates for GaN epitaxial growth are sapphire, silicon (Si), silicon carbide (SiC) and single-crystal GaN. Of course, single-crystal GaN is an ideal epitaxial substrate. However, the fabrication technology of single-crystal GaN is still in its infancy. Therefore, the price of a GaN substrate is very high, around £2000 per 2-inch wafer. SiC has a lattice mismatch with GaN of only 3.5%, which is the smallest of any heteroepitaxy substrate.[50] Meanwhile, the thermal conductivity of 4.9 W/cm is also very close to that of GaN.[50] Unfortunately, SiC is also an expensive material because of production technology limitations. Hence, only a few researchers are using it.

Table 2.3. *Relative material constants of GaN and the epitaxial substrates 6H-SiC, sapphire and Si.*[50–55]

Material	**GaN**	**6H-SiC**	**Sapphire**	**Si**
Lattice constant (Å)	a=3.189 c=5.185	a=3.081 c=15.117	a=4.759 c=12.991	a=5.431
Lattice mismatch to GaN	–	-3.1%	-16%	17%
Thermal expansion mismatch to GaN (a)	–	-25.3%	23.4%	-115%
Thermal conductivity (Wcm-1K-1)	4.1	4.9	0.41	1.3
Melting point (K)	2791	3102	2303	1690

As a material with high hardness, good thermal stability and excellent chemical stability, sapphire is widely used for GaN epitaxy. Although the lattice mismatch of 16% between sapphire and GaN is very high and the thermal conductivity of 0.41 W/cmK is very low, sapphire has nevertheless become the most widely used substrate because of its low cost. Compared with other substrates, Si has the largest lattice mismatch (17%) and largest thermal expansion mismatch (115%) to GaN.[50] Thus, the crystal quality and surface smoothness of GaN on Si epitaxy wafer are limited. As the cheapest substrate, Si is also very easy to remove for lift-off operation. Therefore, it is expected to become an ideal solution for the growth of III-nitride optoelectronics.

2.2.3 Epitaxial Gallium Nitride on Sapphire by Metal–Organic Chemical Vapour Deposition

High-crystal-quality GaN can be grown on a 2-inch c-plane sapphire substrate by a conventional two-step GaN growth method using a metal–organic chemical vapor deposition (MOCVD) technique. Two-step GaN growth consists of the growth of a low- temperature (LT) GaN nucleation layer and the growth of a high-temperature (HT) GaN buffer layer.

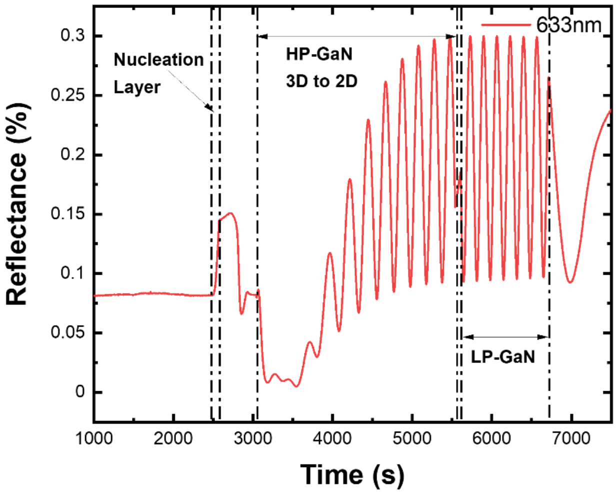

Figure 2.14. *Growth reflectance of 2-step GaN*

In this work, the LT-GaN nucleation layer was grown at 550 °C under the pressure of 450 torr, followed by the HT-GaN grown at 1150 °C, which was divided into two stages, high-pressure (HP) GaN growth (300 torr) and low-pressure (LP) GaN growth (175 torr). The LT-GaN is polycrystalline. After high-temperature annealing, the LT-GaN layer is decomposed and forms GaN islands. Then, the following HT-GaN growth is a process of 3D GaN growth converted to 2D GaN growth with an estimated growth rate of ~0.67 nm/s. Until the growth reflectance was saturated, LP-GaN, with a growth rate of 0.80 nm/s, was involved in reducing the growth time and material cost. Figure 2.14 indicates the reflectance during GaN template growth.

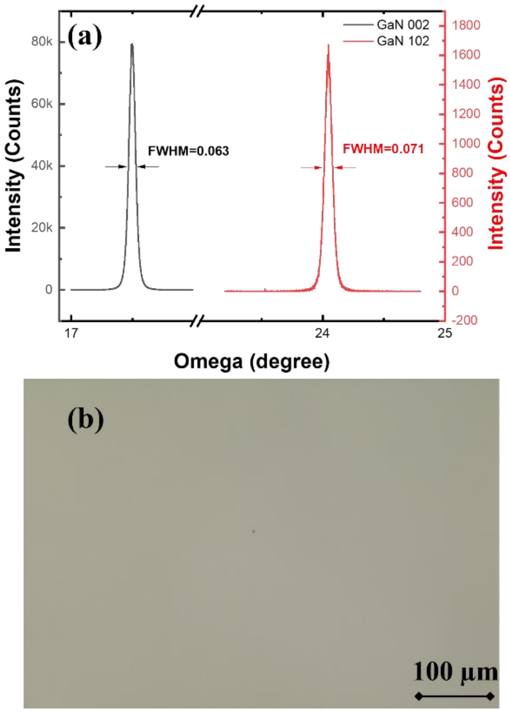

Figure 2.15. *(a) HRXRD (002) and (102) rocking curve measurements; (b) Microscope image of an as-grown n-GaN template.*

Through this technology, high-quality as-grown GaN templates have been prepared. For example, the FWHM of HRXRD (002) and (102) rocking curve measurements of our GaN sample are 0.063 and 0.071, respectively (Figure 2.15a). The XRD results indicate that high-crystal-quality GaN film has been grown. The microscope image collected by Leica DM2700M microscope is shown in Figure 2.15b, displaying a mirror-like surface without any pits and cracking of our as-grown GaN template.

2.3 III-Nitride-Based Optoelectronics

2.3.1 III-Nitride-Based Micro Light-Emitting Diode

III-nitride-based LEDs have been widely used in many fields, such as general lighting, display-screen backlights and traffic signal indicator lights. The typical size of LED chips used in those applications is measured in millimetres. When the size of LED chips is further reduced – for example, to below 100 μm – μLEDs are the result. Because of the advantages of μLEDs, such as uniform current-spreading, high saturation current density, high output optical power density, high display resolution, fast response frequency and high modulation bandwidth, μLEDs have been applied in many fields, including microdisplays such as VR/AR, high-speed visible light communication (VLC) and medical fields such as optogenetics.[56,57]

Table 2.4. *Comparison between μLEDs, LCDs, and OLEDs.*[56]

	μLEDs	**LCDs**	**OLEDs**
Display Type	Emissive	Backlighting	Emissive
Lifetime	>100000 h	30000-60000 h	10000 h
Luminance	$>10^5$ nits	Max. 7×10^3 nits	$<5\times10^3$ nits
Contrast ratio	>1000000:1	5000:1	>1000 00:1
Response time	ns	ms	μs
Pixel size	Submicron	Min. 32 μm	Min. 18 μm
EQE	10%−30% (80% in theory)	5%−12%	10%−40%

In the field of display, compared with LCD and OLED display technologies, μLED displays have the advantages of long life span, high resolution, high brightness, high contrast and fast response time (Table 2.4).[56,57] In the application of visible light communication, the photoelectric modulation bandwidth and communication rate of μLEDs are much higher than those of conventional LEDs.[58,59] In optogenetics, μLEDs array can be integrated on the tip of a needle and inserted into the cerebral cortex of mice with low damage.[60] Because μLED devices are approximately the size of cells, the emission light from μLEDs array can stimulate neurons and control neural networks. They are expected to be used in the treatment of Parkinson's syndrome, blindness and other maladies.[61]

As the next generation of display technology, μLEDs still face many technical challenges. The first is poor extraction efficiency, which limits the EQE. Currently, many techniques are used to enhance the extraction efficiency of μLEDs, such as the back reflector, micro-lenses, and μLED shape design.[62–65] However, the extraction efficiency of μLEDs remains limited and requires further enhancement. The second problem is current-crowding, which causes non-uniform light emission and high efficiency droop. When the injection current is increased, non-uniform light emission becomes more severe, which leads to the low average efficiency of a single μLED device and more efficiency droop.[66] The third (and most critical) issue is sidewall damage during the ICP etching processes.[67] The ratio of the etched sidewall area to the active area increases as μLED dimension decreases, leading to enhanced non-radiative recombination and low internal quantum efficiency (IQE). The ABC model used to calculate the IQE is given by:

$$\eta_{IQE} = \frac{\eta_{inj} B n^2}{An + Bn^2 + Cn^3} \tag{2.11}$$

where A is the non-radiative recombination coefficient, B is the radiative recombination coefficient, C is the Auger recombination coefficient, η_{inj} is the injection current efficiency, and n is the carrier density.[67]

2.3.2 High-Reflectivity Nanoporous Distributed Bragg Reflectors

A traditional distributed Bragg reflector (DBR) is a periodic multi-layer structure consisting of two different materials with different refractive indices.[68] The working principle of a DBR is constructive interference. Therefore, for a specific DBR structure, it can be most efficient at a certain wavelength that corresponds to the constructive interference. The reflectivity of the DBR can be calculated by:

$$R = \left[\frac{n_0(n_2)^{2N} - n_s(n_1)^{2N}}{n_0(n_2)^{2N} + n_s(n_1)^{2N}}\right]^2 \tag{2.12}$$

where N is the number of periods and n_0, n_1, n_2 and n_s represent the refractive indices of the surrounding material, the two alternating materials and the substrate, respectively.[69]

The bandwidth of the photonic stopband can be expressed by:

$$\Delta f_0 = \frac{4f_0}{\pi}\arcsin\left(\frac{n_2 - n_1}{n_2 + n_1}\right) \tag{2.13}$$

where f_0 is the centre frequency of the band.[70]

Thus, increasing the number of periods enhances reflectivity, and increasing the refractive index difference between the two alternating layers can effectively increase reflectivity as well as stopband width.

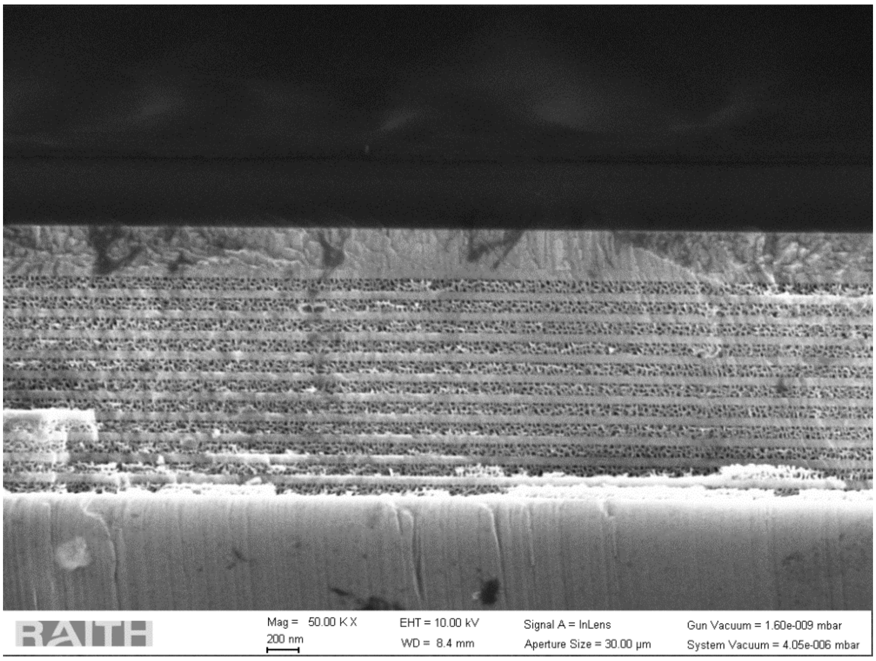

Figure 2.16. *SEM image of nanoporous DBRs.*

In III-nitride semiconductors, the small refractive index contrast between GaN and AlGaN/AlN limits the reflectivity of GaN/AlGaN DBRs.[71,72] To meet the requirement of high reflectivity, the number of periods must be increased, resulting in a high growth cost. For GaN/InAlN DBRs, the difference in refractive index is sufficient. However, the low crystal quality remains a serious challenge.[73] To achieve high reflectivity and high-quality DBRs, a nanoporous GaN/undoped GaN periodical structure was induced.[74] The nanoporous GaN can be fabricated via the electro-chemical (EC) etching process of *n*-type GaN. Figure 2.16 illustrates a typical cross-sectional SEM image of DBR structure fabricated in our group, showing a high density of nanopores. The high density of nanoporous indicates high refractive index contrast, resulting in high reflectivity and broad stopband. A similar DBR structure will also be used in this project to enhance the extraction efficiency of μLEDs, which is introduced in Chapter 5.

2.3.3 III-Nitride-Based Micro Light-Emitting Diodes with Red Emission

There are three ways to achieve III-nitride-based red LEDs. First, they can be achieved via colour conversion by combining LEDs with phosphor or quantum dots. However, the particle size of phosphor is around 1–10 μm, which is quite large in comparison to the dimensions of μLEDs, leading to very low colour conversion efficiency.[75] Thus, quantum dots (QDs) are involved in replacing traditional phosphor in the application of full-colour μLED displays. In 2015, Han showed that the full-colour display could be achieved by applying an advanced aerosol jet printing technique with colloidal quantum dots (CQDs).[76] The particle size of CQD is less than 10 nm – much smaller than the dimensions of μLEDs. Furthermore, the application of the aerosol jet printing technique can achieve high coating uniformity on the surface of μLEDs.[76]

Second, doping GaN with europium (Eu) to achieve red emission is attracting significant attention. In 2010, Nishikawa et al. reported the first *p*-type/Eu-doped/*n*-type GaN LED with an emission wavelength of 621 nm.[77] However, the light output power of GaN:Eu LEDs is limited for the application of display. Thus, they still require further development and have not yet been commercialised.

The third method for achieving III-nitride-based red LEDs is growing high-indium-content multi-quantum wells, a technique that is also used in this project. The involvement of the AlGaN interlayer has dramatically enhanced the optical performance of III-nitride-based red LEDs.[78–80] In 2020, a team in the Kingdom of Saudi Arabia developed a hybrid MQW structure consisting of single blue and double red QWs, achieving an EQE of 1.6%.[81] A 1.2 nm AlN interlayer was also grown on top of the red QW. This team then fabricated red μLEDs with identical hybrid MQWs into different dimensions, achieving a high EQE of 0.56% for 47 μm × 47 μm red μLEDs.[82] Pasayat et al. demonstrated 6 μm × 6 μm ultrasmall 632 nm red μLEDs grown on strain-released porous GaN underlayer, achieving a high EQE of 0.2%.[83] It is clear that with the increase of indium content, the strong QCSE significantly limited the efficiency of red LEDs. Moreover, for the application of red μLEDs, none of these techniques can avoid the sidewall damages incurred during the dry-etching processes for the formation of μLEDs, further reducing efficiency. Therefore, in this project, we developed a new technology that does use dry-etching processes for fabrication to achieve ultrasmall red μLEDs with high EQEs. This breakthrough work is illustrated in Chapter 6.

Reference

1. Sze, S. M.; Lee, M.-K. *Semiconductor Devices Physics and Technology; International Student Version*; Singapore Wiley, 2013.

2. Hook, J. R.; Henry Edgar Hall. *Solid State Physics*; John Wiley, Chichester, 1991.

3. Fox, M. *Optical Properties of Solids*; Oxford University Press: New York, 2012.

4. Agrawal, G. P.; Dutta, N. K. Recombination Mechanisms in Semiconductors. *Semiconductor Lasers* **1993**, 74–146.

5. Hall, R. N. Electron-Hole Recombination in Germanium. *Physical Review* **1952**, *87* (2), 387–387.

6. Shockley, W.; Read, W. T. Statistics of the Recombinations of Holes and Electrons. *Physical Review* **1952**, *87* (5), 835–842.

7. Iveland, J.; Martinelli, L.; Peretti, J.; Speck, J. S.; Weisbuch, C. Direct Measurement of Auger Electrons Emitted from a Semiconductor Light-Emitting Diode under Electrical Injection: Identification of the Dominant Mechanism for Efficiency Droop. *Physical Review Letters* **2013**, *110* (17).

8. Wang, T. Topical Review: Development of Overgrown Semi-Polar GaN for High Efficiency Green/Yellow Emission. *Semiconductor Science and Technology* **2016**, *31* (9), 093003.

9. Pelant, I.; Valenta, J. Luminescence of Disordered Semiconductors. *Luminescence Spectroscopy of Semiconductors* **2012**, 242–262.

10. Kohno, T.; Sudo, Y.; Yamauchi, M.; Mitsui, K.; Kudo, H.; Okagawa, H.; Yamada, Y. Internal Quantum Efficiency and Nonradiative Recombination Rate in InGaN-

Based Near-Ultraviolet Light-Emitting Diodes. *Japanese Journal of Applied Physics* **2012**, *51*, 072102.

11. Nag, B. *Electron Transport in Compound Semiconductors*; Springer Berlin Heidelberg: Berlin, Heidelberg, 1980.

12. Kente, T.; Mhlanga, S. D. Gallium Nitride Nanostructures: Synthesis, Characterization and Applications. *Journal of Crystal Growth* **2016**, *444*, 55–72.

13. Braga, D. Crystal Engineering. A Textbook. By Gautam R. Desiraju, Jagadese J. Vittal and Arunachalam Ramanan. *Angewandte Chemie International Edition* **2012**, *51* (15), 3516–3516.

14. Archilla, J. F. R.; Coelho, S. M. M.; Auret, F. D.; Nyamhere, C.; Dubinko, V. I.; Hizhnyakov, V. Experimental Observation of Intrinsic Localized Modes in Germanium. *Quodons in Mica* **2015**, 343–362.

15. Kwong, F.; Li, L.; Ann, S.; Hass, Z. Gallium Nitride: An Overview of Structural Defects. *Optoelectronics - Materials and Techniques* **2011**.

16. McNally, P. J. 3D Imaging of Crystal Defects. *Nature* **2013**, *496* (7443), 37–38.

17. Wise, R. L.; Lindberg, K. J.; Dyer, L. D.; Huff, H. R. Silicon Epitaxial Layers: Defects. *Encyclopedia of Materials: Science and Technology* **2001**, 8549–8558.

18. Hu, J.; Zhang, Y.; Sun, M.; Piedra, D.; Chowdhury, N.; Palacios, T. Materials and Processing Issues in Vertical GaN Power Electronics. *Materials Science in Semiconductor Processing* **2018**, *78*, 75–84.

19. Hashizume, T. Effects of Mg Accumulation on Chemical and Electronic Properties of Mg-Doped *P*-Type GaN Surface. *Journal of Applied Physics* **2003**, *94* (1), 431–436.

20. Dutta Gupta, S.; Agarwal, A. Artificial Lighting System for Plant Growth and Development: Chronological Advancement, Working Principles, and Comparative Assessment. *Light Emitting Diodes for Agriculture* **2017**, 1–25.

21. Weisbuch, C.; Nakamura, S.; Wu, Y.-R.; Speck, J. S. Disorder Effects in Nitride Semiconductors: Impact on Fundamental and Device Properties. *Nanophotonics* **2020**, *10* (1), 3–21.

22. Hadis Morkoç. *Nitride Semiconductors and Devices*; Springer: Berlin; New York, 1999.

23. Okumura, H.; Ohta, K.; Feuillet, G.; Balakrishnan, K.; Chichibu, S.; Hamaguchi, H.; Hacke, P.; Yoshida, S. Growth and Characterization of Cubic GaN. *Journal of Crystal Growth* **1997**, *178* (1-2), 113–133.

24. Lada, M.; Cullis, A. G.; Parbrook, P. J.; Hopkinson, M. Metastable Rocksalt Phase in Epitaxial GaN on Sapphire. *Applied Physics Letters* **2003**, *83* (14), 2808–2810.

25. Van Camp, P. E.; Van Doren, V. E.; Devreese, J. T. High Pressure Structural Phase Transformation in Gallium Nitride. *Solid State Communications* **1992**, *81* (1), 23–26.

26. Kim, J. H.; Holloway, P. H. Wurtzite to Zinc-Blende Phase Transition in Gallium Nitride Thin Films. *Applied Physics Letters* **2004**, *84* (5), 711–713.

27. Look, D. C.; Sizelove, J. R. Predicted Maximum Mobility in Bulk GaN. *Applied Physics Letters* **2001**, *79* (8), 1133–1135.

28. Blakemore, J. S. Semiconducting and Other Major Properties of Gallium Arsenide. *Journal of Applied Physics* **1982**, *53* (10), R123–R181.

29. Kyuregyan, A. S.; Yurkov, S. N. Room-temperature avalanche breakdown voltages of Si, Ge, SiC, GaAs, GaP and InP. *Sov. Phys. Semicond.* **1989**, *23*, 1126– 1132.

30. Porowski, S. Growth and Properties of Single Crystalline GaN Substrates and Homoepitaxial Layers. *Materials Science and Engineering: B* **1997**, *44* (1-3), 407–413.

31. Glassbrenner, C. J.; Slack, G. A. Thermal Conductivity of Silicon and Germanium from 3°K to the Melting Point. *Physical Review* **1964**, *134* (4A), A1058–A1069.

32. Sze, S. M.; Ng. *Physics of Semiconductor Devices*, Third Edition.; John Wiley & Sons, 2007.

33. Norton, P.; Braggins, T.; Levinstein, H. Impurity and Lattice Scattering Parameters as Determined from Hall and Mobility Analysis inN-Type Silicon. *Physical Review B* **1973**, *8* (12), 5632–5653.

34. *CRC Handbook of Chemistry and Physics*; Haynes, W. M., Lide, D. R., Bruno, T. J., Eds.; CRC Press, 2016.

35. Zhao, D. G.; Yang, H.; Zhu, J. J.; Jiang, D. S.; Liu, Z. S.; Zhang, S. M.; Wang, Y. T.; Liang, J. W. Effects of Edge Dislocations and Intentional Si Doping on the Electron Mobility of N-Type GaN Films. *Applied Physics Letters* **2006**, *89* (11), 112106.

36. Zhuang, D.; Edgar, J. H. Wet Etching of GaN, AlN, and SiC: A Review. *Materials Science and Engineering: R: Reports* **2005**, *48* (1), 1–46.

37. Takeuchi, T.; Sota, S.; Katsuragawa, M.; Komori, M.; Takeuchi, H.; Amano, H.; Akasaki, I. Quantum-Confined Stark Effect due to Piezoelectric Fields in GaInN

Strained Quantum Wells. *Japanese Journal of Applied Physics* **1997**, *36* (Part 2, No. 4A), L382–L385.

38. Praharaj, C. Spontaneous and Piezoelectric Polarization Effects on the Frequency Response of Wurtzite Aluminium Gallium Nitride / Silicon Carbide Heterojunction Bipolar Transistors. *MRS Proceedings* **2008**, *1069*.
39. Bernardini, F. Spontaneous versus Piezoelectric Polarization in III–v Nitrides: Conceptual Aspects and Practical Consequences. *physica status solidi (b)* **1999**, *216* (1), 391–398.
40. Bernardini, F.; Fiorentini, V.; Vanderbilt, D. Spontaneous Polarization and Piezoelectric Constants of III-V Nitrides. *Physical Review B* **1997**, *56* (16), R10024–R10027.
41. Auf der Maur, M.; Pecchia, A.; Penazzi, G.; Rodrigues, W.; Di Carlo, A. Efficiency Drop in Green InGaN/GaN Light Emitting Diodes: The Role of Random Alloy Fluctuations. *Physical Review Letters* **2016**, *116* (2).
42. Nakamura, S. Nobel Lecture: Background Story of the Invention of Efficient Blue InGaN Light Emitting Diodes. *Reviews of Modern Physics* **2015**, *87* (4), 1139–1151.
43. Kim, M.-H.; Schubert, M. F.; Dai, Q.; Kim, J. K.; Schubert, E. F.; Piprek, J.; Park, Y. Origin of Efficiency Droop in GaN-Based Light-Emitting Diodes. *Applied Physics Letters* **2007**, *91* (18), 183507.

44. Hader, J.; Moloney, J. V.; Koch, S. W. Density-Activated Defect Recombination as a Possible Explanation for the Efficiency Droop in GaN-Based Diodes. *Applied Physics Letters* **2010**, *96* (22), 221106.

45. Iveland, J.; Martinelli, L.; Peretti, J.; Speck, J. S.; Weisbuch, C. Direct Measurement of Auger Electrons Emitted from a Semiconductor Light-Emitting Diode under Electrical Injection: Identification of the Dominant Mechanism for Efficiency Droop. *Physical Review Letters* **2013**, *110* (17).

46. Rozhansky, I. V.; Zakheim, D. A. Analysis of Processes Limiting Quantum Efficiency of AlGaInN LEDs at High Pumping. *physica status solidi (a)* **2007**, *204* (1), 227–230.

47. Xie, J.; Ni, X.; Fan, Q.; Shimada, R.; Özgür, Ü.; Morkoç, H. On the Efficiency Droop in InGaN Multiple Quantum Well Blue Light Emitting Diodes and Its Reduction with P-Doped Quantum Well Barriers. *Applied Physics Letters* **2008**, *93* (12), 121107.

48. Vampola, K. J.; Iza, M.; Keller, S.; DenBaars, S. P.; Nakamura, S. Measurement of Electron Overflow in 450 Nm InGaN Light-Emitting Diode Structures. *Applied Physics Letters* **2009**, *94* (6), 061116.

49. Hwang, D.; Mughal, A.; Pynn, C. D.; Nakamura, S.; DenBaars, S. P. Sustained High External Quantum Efficiency in Ultrasmall Blue III–Nitride Micro-LEDs. *Applied Physics Express* **2017**, *10* (3), 032101.

50. Zhu, D.; Wallis, D. J.; Humphreys, C. J. Prospects of III-Nitride Optoelectronics Grown on Si. *Reports on Progress in Physics* **2013**, *76* (10), 106501.

51. Van Vechten, J. A. Quantum Dielectric Theory of Electronegativity in Covalent Systems. III. Pressure-Temperature Phase Diagrams, Heats of Mixing, and Distribution Coefficients. *Physical Review B* **1973**, *7* (4), 1479–1507.

52. Ambacher, O. Growth and Applications of Group III-Nitrides. *Journal of Physics D: Applied Physics* **1998**, *31* (20), 2653–2710.

53. Witek, A. Some Aspects of Thermal Conductivity of Isotopically Pure Diamond—a Comparison with Nitrides. *Diamond and Related Materials* **1998**, *7* (7), 962–964.

54. ing, H.; Keller, S.; Wu, Y-F.; McCarthy, L.; Smorchkova, I. P.; Buttari, D.; Coffie, R.; Green, D. S.; Parish, G.; Heikman, S.; Shen, L.; Zhang, N.; Xu, J. J.; Keller, B. P.; DenBaars, S. P.; Mishra, U. K. Gallium Nitride Based Transistors. *Journal of Physics: Condensed Matter* **2001**, *13* (32), 7139–7157.

55. Liu, L.; Edgar, J. H. Substrates for Gallium Nitride Epitaxy. *Materials Science and Engineering: R: Reports* **2002**, *37* (3), 61–127.

56. Chen, Z.; Yan, S.; Danesh, C. MicroLED Technologies and Applications: Characteristics, Fabrication, Progress, and Challenges. *Journal of Physics D: Applied Physics* **2021**, *54* (12), 123001.

57. Hang, S.; Chuang, C.-M.; Zhang, Y.; Chu, C.; Tian, K.; Zheng, Q.; Wu, T.; Liu, Z.; Zhang, Z.-H.; Li, Q.; Kuo, H.-C. A Review on the Low External Quantum

Efficiency and the Remedies for GaN-Based Micro-LEDs. *Journal of Physics D: Applied Physics* **2021**, *54* (15), 153002.

58. Yu, L.; Wang, L.; Hao, Z.; Luo, Y.; Sun, C.; Xiong, B.; Han, Y.; Wang, J.; Li, H. High-Speed Micro-LEDs for Visible Light Communication: Challenges and Progresses. *Semiconductor Science and Technology* **2021**, *37* (2), 023001.
59. Feezell, D. F.; Monavarian, M.; Rashidi, A.; Nami, M.; Aragon, A. High-Speed GaN-Based Micro-Scale Light-Emitting Diodes for Visible-Light Communication (Conference Presentation). *Wide Bandgap Power and Energy Devices and Applications III* **2018**.
60. Dehkhoda, F.; Soltan, A.; Ramezani, R.; Degenaar, P. Biphasic Micro-LED Driver for Optogenetics. *2016 IEEE Biomedical Circuits and Systems Conference (BioCAS)* **2016**.
61. Zhao, H. Optogenetic Implants. *Handbook of Biochips* **2022**, 179–206.
62. Choi, H. W.; Jeon, C. W.; Dawson, M. D. InGaN Light Emitting Diodes of Micro-Ring Geometry. physica status solidi (c) 2003, No. 7, 2185–2188.
63. Choi, H. W.; Liu, C.; Gu, E.; McConnell, G.; Girkin, J. M.; Watson, I. M.; Dawson, M. D. GaN Micro-Light-Emitting Diode Arrays with Monolithically Integrated Sapphire Microlenses. Applied Physics Letters 2004, 84 (13), 2253–2255.
64. Tan; Zhou; Hu; Wang; Yao. Light Extraction Enhancement of InGaN Based Micro Light-Emitting Diodes with Concave-Convex Circular Composite Structure Sidewall. Applied Sciences 2019, 9 (17), 3458.

65. Hong, I. Y.; Lee, J. H.; Cho, S. M.; So, J. B.; Kim, T. K.; Cha, Y.-J.; Kwak, J. S. Impact of Hydrothermally Grown ZnO Nanorods on External Quantum Efficiency of 32 × 32 Pixelated InGaN/GaN Micro-LED Array. IEEE Transactions on Nanotechnology 2019, 18, 160–166.

66. Tian, P.; McKendry, J. J. D.; Gong, Z.; Guilhabert, B.; Watson, I. M.; Gu, E.; Chen, Z.; Zhang, G.; Dawson, M. D. Size-Dependent Efficiency and Efficiency Droop of Blue InGaN Micro-Light Emitting Diodes. *Applied Physics Letters* **2012**, *101* (23), 231110.

67. Olivier, F.; Daami, A.; Licitra, C.; Templier, F. Shockley-Read-Hall and Auger Non-Radiative Recombination in GaN Based LEDs: A Size Effect Study. *Applied Physics Letters* **2017**, *111* (2), 022104.

68. Schubert, M. F.; Xi, J.-Q.; Kim, J. K.; Schubert, E. F. Distributed Bragg Reflector Consisting of High- and Low-Refractive-Index Thin Film Layers Made of the Same Material. *Applied Physics Letters* **2007**, *90* (14), 141115.

69. Sheppard, C. J. R. Approximate Calculation of the Reflection Coefficient from a Stratified Medium. *Pure and Applied Optics: Journal of the European Optical Society Part A* **1995**, *4* (5), 665–669.

70. Zhang, C.; ElAfandy, R.; Han, J. Distributed Bragg Reflectors for GaN-Based Vertical-Cavity Surface-Emitting Lasers. *Applied Sciences* **2019**, *9* (8), 1593.

71. Huang, G. S.; Lu, T. C.; Yao, H. H.; Kuo, H. C.; Wang, S. C.; Lin, C.-W.; Chang, L. Crack-Free GaN∕AlN Distributed Bragg Reflectors Incorporated with GaN∕AlN Superlattices Grown by Metalorganic Chemical Vapor Deposition. Applied Physics Letters **2006**, 88 (6), 061904.

72. Wu, C. M.; Zhang, B. P.; Shang, J. Z.; Cai, L. E.; Zhang, J. Y.; Yu, J. Z.; Wang, Q. M. High-Reflectivity AlN/GaN Distributed Bragg Reflectors Grown on Sapphire

Substrates by MOCVD. Semiconductor Science and Technology **2011**, 26 (5), 055013.

73. Sadler, T. C.; Kappers, M. J.; Oliver, R. A. Optimisation of GaN Overgrowth of InAlN for DBRs. *physica status solidi c* **2009**, *6* (S2).

74. Zhang, C.; Park, S. H.; Chen, D.; Lin, D.-W.; Xiong, W.; Kuo, H.-C.; Lin, C.-F.; Cao, H.; Han, J. Mesoporous GaN for Photonic Engineering—Highly Reflective GaN Mirrors as an Example. *ACS Photonics* **2015**, *2* (7), 980–986.

75. Chen, D.-C.; Liu, Z.-G.; Deng, Z.-H.; Wang, C.; Cao, Y.-G.; Liu, Q.-L. Optimization of Light Efficacy and Angular Color Uniformity by Hybrid Phosphor Particle Size for White Light-Emitting Diode. *Rare Metals* **2014**, *33* (3), 348–352.

76. Han, H.-V.; Lin, H.-Y.; Lin, C.-C.; Chong, W.-C.; Li, J.-R.; Chen, K.-J.; Yu, P.; Chen, T.-M.; Chen, H.-M.; Lau, K.-M.; Kuo, H.-C. Resonant-Enhanced Full-Color Emission of Quantum-Dot-Based Micro LED Display Technology. *Optics Express* **2015**, *23* (25), 32504.

77. Nishikawa, A.; Kawasaki, T.; Furukawa, N.; Terai, Y.; Fujiwara, Y. Electroluminescence Properties of Eu-Doped GaN-Based Red Light-Emitting Diode by OMVPE. *physica status solidi (a)* **2010**, *207* (6), 1397–1399.

78. Shioda, T.; Yoshida, H.; Tachibana, K.; Sugiyama, N.; Nunoue, S. Enhanced Light Output Power of Green LEDs Employing AlGaN Interlayer in InGaN/GaN MQW Structure on Sapphire (0001) Substrate. *physica status solidi (a)* **2012**, *209* (3), 473–476.

79. Alhassan, Abdullah. I.; Young, Nathan. G.; Farrell, Robert. M.; Pynn, Christopher.; Wu, Feng.; Alyamani, Ahmed. Y.; Nakamura, S.; DenBaars, Steven. P.; Speck, James. S. Development of High Performance Green C-Plane III-Nitride Light-Emitting Diodes. *Optics Express* **2018**, *26* (5), 5591.

80. Hwang, J.-I.; Hashimoto, R.; Saito, S.; Nunoue, S. Development of InGaN-Based Red LED Grown on (0001) Polar Surface. *Applied Physics Express* **2014**, *7* (7), 071003.

81. Iida, D.; Zhuang, Z.; Kirilenko, P.; Velazquez-Rizo, M.; Najmi, M. A.; Ohkawa, K. 633-nm InGaN-Based Red LEDs Grown on Thick Underlying GaN Layers with Reduced In-Plane Residual Stress. *Applied Physics Letters* **2020**, *116* (16), 162101.

82. Zhuang, Z.; Iida, D.; Velazquez-Rizo, M.; Ohkawa, K. 606-nm InGaN Amber Micro-Light-Emitting Diodes with an On-Wafer External Quantum Efficiency of 0.56%. *IEEE Electron Device Letters* **2021**, *42* (7), 1029–1032.

83. Pasayat, S. S.; Gupta, C.; Wong, M. S.; Ley, R.; Gordon, M. J.; DenBaars, S. P.; Nakamura, S.; Keller, S.; Mishra, U. K. Demonstration of Ultra-Small (<10 µm) 632 nm Red InGaN Micro-LEDs with Useful On-Wafer External Quantum Efficiency (>0.2%) for Mini-Displays. *Applied Physics Express* **2020**, *14* (1), 011004.

Chapter 3

Experimental Equipment

3.1 Fabrication Technology

3.1.1 Plasma-Enhanced Chemical Vapour Deposition

Plasma-enhanced chemical vapour deposition (PECVD) is a professional thin-film deposition equipment that is widely used for SiO_2 or SiN deposition. In this work, SiO_2 dielectric films are deposited by a Plasma-Therm 790 PECVD system, as shown in Figure 3.1. During the deposition process, a mixture of SiH_4, N_2O and N_2 is flown into the chamber with a reactor temperature of 300 °C and a reactor pressure of 900 mTorr. Under radio frequency, the mixture gases are ionised and generate plasma which has very high chemical activity and promotes the chemical reaction.[1] Through this technology, high-quality SiO_2 films can be fabricated on templates. The reaction formula is given by:

$$SiH_4 + 2N_2O \rightarrow SiO_2 + 2H_2 + 2N_2 \tag{3.1}$$

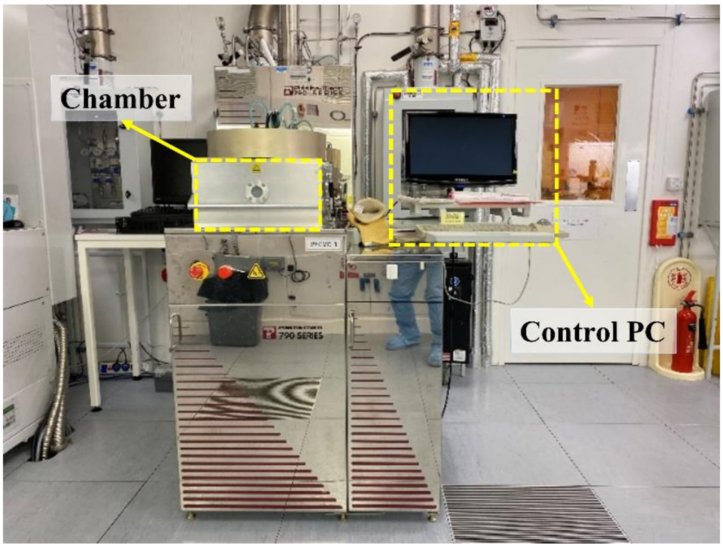

Figure 3.1. *Plasma-Therm 790 PECVD system.*

The SiO_2 deposition rate is changing with time goes by as the equipment conditions are changing. Hence, a small GaN on sapphire wafer is used as a reference sample to test the deposition rate before we deposit SiO_2 on our μLED templates. In detail, we use SEM to check the cross-section of reference sample and measure the SiO_2 thickness to get the accurate deposition rate.

3.1.2 Photolithography

Photolithography is a technology used to transfer a designed pattern from a photomask to a photoresist to provide patterned access to the substrate underneath. Initially, a SPRS350 positive photoresist is deposited onto the template with SiO_2. In this step, a spinner is used to spin the template with the photoresist and form a uniform photoresist layer. The sample is then placed on the heater at 100 °C to solidify the photoresist. Next, the Karl Suss MJB3 UV400 Mask Aligner, shown in Figure 3.2, is used to do UV exposure photolithography. The positive photoresist, which is exposed to UV light, becomes hydrophilic and easily removable by a developer.[2] An MF26A developer is involved in this step. The 3.6 μm and 2 μm μLED templates were both fabricated by this mask aligner. Because of the wafer bowing, it was very difficult to achieve the uniform 2 μm circular pattern cross the whole 2-inch wafer. Hence, we removed the the pattern in the edge of wafer and then got better 2 μm μLED templates.

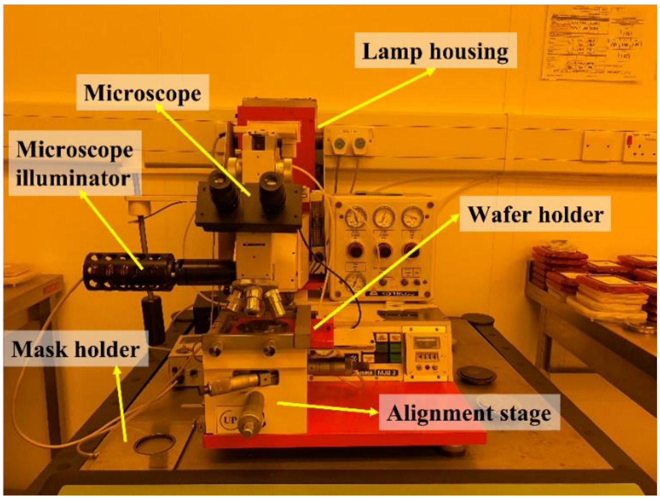

Figure 3.2. *The Karl Suss MJB3 UV400 Mask Aligner.*

3.1.3 Inductively Coupled Plasma RIE

Inductively coupled plasma reactive ion etching (ICP-RIE) is a widely used etch technology that combines chemical reactions and ion-induced etching under high-density plasma. Figure 3.3 shows the Oxford Instruments Plasmalab 100 ICP-RIE system used in this project to etch the SiO_2 during the μLEDs template fabrication processes. The SiO_2 is etched under CHF_3, and Ar mixed gases with flow rates of 20 sccm and 30 sccm, respectively. The reactor pressure is 25 mTorr, and the etching power is 200W. The etching rate of our ICP is not stably as well. We also used a test sample test the etching rate before any ICP etching process.

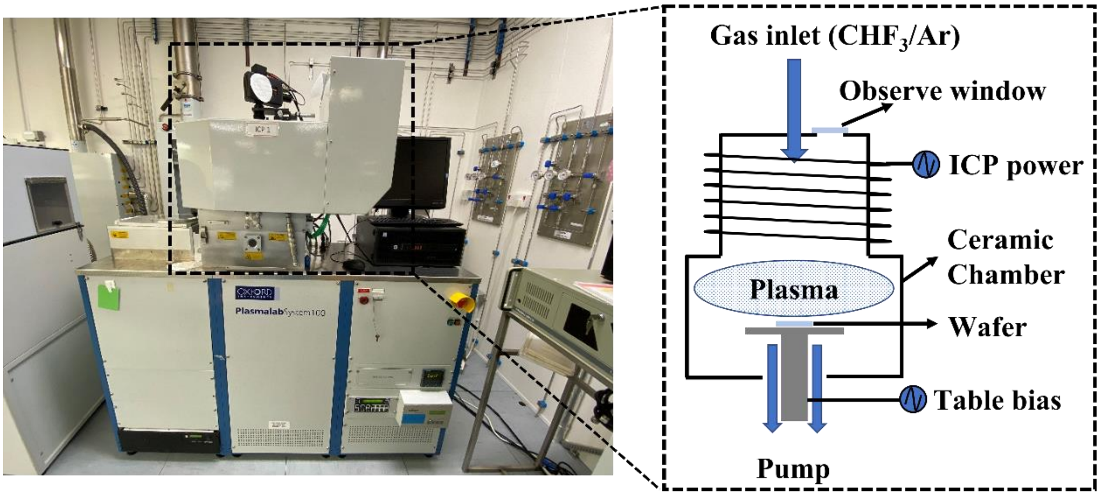

Figure 3.3. *The Oxford Instruments Plasmalab 100 ICP system.*

3.1.4 Sample Treatment

During the μLED template fabrication processes, many contaminants may be absorbed into the μLEDs template. Thus, it is important to run a cleaning treatment before MOCVD overgrowth. First, the μLED template was cleaned sequentially with n-butyl, acetone, and IPA for 15 minutes each in an ultrasonic bath to remove contaminants. Subsequently, the μLED template was placed in a 10% KOH solution under UV illumination for 40 minutes to smooth the patterned n-GaN surface.[3] Figure 3.4 shows the scanning electron microscope (SEM) images of the n-GaN surface after 5 minutes, 10 minutes, 20 minutes and 40 minutes of KOH etching time under UV. It is evident that the number of black points, which are physical damages caused by the dry-etching process, is decreased with the increase of KOH etching time, and is entirely eliminated after 40 minutes of etching. Afterward, 37% HCl solution was used to remove residual KOH and other metal pollutants from the μLED template. Finally, after DI water cleaning, the μLED template was ready for the confined selective epitaxy by MOCVD.

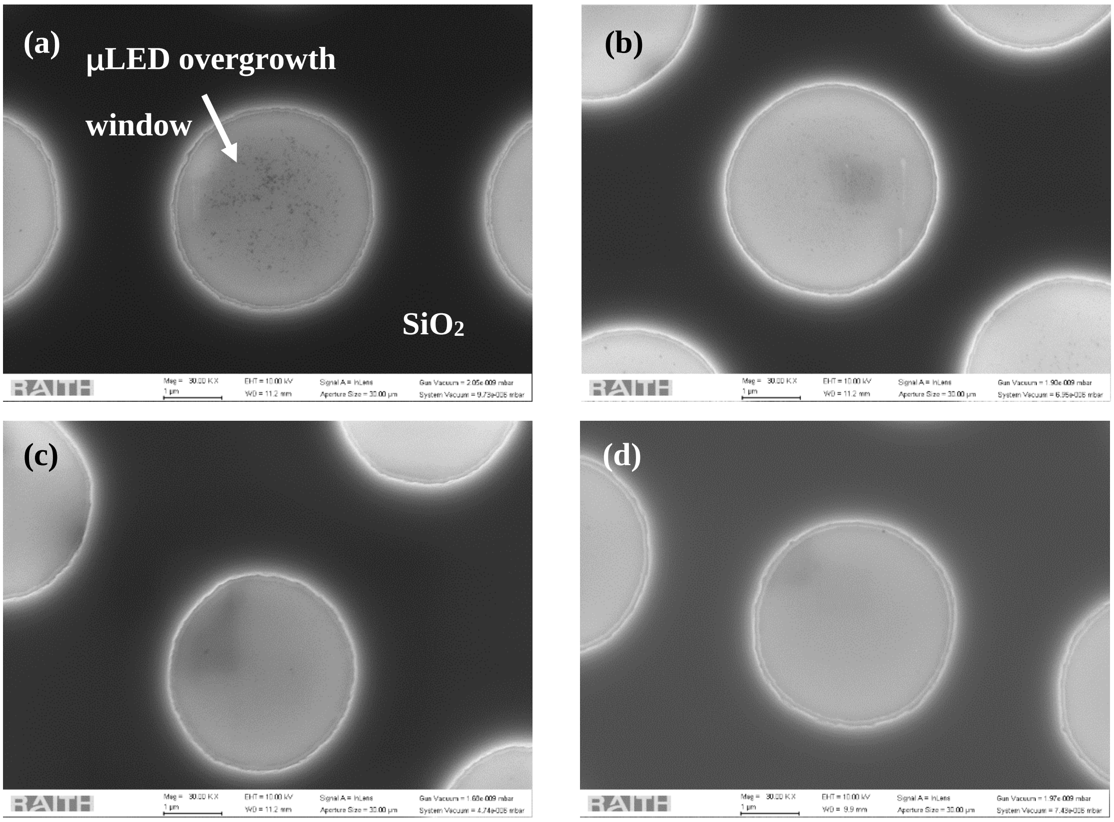

Figure 3.4. *SEM images of the n-GaN surface after (a) 5 minutes, (b) 10 minutes, (c) 20 minutes and (d) 40 minutes of KOH etching under UV.*

3.2 Metal–Organic Chemical Vapour Deposition

Metal–organic chemical vapour deposition (MOCVD), also commonly known as metal–organic vapour-phase epitaxy (MOVPE), is a vapour-phase epitaxy technology that uses organic compounds of group II and III elements as well as hydrides of group V and VI elements as source materials to grow thin-layer monocrystalline III–V or II–

VI compound semiconductor materials on various substrates.[4] Figure 3.5 shows the main body of the Thomas Swan MOCVD system, which is used in this project for the growth of III-nitride semiconductors. There is another Aixtron CCS MOCVD system in our group. However, the temperature stability between different growth runs is worse than our Thomas Swan MOCVD system. As a result, it is very hard to repeat the LED growth runs. Hence, I chose the Thomas Swan MOCVD system to do this project.

Figure 3.5. *Thomas Swan CS1664 MOCVD system.*

The Thomas Swan MOCVD system consists of the system control panel, gas circuit cabinet, glovebox cabinet with reactor chamber, and load lock cabinet. The system control panel on the left of the MOCVD system contains many important control units, such as the system power switch, emergency stop switch, 24V safety system with 11 interlocks, and programmable logic circuit (PLC). The system power switch is used to turn the whole MOCVD system's power supply on or off. The reactor can be immediately shut down by pressing the emergency stop switch. The 11 interlocks are: extract air, pneumatic air, access panel, H_2 detected in glovebox, reactor closed, reactor overpressure, scrubber, H_2 detected, low H_2 manifold pressure, low N_2 manifold pressure, and water flow. Any interlock problem will trip the 24V off and automatically switch the whole system into N_2 safety mode. Other essential units, such as heater power, wafer rotation, pressure controller, recirculation pump, regeneration pump, load lock pump, pyrolysis furnace and Ebara pump controller, are in the control panel on the right of the MOCVD system. All can be safely switched on or off using the control switch on this control panel.

The gas circuit cabinet contains the gas delivery circuit of ammonia (NH_3), disilane (Si_2H_6), and metal–organic (MO) sources. The gas circuit diagram of the whole MOCVD system is illustrated in Figure 3.6. The upper carrier and lower carrier are used to deliver the NH_3 and MO sources, respectively, to prevent the reaction from occurring before the reactor is reached. There are also two vent gas circuits: the upper vent and the lower vent. The NH_3 will be delivered to the exhaust via the upper vent until the flow rate is stable, after which it will flow to the reactor via upper carrier. A manifold is designed to control the delivery of all MO sources and Si_2H_6 by switching gas flow between a vent line and a lower carrier line. MO sources are installed in refrigerated baths with thermo-regulators at the bottom of the gas circuit cabinet to maintain a stable source temperature for growth. The gas circuit of the Thomas Swan MOCVD system used in this project is attached in the Appendix Figure 1.

Table 3.1. *Partial pressures and other constants of MO sources.*[5–8]

MO sources	**Temperature (K)**	**A**	**B**	**$P_{partial}$ (torr)**	**$P_{bubbler}$ (torr)**
$TMG_{1,2}$	273	1703	8.07	67.91	1300
TMA_1	291	2134	8.224	7.70	1500
TMA_2	294	2134	8.224	9.15	1500
$TMIn_{1,2}$	303	3204	10.98	2.67	1000
CP_2Mg	303	4198	25.14	0.07	900

In this MOCVD system, for the growth of III-nitride materials, trimethylgallium (TMGa), trimethylindium (TMIn), trimethylaluminum (TMAl), and bis(cyclopentadienyl)magnesium (CP2Mg) sources are installed. The refrigerated bath and thermo-regulator are used to maintain an appropriate temperature of the MO source.

The source pressure is controlled by a pressure controller in the output line of the MO source. The partial pressure of a MO source is given by:

$$\log(P_{partial}) = B - {}^{A}/_{T} \tag{3.2}$$

where $P_{partial}$ is the partial pressure, A and B are material constants of the MO source, and T is the temperature in Kelvin. [5–7] This relationship is slightly changed to:

$$\log(P_{partial}) = B - {}^{A}/_{T} - 2.18 \ln T \tag{3.3}$$

when it is applied on CP2Mg.[8] Table 3.1 illustrates the partial pressures and other constants of our MO sources. The mole flow rate is given by:

$$f_{MO}(mole/min) = \frac{f_{carrier\ gas}\ (sccm)}{22400\ (sccm/mole)} \cdot \frac{P_{partial}\ (torr)}{P_{source} - P_{partial}\ (torr)} \tag{3.4}$$

where $f_{carrier\ gas}$ is the carrier gas flow rate, $P_{partial}$ is the partial pressure, and P_{source} is the source pressure.

The following formula illustrates the chemical reactions of GaN.[9]

$$Ga(CH_3)_3 + NH_3 \rightarrow GaN + 3CH_4 \tag{3.5}$$

The reactor chamber is placed in a glovebox where the atmosphere is isolated to achieve a deeply pure environment with low oxygen and moisture. When a sample needs to be transferred out of the reactor, a load lock system is involved. The sample is initially put in the load lock chamber, which was pre-purged four times by pure N_2, and is then moved out. In this process, there is no direct connection between the glovebox and the outside environment.

Figure 3.6 illustrates the reactor chamber of our Thomas Swan MOCVD. The showerhead is divided into upper showerhead and lower showerhead. The upper showerhead is connected to the MO source line, and the lower showerhead is connected to the NH_3 line. This design is intended to prevent pre-reaction and ensure that the reaction occurs only inside the chamber. There are four optical ports on the top of the reactor chamber. These optical ports provide an essential optical entrance for the in-situ monitoring laser, which is placed on the top of the MOCVD. In this MOCVD system, a LayTec EpiCurve TT is involved as in-situ monitoring. Three different lasers – 405 nm, 633 nm, and 950 nm – are used to monitor the growth reflectivity and other significant parameters during growth.

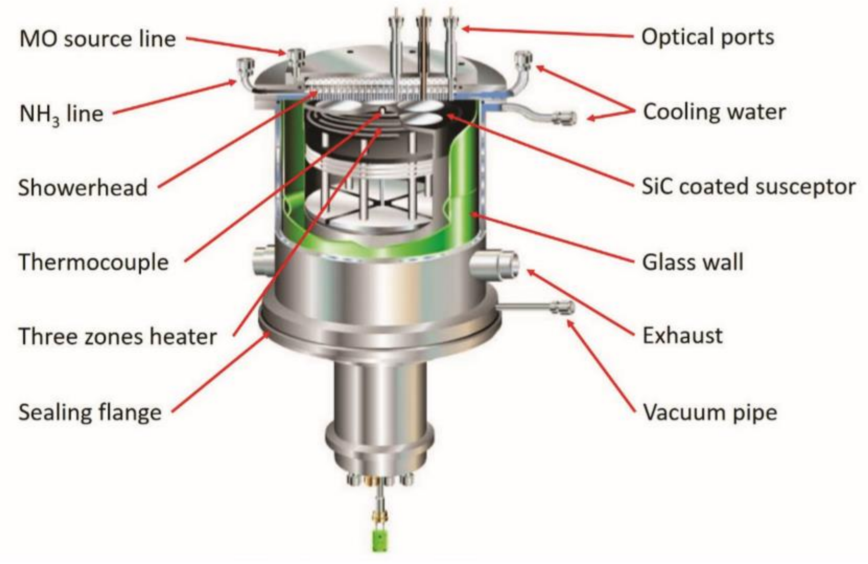

Figure 3.6. *Reactor Chamber of Thomas Swan MOCVD.*[10]

The cooling water is connected to an Affinity chiller to control showerhead temperature during growth. The samples are placed on the 3 × 2 inch SiC-coated susceptor above the three-zone heater. Susceptor temperature uniformity is controlled by adjusting power to each of the three zones. A thermocouple is located below the susceptor to monitor the temperature, and the reactor is sealed by the sealing flange and double O-ring (DOR) sealing. The vacuum pipe is used to check the leakage between the DOR to ensure the seal.

Both carrier gases (H_2 and N_2) and NH_3 must be purified before flowing into the MOCVD reactor. A palladium membrane cell purifier, illustrated in Figure 3.7, is used to purify H_2 for this MOCVD system. The palladium membrane cell is heated to 400 °C, and only H_2 is allowed to pass through the membrane due to its small molecular size. As a result, the purified H_2 is extremely clean, and it is the best choice of carrier gas for MOCVD growth.

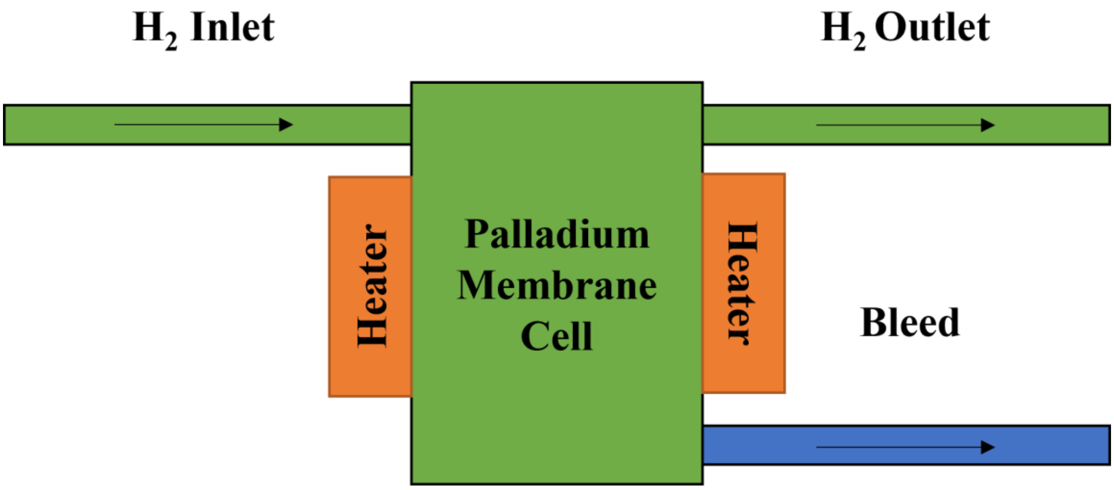

Figure 3.7. *Schematic of the palladium membrane cell purifier.*

However, InGaN must be grown under N_2 ambient. Thus, a Nanochem L-2000 purifier with a 0.0003 μm particle filter is employed to remove H_2O, O_2 and CO_2 for the purification of N_2. The ammonia source used in our group is white ammonia with a high purity of 99.99999%; it is also further purified by a Nanochem MS-8000 purifier.

3.3 Characterisation Technology

3.3.1 Normarski Microscopy

The schematic of a Nomarski optical microscope is shown in Figure 3.8a. Through a polariser, the input light is initially converted into linearly polarised light. Next, the linearly polarised light is separated into two orthogonal components by a Normarski wedge (also called a Wollaston prism). Next, these two orthogonal polarised lights are focused on the sample through an objective lens. The reflective lights can then be focused and mixed on the interface plane of the Normarski wedge, after which the mixed lights pass through an analyser and finally on to the eyepiece, generating three-dimensional (3D) images by the contrast difference generated from the path difference between two orthogonal lights. The Leica DM2700M Normarski microscope used in my research is shown in Figure 3.8b.

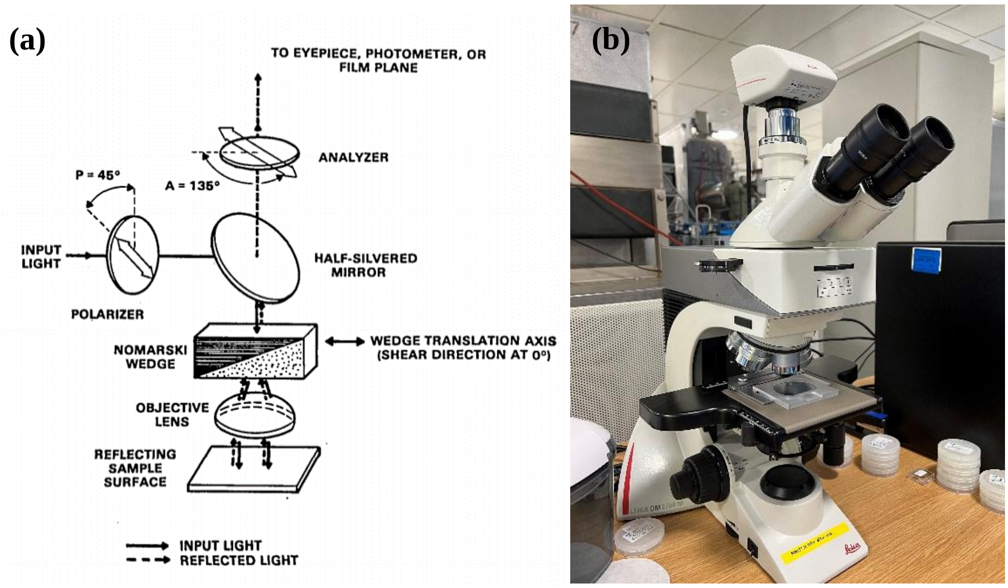

Figure 3.8. *(a) Schematic diagram of a Nomarski microscope*[11] *and (b) Leica DM2700M microscope.*

3.3.2 High-Resolution X-Ray Diffraction (HRXRD)

The basic physics mechanism of high-resolution X-ray diffraction equipment is Bragg's law.[12] Figure 3.9 illustrates the schematic of Bragg's law. When an X-ray beam is incident onto a single-crystal material, wave diffraction can be generated because of the existence of ordered crystalline structures. As shown in Figure 3.10, when the X-ray beams are reflected by different planes, extra path lengths occur between different beams. The path difference between beam 1 and beam 2 is $2dsin\theta$. When the path difference is equal to the integral multiple of the wavelength, constructive interference is generated.

This is illustrated by Bragg's law:[12]

$$2dsin\theta = n\lambda \tag{3.6}$$

where d is the distance between crystal planes, θ is the scattering angle, n is the order of diffraction, and λ is the wavelength of incident X-ray.

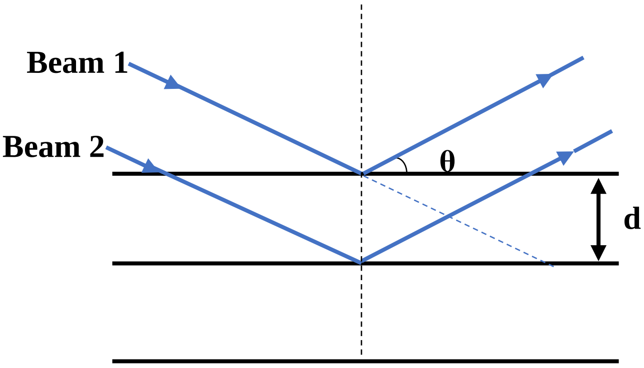

Figure 3.9. *Illustration of Bragg's law.*

The XRD used in this project is a Bruker D8 high-resolution X-ray diffractometer, as shown in Figure 3.10, which has a Cu $K-\alpha$ X-ray generator to provide an X-ray beam with a wavelength of 1.5418Å. The primary optics unit is formed by a Goebel mirror, a monochromator, and a Soller slit. The Goebel mirror is involved in collimating the X-ray beam, followed by a monochromator used to select the wavelength of the X-ray beam. The Soller slit is used to limit the divergence of the incident X-ray beam. Next, the X-ray goes to a sample stage that can be rotated at various angles such as phi, psi and omega. The diffracted X-ray beam then passes through the secondary optics unit, which is similar to the primary optics unit, and is eventually collected by the detector.

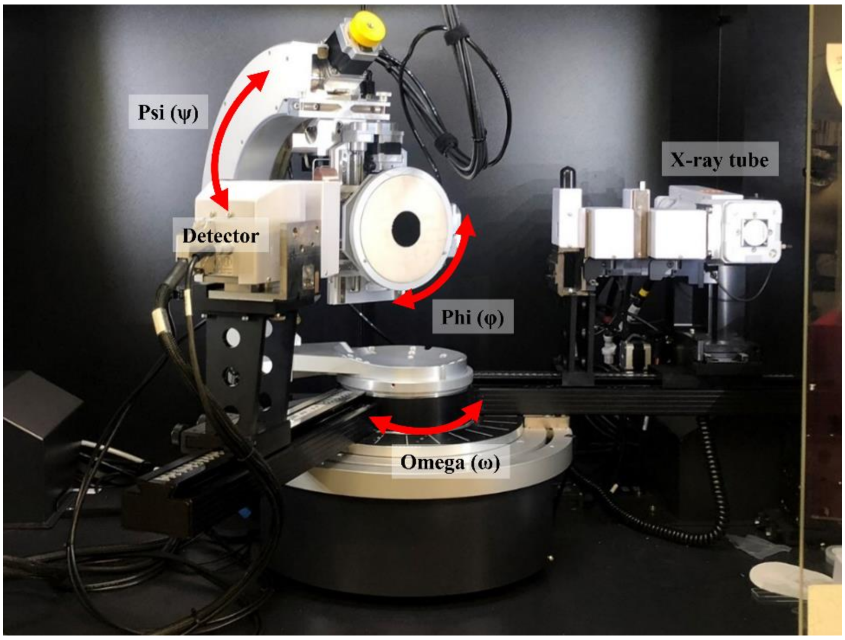

Figure 3.10. *Bruker D8 high-resolution X-ray diffractometer.*

This project makes frequent use of XRD rocking curve measurements to investigate the crystal quality of III-nitride-based semiconductors. The diffraction intensity as a function of omega angle at a specific crystal orientation is measured in this process. A high crystal quality can be identified by a narrow full width at half maximum (FWHM) of the XRD peak. The omega-2theta measurements are generally used to evaluate the composition and thickness of periodical structures like multi-quantum wells (MQWs). The total thickness of one pair of MQWs can be calculated via the equation below[13]:

$$\mathrm{T} = \frac{(n_1 - n_2)\lambda}{2(sin\theta_1 - sin\theta_2)} \tag{3.7}$$

where θ_1 and θ_2 are the angles for two satellite peaks and $n_1 - n_2$ is the number of satellite peaks that come from the MQWs structure between these two satellite peaks.

3.3.3 Photoluminescence

Photoluminescence (PL) spectroscopy is a common technique for investigating the optical properties of semiconductor optoelectronics; the physical mechanism of PL measurements is spontaneous emission.[14] When a laser photon with higher photon energy than the bandgap energy of the semiconductor material is absorbed by the semiconductor material, a free electron can be excited from the valence band to the conduction band, and a hole can be generated in the valence band. The free electrons generated in this way are short-lived. As a result, free electrons automatically recombine with holes in the valence band and generate photons; this phenomenon is called ‘spontaneous emission’.

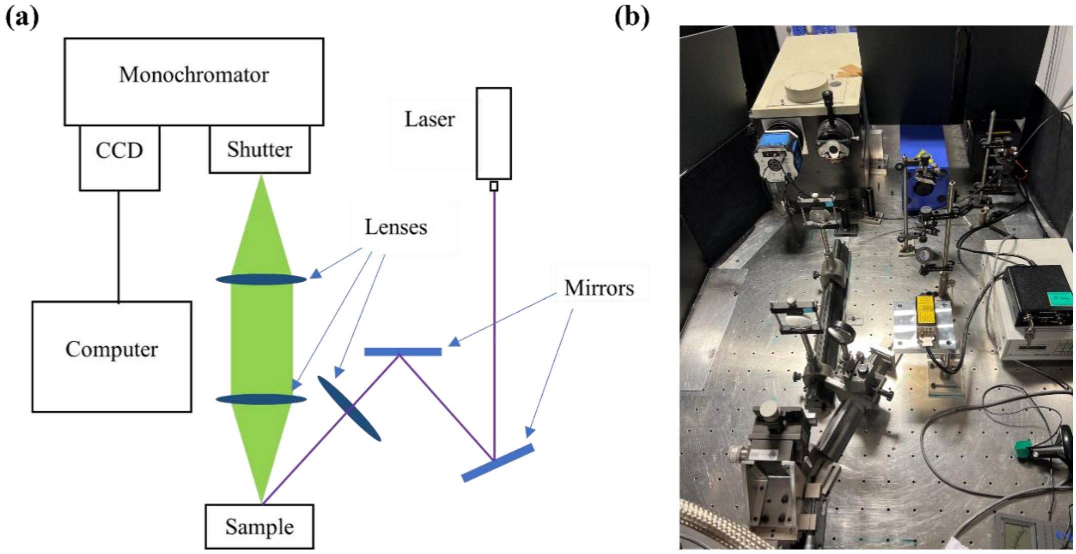

Figure 3.11. *(a) Schematic illustration of the PL system and (b) the homemade PL system.*

In this project, a 375 nm laser is used to characterise III-nitride-based μLED samples. As indicated in Figures 3.11a and 3.11b, our PL system consists of a Vortran Stradus 375 nm laser diode, a sample stage with the cryostat, a SPEX 500M monochromator, a thermoelectrically cooled charge-coupled device (CCD) detector, a computer, and other mirrors and lenses. The laser beam is initially reflected by aluminium-coated mirrors with high reflectivity (>99%) and then focused on the sample by a lens. The diameter of the laser beam can be focused down to 200 μm. The sample stage is combined with a helium (He) closed-cycle cryostat and a thermal controller, which can adjust the sample temperature from 10K to 300K (room temperature), thereby facilitating temperature-dependent PL measurement (TDPL). The next two lenses collect and focus the PL emission light into the monochromator. The optical dispersion is then collected by the CCD and transferred to the computer, generating the optical spectrum of the PL emission

Temperature-dependent PL measurement is a useful method for estimating the IQE of an LED sample. The IQE of an LED sample is defined as the ratio of the photons internally generated to electrons injected in.[15] At extremely low temperatures (like 10K), non-radiative recombination is very weak and nearly vanishes. Therefore, it can be assumed that only radiative recombination occurs at 10K, assuming in 100% IQE. Next, the IQE at room temperature can be calculated by the integrated PL intensity of a LED sample at 300K divided by the integrated PL intensity at 10K.[16] Although this method cannot provide an accurate IQE value, the scaled IQE value is maximum possible value. However, the estimated IQE value can still be used to evaluate the optical performance of LED samples and has become the most common method of characterising LEDs.

3.3.4 Scanning Electron Microscopy

The scanning electron microscope is a type of high-resolution microscope that uses a high-energy electron beam as an illumination source to examine submicron structures under high magnification. As shown in Figure 3.12a, the high-energy electron beam is generated from the electron gun on the top of the SEM system. The whole SEM chamber is under a high vacuum ambient, normally 5×10^{-5} mBar, to prevent electron scattering. The electron beam passes through various magnetic condenser lenses to be collimated and focused on the sample surface. After the bombardment of the electron beam on the sample surface, secondary electrons, continuum X-ray, characteristic X-ray, Auger electrons, backscattered electrons, etc. are generated and subsequently detected by the secondary electron detector or X-ray detector. A reconfigured Raith EO SEM (shown in Figure 3.12b) is used in this project.

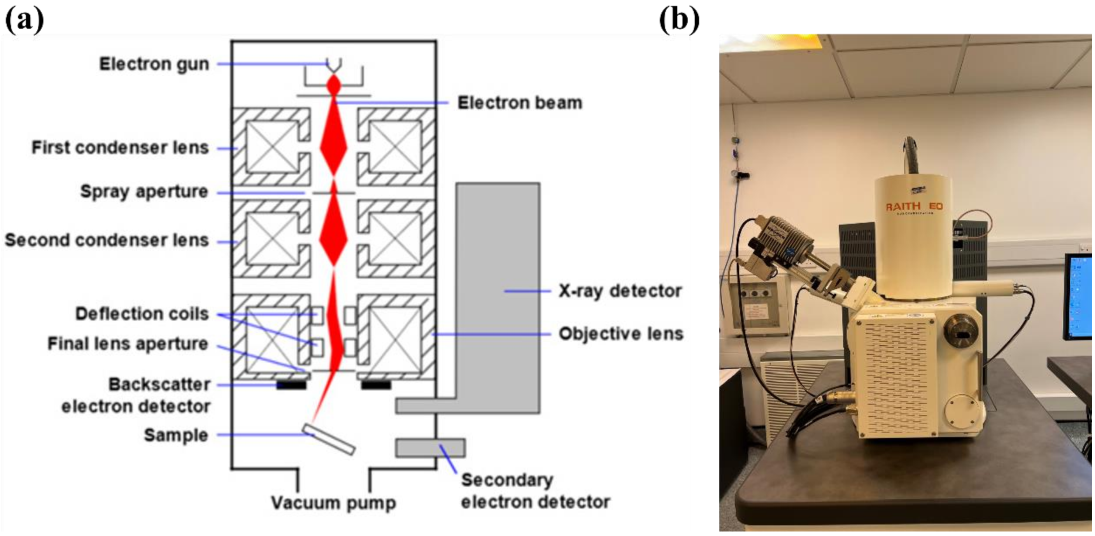

Figure 3.12. *(a) Demonstration of SEM working principle*[17] *and (b) the Raith EO SEM system.*

Reference

1. Chanana, R. K.; Dwivedi, R.; Srivastava, S. K. Effect of Annealing and Plasma Precleaning on the Electrical Properties of N2O/SiH4 PECVD Oxide as Gate Material in MOSFETs and CCDs. *Solid-State Electronics* **1993**, *36* (7), 1021–1026.

2. Dill, F. H.; Hornberger, W. P.; Hauge, P. S.; Shaw, J. M. Characterization of Positive Photoresist. *IEEE Transactions on Electron Devices* **1975**, *22* (7), 445–452.

3. Youtsey, C.; Adesida, I.; Romano, L. T.; Bulman, G. Smooth N-Type GaN Surfaces by Photoenhanced Wet Etching. *Applied Physics Letters* **1998**, *72* (5), 560–562.

4. Thompson, A. G. MOCVD Technology for Semiconductors. *Materials Letters* **1997**, *30* (4), 255–263.

5. TMGa SSG Trimethylgallium; CAS RN: 1445-79-0; Rev. 1; Nouryon; September 20, 2021. https://www.nouryon.com/globalassets/inriver/resources/pds-tmga-ssg-electronics-glo-en.pdf (accessed 2022-08-25).

6. TMAl SSG Trimethylaluminum, CAS RN: 75-24-1; rev. 1; Nouryon; September 20, 2021.https://www.nouryon.com/globalassets/inriver/resources/pds-tmal-ssg-electronics-glo-en.pdf (accessed 2022-08-25).

7. TMIn SSG Trimethylindium; CAS RN: 3385-78-2; rev. 1; Nouryon; September 20, 2021. https://www.nouryon.com/globalassets/inriver/resources/pds-tmin-ssg-electronics-glo-en.pdf (accessed 2022-08-25).

8. Cp2Mg SSG Bis(cyclopentadienyl)magnesium; CAS RN: 1284-72-6; rev. 1; Nouryon; September 20, 2021.

https://www.nouryon.com/globalassets/inriver/resources/pds-cp2mg-ssg-electronics-glo-en.pdf (accessed 2022-08-25).

9. Solomon, G. S.; Miller, D. J.; Ramsteiner, M.; Trampert, A.; Brandt, O.; Ploog, K. H. Combined Hydride and Metal Organic Vapor-Phase Epitaxy of GaN on Sapphire. *Applied Physics Letters* **2005**, *87* (18), 181912.

10. Thomas Swan CCS-MOCVD Reactor System Manual by Thomas Swan Scientific Equipment LTD. 2007.

11. Lessor, D. L.; Hartman, J. S.; Gordon, R. L. Quantitative Surface Topography Determination by Nomarski Reflection Microscopy I Theory. *Journal of the Optical Society of America* **1979**, *69* (2), 357.

12. Moram, M. A.; Vickers, M. E. X-Ray Diffraction of III-Nitrides. *Reports on Progress in Physics* **2009**, *72* (3), 036502.

13. Zhou, D.; Usher, B. F. X-Ray Diffraction Simulation of Strained InGaAs/AlGaAs Multiple Quantum Wells Grown by Molecular Beam Epitaxy. COMMAD 2000 Proceedings. *Conference on Optoelectronic and Microelectronic Materials and Devices.*

14. Reshchikov, M. A.; Morkoç, H. Luminescence Properties of Defects in GaN. *Journal of Applied Physics* **2005**, *97* (6), 061301.

15. Pimputkar, S.; Speck, J. S.; DenBaars, S. P.; Nakamura, S. Prospects for LED Lighting. *Nature Photonics* **2009**, *3* (4), 180–182.

16. Seetoh, I. P.; Soh, C. B.; Zhang, L.; Patrick Tung, K. H.; Fitzgerald, E. A.; Jin Chua, S. Improvement in the Internal Quantum Efficiency of InN Grown over Nanoporous GaN by the Reduction of Shockley-Read-Hall Recombination Centers. *Applied Physics Letters* **2013**, *103* (12), 121903.

17. Scanning electron microscope https://en.wikipedia.org/wiki/Scanning_electron_microscope#/media/File:Schema_MEB_(en).svg.

Chapter 4

Direct Epitaxial Growth to Achieving III-Nitride μLEDs on a Patterned Template

This chapter demonstrates the development of a creative “confined selective epitaxy" (CSE) approach used to produce III-nitride-based micro light-emitting diodes (μLEDs). In contrast to traditional methods for the fabrication of μLEDs, dry-etching processes are not involved in this new technique of fabricating μLED arrays. Therefore, the sidewall damages incurred during the dry-etching processes are eliminated. In this work, the design and fabrication of patterned templates are optimised in terms of dimension, filling factor and etching depth for the application of confined selective epitaxy. Subsequently, the n-GaN and p-GaN optimisation of μLED overgrowth structures are processed and discussed. Ultimately, ultrasmall, high-efficient and ultracompact green μLEDs with a diameter of 3.6 μm and an interpitch of 2 μm have been demonstrated. The IQE of these μLED arrays is measured to be 28% by temperature-dependent photoluminescence (TDPL). Our μLED device shows a high EQE of 6% at the emission wavelength of 515 nm and high luminance of $>10^7$ cd/m^2.

4.1 Introduction

As introduced in previous chapters, there is a significant increase in the demand for the development of III-nitride-based visible μLEDs as next generation display technology.[1-4]In general, different μLEDs applications have different requirements for dimension. A dimension of <100 μm is required for autodisplay and next-generation TV applications, while other applications require a dimension of <50 μm (ideally ≤10 μm). Specifically, AR/VR devices require μLEDs with a dimension of <5 μm to achieve high resolution. Because of the decreased dimension, the junction capacitance of μLEDs is dramatically reduced compared with conventional broad-area LEDs.

Therefore, μLEDs are perfect for high-speed data transmission VLC applications with a GHz modulation bandwidth.[5,6] However, there are also some challenges in this applications. First, the QCSE of III-nitride-based μLEDs can reduce the radiative recombination rate, results in lower modulation bandwidth. Secondly, the carrier localization effect increases the carrier lifetime and thus reduces the bandwidth. At last, the dry-etching induced sidewall damages of μLEDs also limited the modulation bandwidth.

The most common fabrication method of III-nitride-based μLEDs combines a standard photolithography technique and subsequent dry-etching processes on an as-grown III-nitride-based LED wafer.[7–12] Inevitably, sidewall surface damage is incurred during the dry-etching processes, leading to enhanced non-radiative recombination and reduced optical efficiency.[13–18] This issue is not salient in conventional LED with a dimension of >100 μm due to the small ratio of the damaged area to the active area. However, with the reduction of μLED dimension, the damaged area ratio is significantly increased. Therefore, the sidewall damage issue becomes more severe and ultimately becomes a major factor that results in severe degradation of optical performance.[14,15,19] Sidewall passivation is an effective technique used to reduce the sidewall damage effect and improve the optical performance of μLEDs. The standard method is to use PECVD to deposit dielectric materials for surface passivation. There is also a new technique, advanced atomic layer deposition (ALD), that can generate better surface passivation. Although dielectric materials can reduce the effect of plasma damage to μLEDs in the process of dry-etching, the improvement remains limited, even when using the advanced ALD technique. Moreover, the passivation process creates an additional issue: during the etching of dielectric materials to reach p-contact, the p-contact or top of the p-GaN is degraded, leading to reduced electrical injection.[13]

As a result, there have been almost no reports on μLEDs with a dimension less than 5 μm before 2021, which are key components of AR/VR devices. At the same time, the EQE of μLEDs with a dimension of <5 μm is limited to 1% to 5%, which means that such μLEDs cannot provide better efficiency than OLEDs. There is a report of square blue μLEDs with a size of <5 μm which clearly shows severe damage on the sidewalls of the μLEDs on SEM images.[20] As a result, it is quite clear that the traditional fabrication method, which combines standard photolithography technique and subsequent dry-etching processes, may not be suitable for the fabrication of high-performance ultrasmall μLEDs (dimension <5 μm).

In light of these findings, the manufacturing of μLEDs should abandon the traditional fabrication method and undergo a basic change of epitaxial growth and device fabrication, aiming to overcome the huge challenge of efficiency limitation. This chapter introduces a new approach for producing μLEDs that uses confined selective epitaxy on GaN templates patterned with SiO_2 – an approach that is radically different from all traditional fabrication methods. The selective overgrowth occurs only within the pre-patterned SiO_2 microholes. The optimisation of selective area filling factor, template etching depth and μLED structure eventually achieves the ultrasmall, high-efficient and ultracompact green μLED array wafer with a dimension of 3.6 μm and an interpitch of 2 μm. It is worth mentioning that our confined selective epitaxy method entirely avoids the dry-etching processes for the formation of μLED arrays, which are essential to the traditional μLED fabrication method. In addition, the device fabrication processes are simplified because the SiO_2 microhole mask also functions as a kind of natural surface passivation that does not involve any additional process. By these means, ultrasmall green μLEDs with an emission wavelength of 515 nm, high peak EQE of 6%, and high brightness of $>10^7$ cd/m^2 have been achieved.

The schematics of our invention (confined selective epitaxy on patterned template) are illustrated in Figure 4.1, including the growth of as-grown n-GaN template, deposition of SiO_2 on an n-GaN template, patterning process, and confined selective epitaxy of μLEDs.

A 2-μm-thick standard silicon-doped n-GaN buffer layer was initially grown on a 2-inch *c*-plane sapphire substrate by a conventional two-step GaN growth method using an MOCVD technique to prepare an ‘as-grown n-GaN template’. Then, through a standard PECVD technique, 500-nm-thick SiO_2 dielectric film is deposited on the n-GaN template. Subsequently, a photolithography technique and a standard inductively coupled plasma (ICP) technique are combined to selectively etch the SiO_2 dielectric film down to the top surface of the n-GaN layer. The ICP etching processes were carried out under 25 mTorr pressure in a mixture of 20 sccm CHF_3 and 30 sccm Ar with an etching power of 200W. After these processes, a μLED template for confined selective epitaxy is fabricated. Eventually, following the cleaning processes described in Chapter 3, a μLED template is ready for the overgrowth.

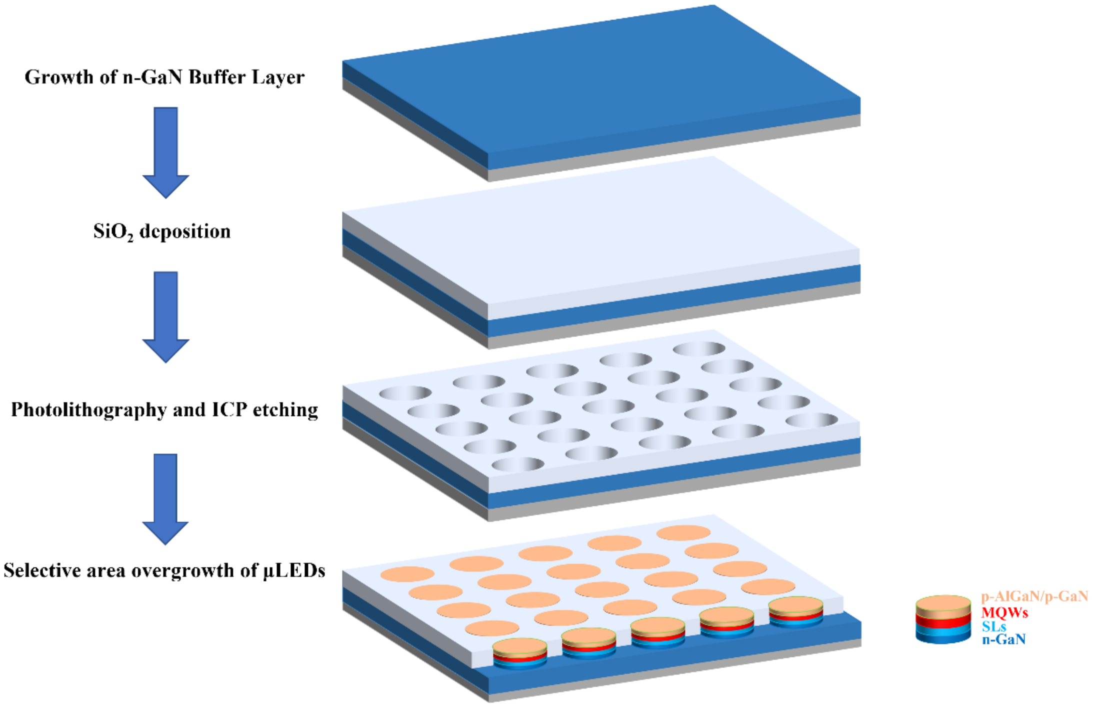

Figure 4.1. *Illustration of patterned template fabrication and* confined selective epitaxy *of μLEDs.*

4.2 Experiment and Discussion

To achieve high-quality ultrasmall InGaN-based µLEDs by an overgrowth on patterned GaN templates, it is essential to conduct a large amount of research work on optimization of the template fabrication and the µLED overgrowth in terms of filling factor, edge effect, initial overgrowth and surface roughness.

4.2.1 Investigation of Filling Factor

Table 4.1. *The growth rates of GaN overgrown on µLED templates with different filling factors.*

Filling factor	**Dektak depth before overgrowth (nm)**	**Dektak depth after overgrowth (nm)**	**Growth thickness (nm)**	**Growth rate (nm/s)**
19.6%	1657	217	1440	3.20
34.9%	1675	852	823	1.83
44.2%	1628	951	677	1.50

The filling factor is defined as the ratio of all µLED areas to a whole wafer area, which is an essential element for confined selective epitaxy by MOCVD.[21–23] The patterned templates used for the subsequent growth of µLEDs used at the beginning of my research were fabricated in 1.65-µm-deep microholes with a diameter of 20 µm, 40 µm and 60 µm, respectively, meaning that ~1.15 µm n-GaN had to be etched apart from the 500 nm SiO_2 on top. To investigate the influence of filling factor on the n-GaN growth rate, 450 sec GaN was grown under the same growth conditions on 20 µm, 40 µm and 60 µm µLED templates with filling factors of 19.6%, 34.9% and 44.2%, respectively. The growth thicknesses of each sample were measured by Dektak and are illustrated in Table 4.1. The estimated growth rates increased sharply from 1.50 nm/s to 3.20 nm/s, with the filling factor decreasing from 44.2% to 19.6%.

4.2.2 Investigation of Edge Effect

Another phenomenon is that the edge of a single μLED pixel is much higher than the centre area after the confined selective epitaxy. This phenomenon is caused by the so-called ‘edge effect’.[24,25]

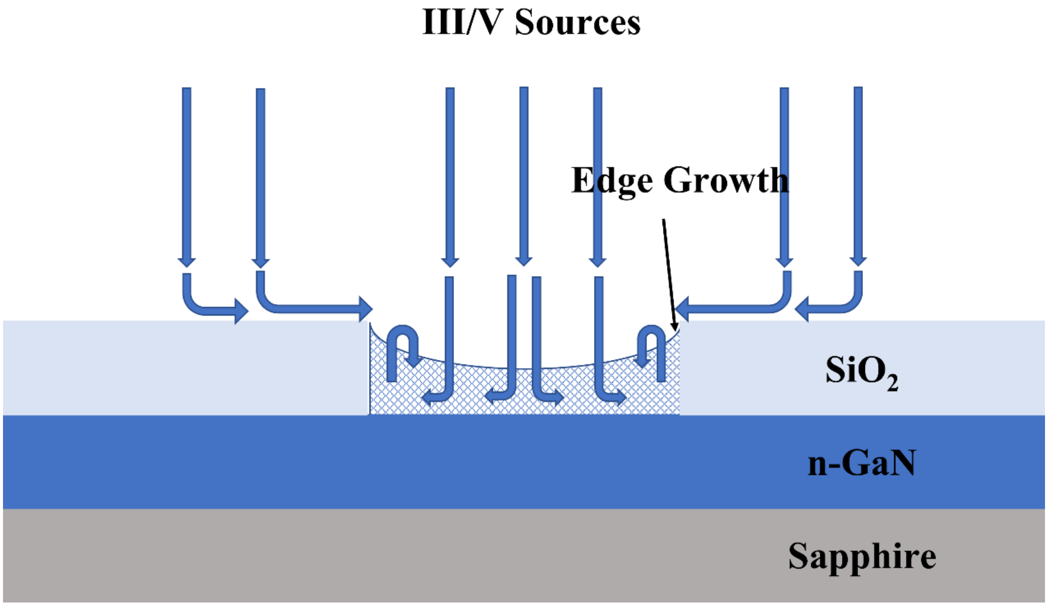

Figure 4.2. *Illustration of* confined selective epitaxy.

Figure 4.2 illustrates growth activity during the MOCVD confined selective epitaxy. Vapour-phase diffusion and surface diffusion are the two main diffusion types involved in selective area growth.[25] The diffusion length of group III sources on SiO_2 is much longer than on GaN, leading to vapour-phase diffusion. The surface diffusion occurs only near the edge of microholes. The absorbed metal–organic (MO) sources on SiO_2 can move into the edge of microholes, resulting in edge growth. Consequently, the MO sources and NH_3 become trapped in microholes and the edge area has more sources, causing more materials to grow in the edge area; this is called the ‘edge effect’.

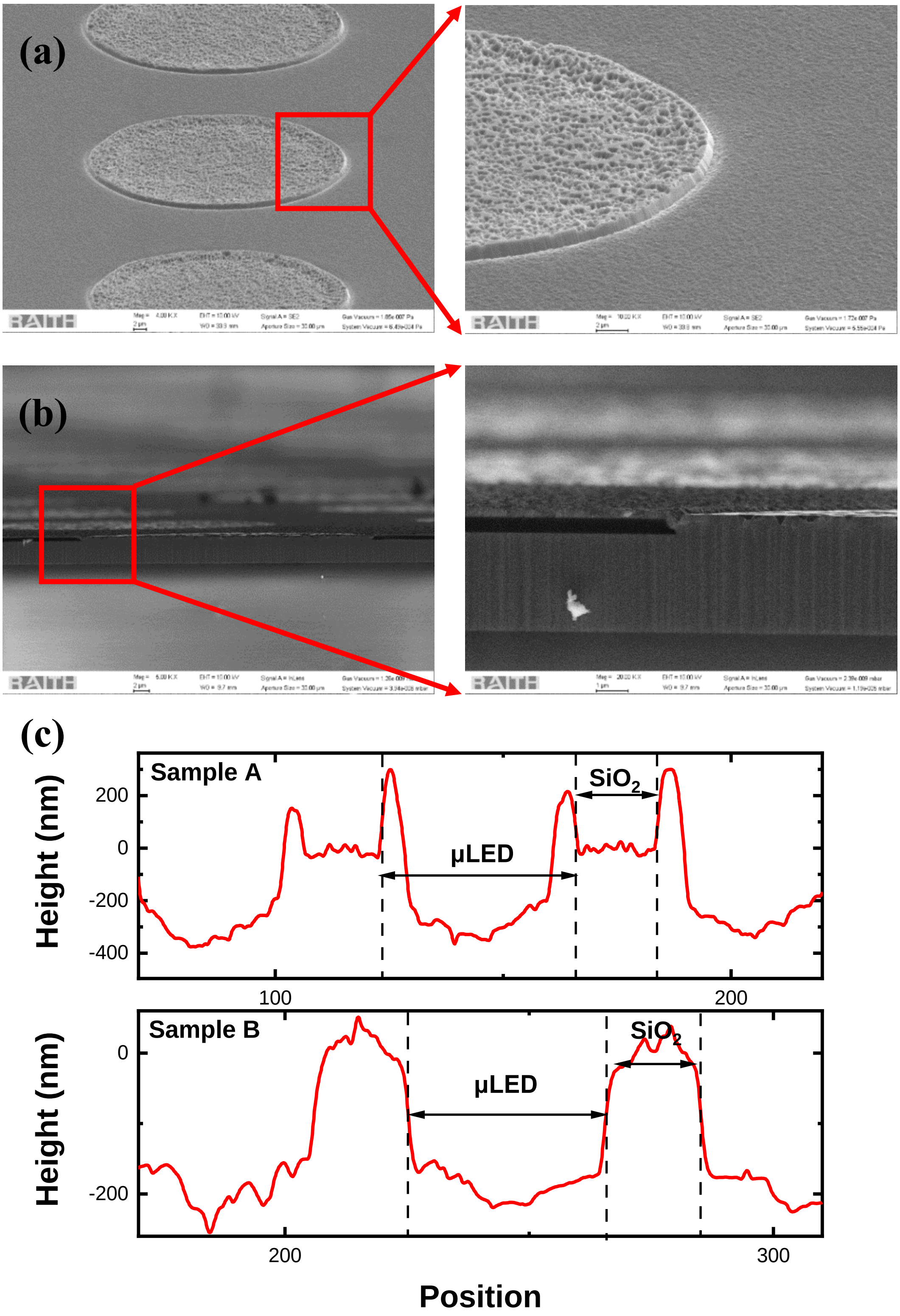

Figure 4.3. *(a) SEM images of sample A, (b) SEM images of sample B, and (c) Dektak measurements of samples A and B.*

The n-GaN overgrowth thickness was reduced to decrease the edge effect. Samples A and B are two 40 μm μLED samples overgrown on 1.65 μm- and 530 μm-deep microhole templates, respectively. In detail, except for the 500 nm SiO_2, 1.15 μm n-GaN was etched for sample A and only 30 nm n-GaN was etched for sample B. The growth conditions are the same except for the n-GaN growth time. As shown in Figure 4.3a, the SEM top view image of sample A with a titled angle of 70 degrees shows that the edge of the μLED pixel is much higher than the centre, whereas sample B in Figure 4.3b shows a flat surface. This issue is also confirmed by the Dektak measurements, as shown in Figure 4.3c. Therefore, the edge effect can be alleviated by reducing the n-GaN growth thickness.

4.2.3 Investigation of Initial n-GaN Growth

Afterward, the μLED diameter was further shrunk to 3.6 μm with an interpitch of 2 μm and a filling factor of 32.5%. Simultaneously, the initial n-GaN growth for the μLED overgrowth was totally removed to make a comparison. Samples C and D wereboth 3.6 μm μLEDs overgrown on 530 nm etching depth templates, and the growth conditions of superlattices (SLs), MQWs, and p-GaN are identical. Sample C did not have n-GaN overgrowth, whereas sample D had 30s n-GaN growth estimated at 60 nm. The n-GaN was overgrown at 1108 °C under 140 torr. The flow rate of NH_3 is 3000 sccm, the flow rate of TMGa is 55 sccm, and the flow rate of Si_2H_6 is 15 sccm. The photoluminescence (PL) results clearly indicated that sample D had a strong deep green emission at 540 nm as indicated in Figure 4.4. However, sample C had no light emission from the MQWs. This is attributed to the enhanced crystal defect density when the μLEDs are grown directly on the template. Therefore, the initial n-GaN growth is essential to achieve the confined selective epitaxy of μLEDs.

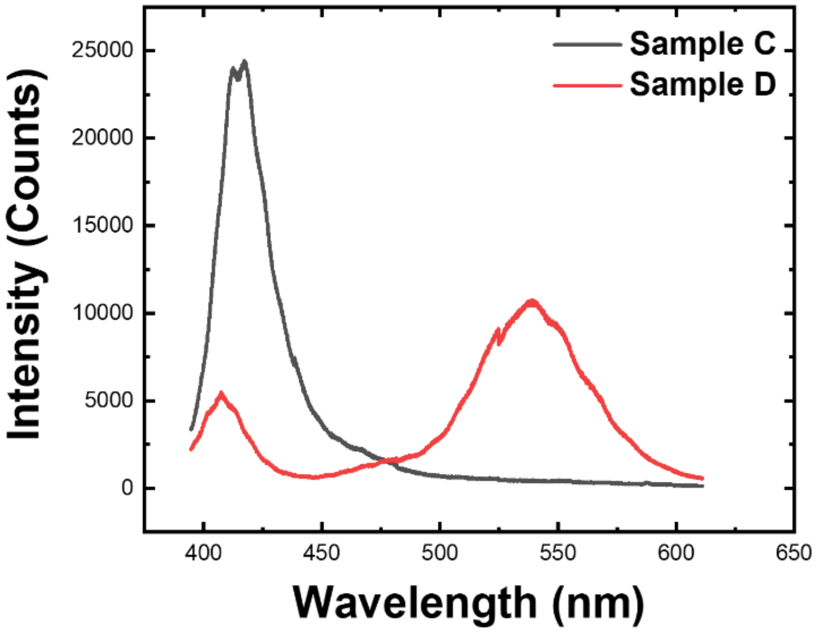

Figure 4.4. *PL spectra of sample C and sample D.*

4.2.4 Characterisation of Surface

To improve the smoothness of the p-GaN surface, three 5 μm μLEDs are prepared – labelled as samples E1, E2 and E3 – which are grown under identical growth conditions for n-GaN, SLs and MQWs. According to the report by W. Lee, at constant growth temperature, the surface roughness of Mg-doped p-GaN increases with the growth rate.[6] In my research, the flow rate of TMGa is reduced to decrease the growth rate. The TMGa flow rate of sample E1 is 20 sccm; for E2, 10 sccm; and for E3, 7.5 sccm. Growth time is increased correspondingly to ensure the same p-GaN growth thickness. The SEM images of p-GaN surfaces are shown in Figure 4.5. It is clear that a lower growth rate results in a smooth p-GaN surface. However, as indicated in Figure 4.6, the PL intensity is also reduced, which is attributed to the thermal degradation of MQWs during the prolonged p-GaN growth time.[27] Consequently, through this method, the smooth p-GaN surface of μLEDs has been achieved.

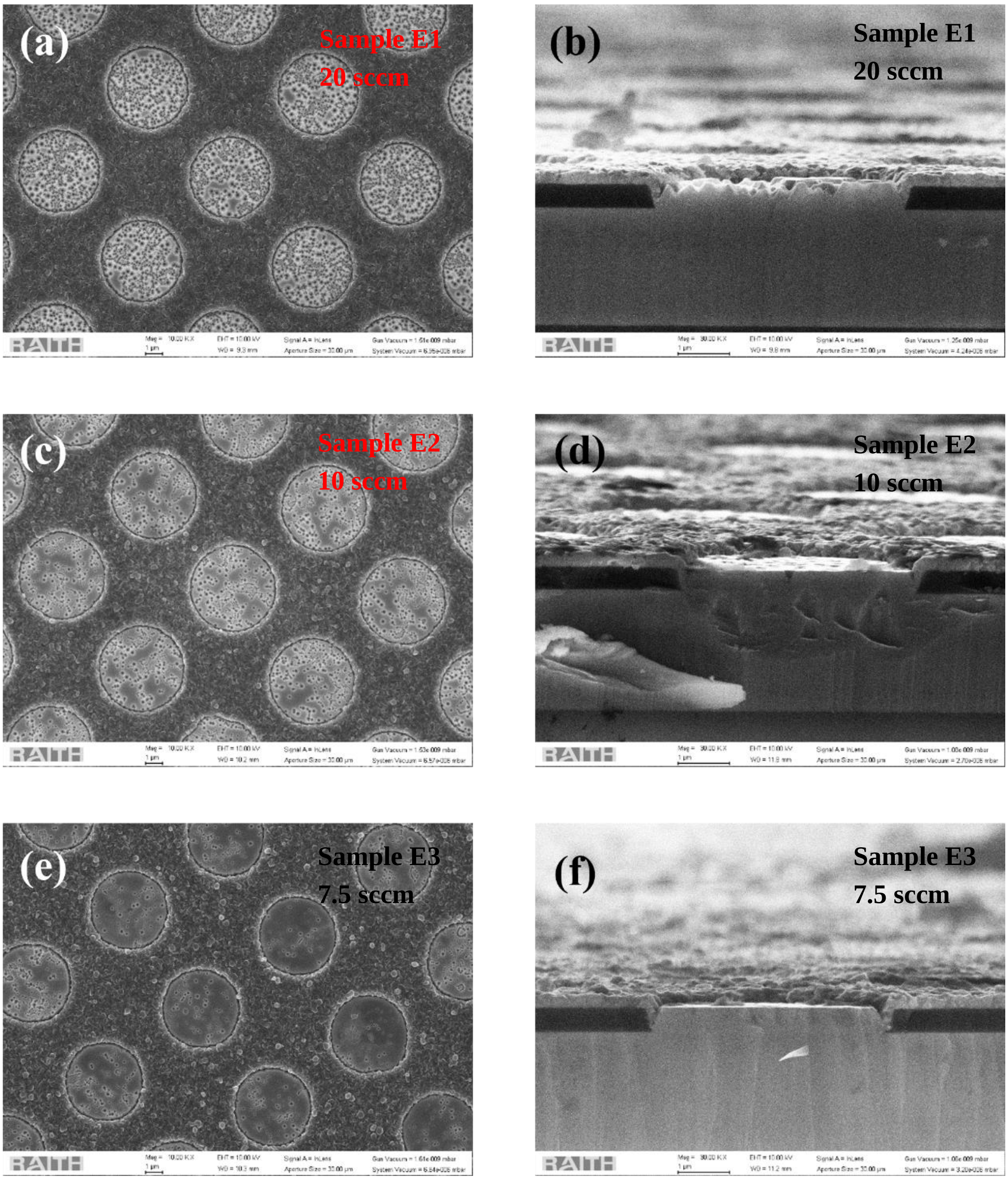

Figure 4.5. *(a) Top view and (b) cross-section SEM image of sample E1; (c) Top view and (d) cross-section SEM image of sample E2; (e) Top view and (f) cross-section SEM image of sample E3.*

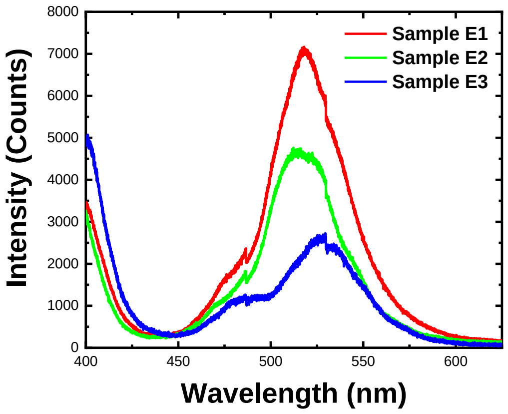

Figure.4.6. *PL spectra of samples E1, E2 and E3.*

4.2.5 Investigation of Superlattice

Three 3.6 μm μLEDs with different superlattice (SLs)_structures were prepared to investigate the influence of SLs. The SLs contain 30 periods InGaN/GaN layers with growth time of 10s/10s, 10s/15s, and 15s/10s respectively. The PL results shown in Figure 4.7 indicate that the thicker InGaN or GaN can both enhace the emission wavelength and the InGaN layer is more effective. However, the FWHM is also increased from 29.3 nm to 35.2 nm and 44.2 nm with the increase of barrier thickness. To achieve a relative longer emission wavelength and narrower FWHM, 30 periods 10s/15s InGaN/GaN SLs are generally used in the μLEDs overgrowth.

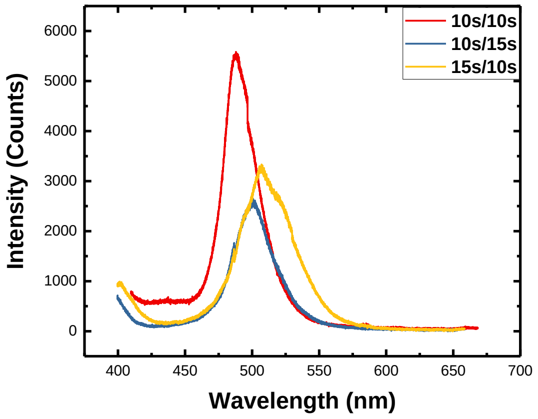

Figure 4.6. *The PL spectra of μLEDs with different SLs.*

4.2.6 Investigation of Active Region

The effect of quantum barriers (QBs) thickness is investigated by the comparison of samples F1, F2 and F3 which only have different QB thicknesses of 16 nm, 15 nm and 13.3nm respectively. As shown in the Figure 4.7a, sample F1 has a PL wavelength of 533 nm, sample F2 is 528 nm and sample F3 is 504 nm. Hence, with the increase of barrier thickness, there is a red-shift. This may be caused by the enhanced QCSE due to the thicker GaN barrier thickness. The number of quantum wells (QWs) is also investigated. The PL results are shown in Figure 4.7b. With the increase of MQWs period, the PL intensity increased as well. However, only the last one or two QWs are working under EL due to the low carrier mobility of holes. Hence, seven QWs are not necessary. Meanwhile, the PL intensity of three QWs sample is too low to get enough information to analyse. Therefore, I use five QWs active region in this project.

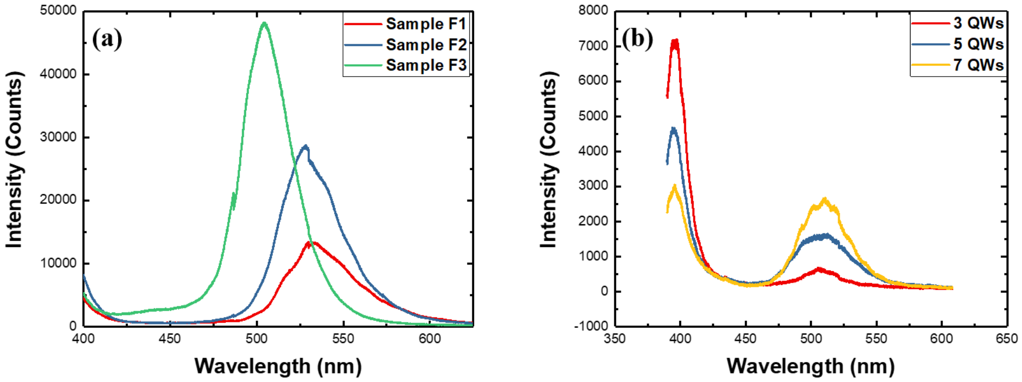

Figure 4.7. *(a) The PL spectra of LED with different barrier thicknesses and (b) the PL spectra of μLED with different number of MQWs.*

4.2.7 Effect of Micro-LED Dimensions

One important phenomenon I found during this project is the size-dependent wavelength shift of μLEDs achieved by CSE. Figure 4.8a illustrates the 2 inch μLED template with three different dimensions (20 μm, 40 μm and 60 μm). Through this design, the 20 μm, 40 μm and 60 μm μLEDs can be grown under the identical growth condition at the same growth run. The PL wavelength of 20 μm, 40 μm and 60 μm µLEDs is 518 nm, 502 nm and 490 nm, respectively (Figure 4.8b). This phenomenon may be caused by the strain relaxation in the CSE, leading to high indium composition.

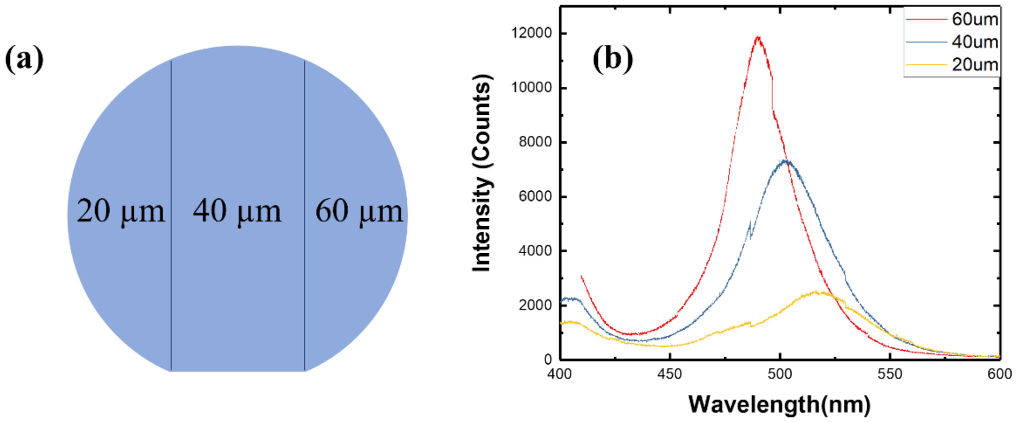

Figure 4.7. *(a) The demonstration of µLED template with different µLED sizes and (b) the PL spectra of sample GN4108.*

4.2.8 Achieving Ultrasmall Green µLEDs with a Diameter of 3.6 µm

As a product of all the optimisation described above, 3.6 µm ultrasmall green µLEDs with an interpitch of 2 µm have been achieved. The optimized III-nitride LED structure was grown on the n-GaN template patterned with microhole arrays by MOCVD. Initially, a thin silicon-doped n-GaN layer, estimated at 50 nm, was grown in H_2 ambient under 140 torr reactor pressure at 1108 °C. The flow rates of TMGa, Si_2H_4 and NH_3 are 55 sccm, 15 sccm and 3000 sccm, respectively. Next, the reactor ambient is changed to N_2, the temperature is reduced to 890 °C, and the reactor pressure is increased to 250 torr to prepare the growth of a 200 nm $In_{0.05}Ga_{0.95}N$-based pre-layer. In detail, the InGaN pre-layer consists of 30 pairs of $In_{0.05}Ga_{0.95}N$/GaN SLS with 4.2 nm InGaN layers and 2.5 nm GaN layers. Subsequently, the active region, which is formed by five periods of 2.5 nm/13.5 nm $In_{0.2}Ga_{0.8}N$/GaN MQWs, was grown under 250 torr as well.

The quantum wells were grown at 795 °C with a flow rate of 1.5 sccm TMGa, 200 sccm TMIn and 8000 sccm NH_3, while the growth temperature of quantum barriers was 880 °C in a mixture ambient of 6 sccm TMGa and 8000 sccm NH_3. The SLS and MQW structures were examined by the XRD measurement processed by the Bruker D8 X-ray diffraction system and the Bruker LV-RADS simulation software. Figure 4.9a shows the XRD omega-2theta measurement and fitting results of the μLED sample. Finally, a 20 nm p-AlGaN electron-blocking layer (EBL) and a 200 nm p-GaN layer were grown.

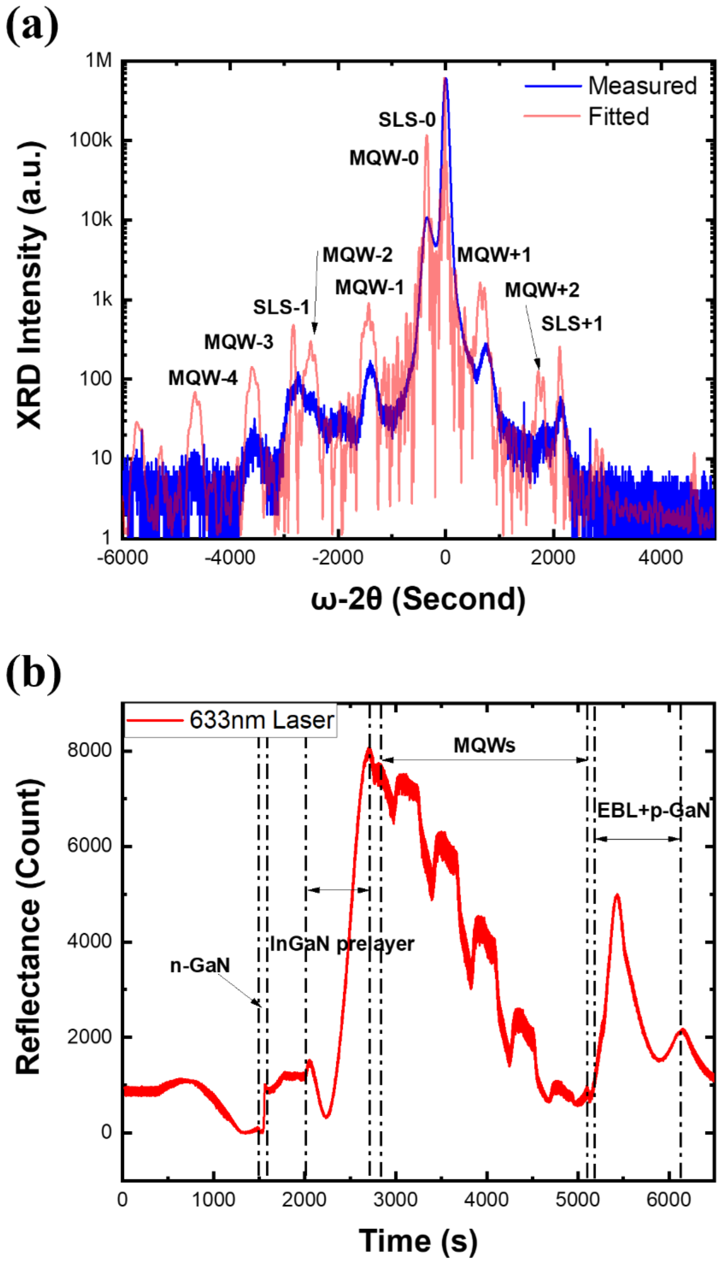

Figure 4.9. *(a) High-resolution XRD omega-2theta measurement and fitting results; (b) μLED overgrowth reflectance.*

Figure 4.9b shows the reflectance of the whole overgrowth process, whichshows n-GaN, InGaN SLS pre-layer, MQW, EBL and p-GaN growth. The total overgrowth thickness is close to that of SiO_2 dielectric film (i.e. approximately 500 nm). Due to the existence of SiO_2 masks, the LED structure can be grown only in the microholes to directly form µLED arrays (Figure 4.2c). Through this approach, the SiO_2 microhole masks, without involving any µLED mesa etching processes, can entirely control the diameter, the individual location, the shape, and the interpitch of µLED arrays.

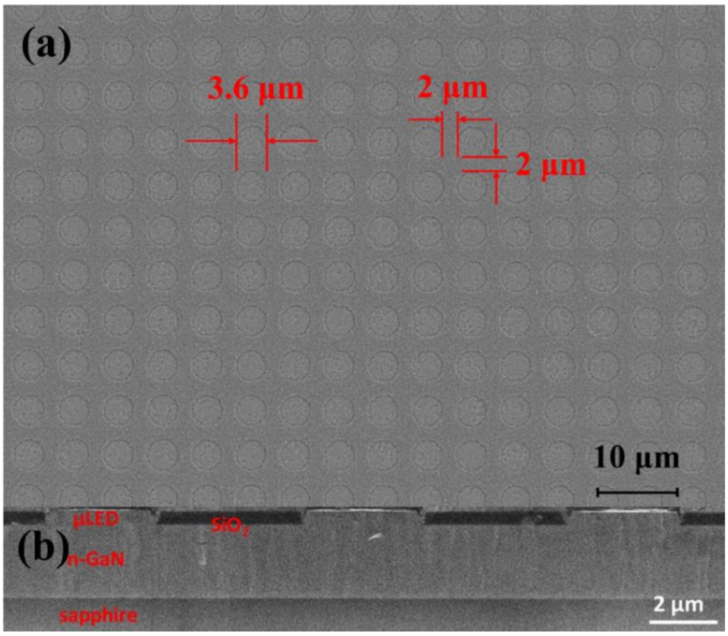

Figure 4.10. *(a) Top view and (b) cross-section SEM image of 3.6 µm µLEDs.*

The SEM images in Figures 4.10a and 4.10b show, respectively, the typical top view and cross-sectional view of our regularly arrayed µLED wafer. It is apparent that our µLED arrays have a circular shape as well as excellent uniformity of diameter (3.6 µm) and interpitch (2 µm). Aiming to achieve high-resolution microdisplay (like VR/AR) in a compact manner, µLED dimension and interpitch as small as those of our regularly arrayed µLEDs are essential. Moreover, a very high filling factor (~32.5%) of our µLED wafer is illustrated in Figure 4.10a. It is clear that in Figure 4.10b, the µLEDs are embedded in the patterned microholes, and that the top faces of µLEDs – which have almost the same height as the top of SiO_2 film – are very flat.

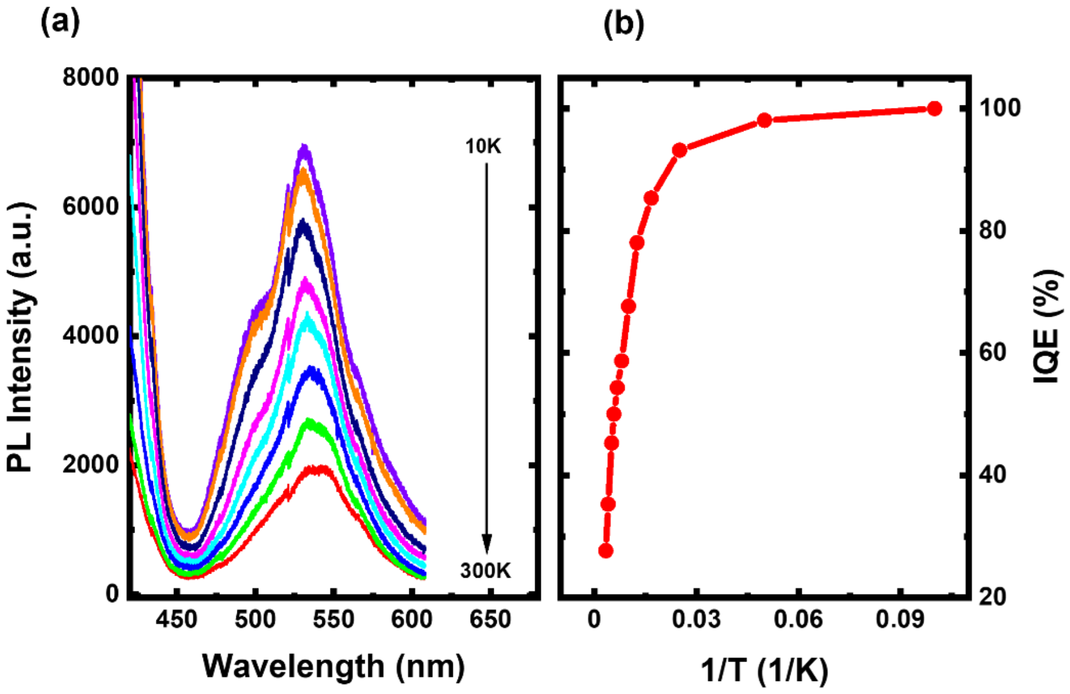

Figure 4.11. *(a) TDPL spectrum and (b) IQE as a function of temperature.*

The IQE of this μLED sample was assessed by temperature-dependent photoluminescence (TDPL) measurements, which used a 375 nm diode laser as an excitation source. A monochromator (Horiba SPEX 500M) was used to disperse the emission light from the μLED sample, and an air-cooled CCD was involved in detecting the emission. A closed-cycle helium cryostat was used to place the sample and control the temperature from 10K to 300K. The TDPL spectra measured from 10K to 300K under an excitation power density of 3 W/cm^2 indicate strong green emission at around 520 nm, as shown in Figure 4.11a. Moreover, as indicated in Figure 4.11b, the efficiency as a function of temperature is calculated by the ratio of integrated PL intensity at high temperatures to that at 10K. The integrated region is from 460 nm t 610 nm. The measured IQE value at room temperature is around 28%.

4.2.9 Device Characterisation

This sample was subsequently fabricated into an LED device with an area of 0.1 mm^2, including thousands of 3.6 μm μLEDs (Figure 4.12a). A layer of ITO was deposited on the top of the sample and annealed under an air atmosphere at 600 °C for 1 minute to form transparent p-type contact. Ti/Au alloys were deposited as an anode and cathode by a thermal evaporator. The characteristics of these green μLED arrays were measured on a bare chip with no coating, passivation, epoxy or reflector, which are commonly used to enhance extraction efficiency.

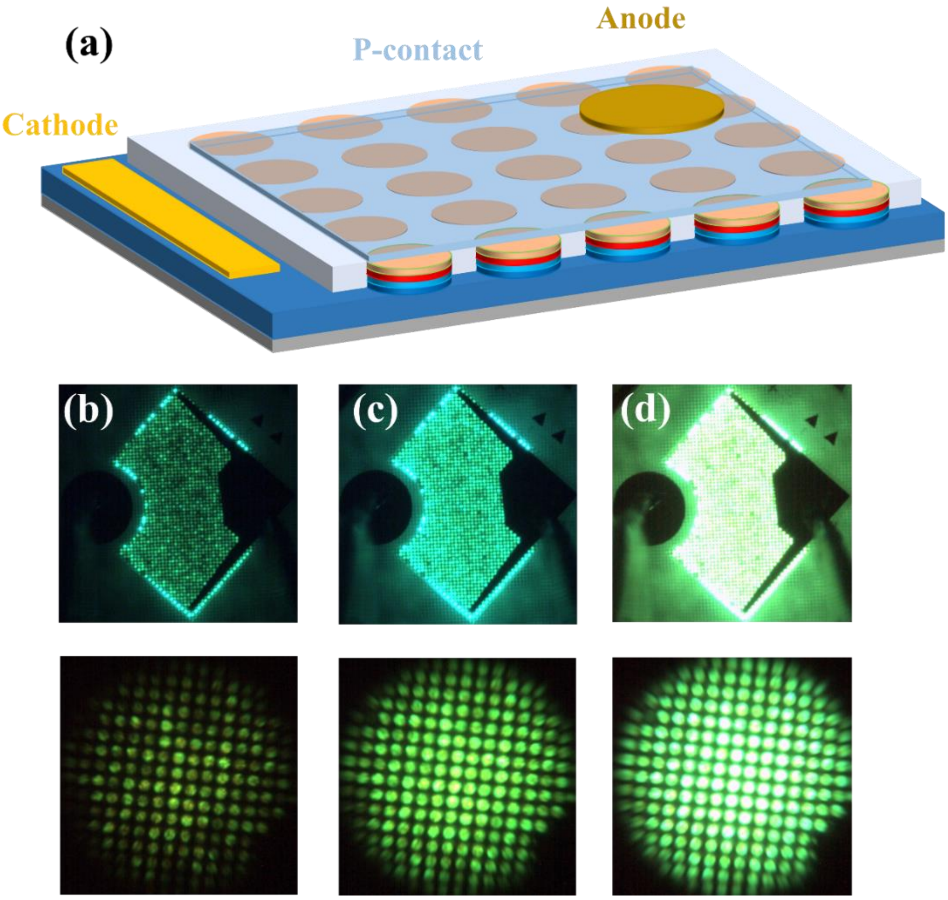

Figure 4.12. *(a) Schematic illustration of our green μLED array. (b) EL microscopy images of our μLED arrays at an injection current density of 1 A/cm^2 (upper: under low magnification; bottom: under high magnification. (c) EL microscopy images of our μLED arrays at an injection current density of 3 A/cm^2. (d) EL microscopy images of our μLED arrays at an injection current density of 9 A/cm^2.*

For the device chip in this case, each μLED pixel shares a common n-contact, and all the p-contacts remain open. In the future, these can be bonded for indium bumps with drive transistors on a CMOS to achieve controlled microdisplay.[1] Thus, the μLEDs achieved by our new direct epitaxy approach can be applied to any existing microdisplay fabrication techniques. For example, the most common pick-and-place technology as well as semiconductor integration of μLEDs and transistors are both compatible with our μLEDs.[1]

Aiming to clearly demonstrate the emission of μLED arrays, microscope images are taken by a micro-electroluminescence (micro-EL) system, which is equipped with two objective lenses: 10× and 50× for total magnification of 120× and 600×, respectively. Figures 4.12b, 4.12c and 4.12d depict the EL microscope images under 120× and 600× magnification of a single μLED array chip at injection current densities of 1 A/cm^2, 3 A/cm^2 and 9 A/cm^2, respectively. It is clear that all 3.6 μm μLED pixels show strong green emission under a low current density of 3 A/cm^2. Considering the area of a single 3.6 μm μLED pixel, each μLED pixel can be turned on at a bias of 2.5 V and an ultralow driving current of 0.3 μA, while the common driving current is 1 − 20 μA.[28,29] It also indicates that the power consumption of a 640 × 480 microdisplay is merely ~0.23W. At an injection current density of 9 A/cm^2, the emission is ultrabright as shoen in Figure 4,12d. However, when the injection current density is reduced to 1 A/cm^2, the emission is non-uniform. This may be attributable to the ITO contact issue and might be resolved by optimising the ITO deposition conditions. Importantly, the injection current density of our μLEDs is much smaller than the typical injection current density of 22 A/cm^2 for a conventional 330 μm × 330 μm broad-area LED. This also means that a microdisplay fabricated by our μLEDs should have at least the same lifetime as that of a microdisplay fabricated by broad-area LEDs, which is expected to work more than 100,000 h under normal operating conditions.[30] However, the lifetime performance of our μLEDs needs more professional tests in the furture.

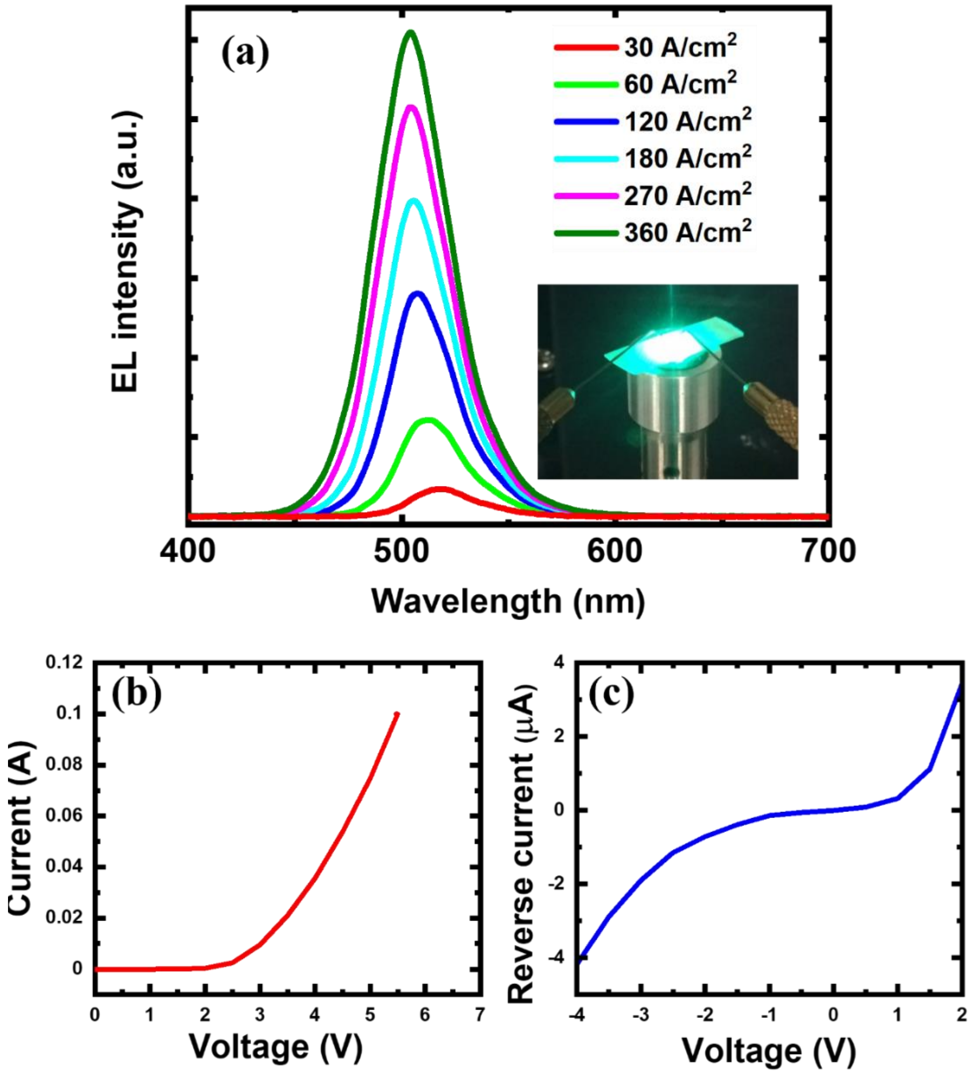

Figure 4.13. *(a) EL spectra of individual μLED array chip measured as a function of injection current density at room temperature. Inset: Emission photo of a μLED array chip taken at 60 A/cm^2. (b) I–V characteristics of individual μLED array chip as a function of forward voltage. (c) I–V characteristics of individual μLED array chip as a function of reverse bias.*

The EL spectra of a single μLED array chip as a function of injection current density at room temperature are demonstrated in Figure 4.13a. The current density range is from 30 to 360 A/cm^2, corresponding to the current from 10 to 120 mA. The EL intensity is enhanced with the increase of injection current density, and all EL spectra show single emission peaks (505–520 nm) in the green emission region. The inset emission photo illustrates a very bright green emission of a single µLED array chip at 60 A/cm^2 current density. As indicated in Figure 4.13b, the current–voltage (I–V) characteristic of our µLEDs show 20 mA injection current at 3.4 V forward bias, which is similar to that of conventional broad-area LEDs. The I–V characteristic under reverse bias, which examines the leakage current, is shown in Figure 4.13c. The leakage current of our µLED array chip is 4.1 µA at 4 V reverse bias, indicating that the leakage current density is only 0.013 A/cm^2, which is much lower than that of 10 µm blue µLEDs fabricated by the traditional µLED fabrication method with advanced ALD passivation technology.[19] In summary, our µLED array chips exhibit very good electrical performance.

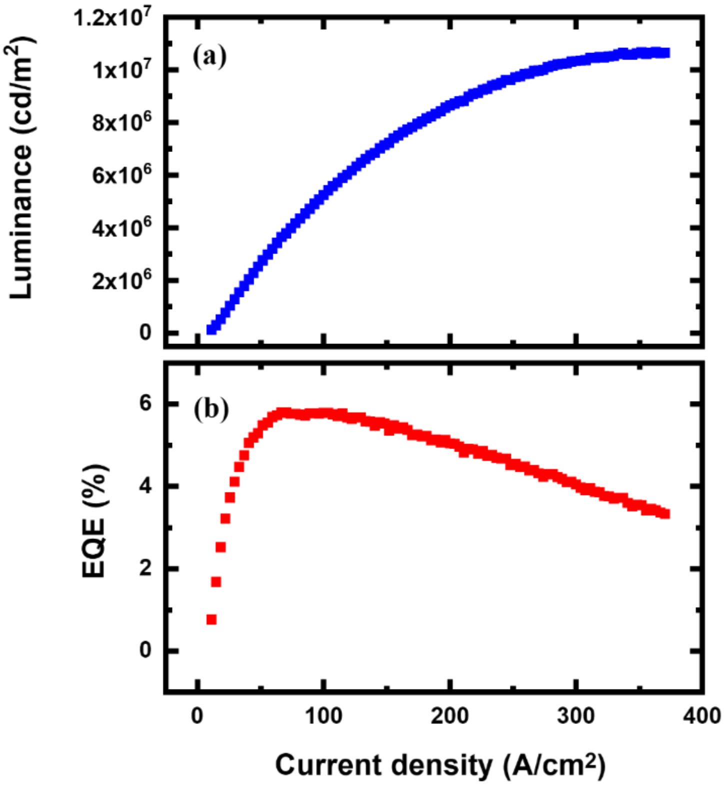

Figure 4.14. *(a) Luminance of µLEDs as a function of injection current density; (b) EQE of µLEDs as a function of injection current density.*

An LCS-100 characterisation system equipped with an integrating sphere and a CCD APRAR spectrometer is used in this project to measure the luminance and EQE of our μLED array chip in a CW mode. As indicated in Figure 4.14a, the high luminance of 1 × 10^7 cd/m^2, which is two to three times higher than that of current OLEDs[31] and LCDs,[32] has been achieved on our μLED array chip. Figure 4.14b shows the EQE of our μLED array chip as a function of injection current density up to 400 A/cm^2. It is immediately apparent that the peak EQE of our μLEDs is around 6%, which is a record-setting EQE compared with that of other green μLEDs previously reported. Our μLEDs can also be operated at a high current density of 400 A/cm^2 without any heat sink, demonstrating very high material quality through the overgrowth. It is worth highlighting that our μLEDs are fabricated without any surface coating, passivation, epoxy or reflectors. Therefore, the EQE can be further enhanced by involving proper packages used to increase the extraction efficiency.

4.3 Summary

In summary, ultrasmall, high-efficient and ultracompact μLEDs with a dimension of 3.6 μm and an interpitch of 2 μm have been achieved by a confined selective epitaxy approach after the optimisation of template fabrication and μLED overgrowth. Through this approach, the sidewall damages introduced during dry-etching processes in the traditional μLED fabrication approaches can be eliminated. Consequently, a high IQE of 28%, a high luminance in excess of 1 × 10^7 cd/m^2, and a high EQE of 6% at 515 nm emission have been obtained.

Reference

1. Lee, V. W.; Twu, N.; Kymissis, I. Micro-LED Technologies and Applications. *Information Display* **2016**, *32* (6), 16–23.

2. Fan, Z. Y.; Lin, J. Y.; Jiang, H. X. III-Nitride Micro-Emitter Arrays: Development and Applications. *Journal of Physics D: Applied Physics* **2008**, *41* (9), 094001.

3. Templier, F. GaN-Based Emissive Microdisplays: A Very Promising Technology for Compact, Ultra-High Brightness Display Systems. *Journal of the Society for Information Display* **2016**, *24* (11), 669–675.

4. Day, J.; Li, J.; Lie, D. Y. C.; Bradford, C.; Lin, J. Y.; Jiang, H. X. III-Nitride Full-Scale High-Resolution Microdisplays. *Applied Physics Letters* **2011**, *99* (3), 031116.

5. Green, R. P.; McKendry, J. J. D.; Massoubre, D.; Gu, E.; Dawson, M. D.; Kelly, A. E. Modulation bandwidth studies of recombination processes in blue and green InGaN quantum well micro-light-emitting diodes. *Applied Physics Letter* **2013**, *102* (9), 091103.

6. Rajbhandari, S.; McKendry, J. J. D.; Herrnsdorf, J.; Chun, H.; Faulkner, G.; Haas, H.; Watson, I. M.; O’Brien, D.; Dawson, M. D. A review of gallium nitride LEDs for multi-gigabit-per-second visible light data communications. *Semiconductor Science and Technology* **2017**, *32* (2), 023001.

7. Ozden, I.; Diagne, M.; Nurmikko, A. V.; Han, J.; Takeuchi, T. A matrix addressable 1024 element blue light emitting InGaN QW diode array. *physica status solidi (a)* **2001**, *188* (1), 139−142.

8. Liu, Z. J.; Wong, K. M.; Keung, C. W.; Tang, C. W.; Lau, K. M. Monolithic LED Microdisplay on Active Matrix Substrate Using Flipchip Technology. *IEEE Journal of Selected Topics in Quantum Electronics* **2009**, *15* (4), 1298−1302.

9. Otto, I.; Mounir, C.; Nirschl, A.; Pfeuffer, A.; Schapers, Th.; Schwarz, U. T.; von Malm, N. Micro-pixel Light Emitting Diodes: Impact of the Chip Process on Microscopic Electro- and Photoluminescence. *Applied Physics Letters* **2015**, *106* (15), 151108.

10. Li, K. H.; Cheung, Y. F.; Tang, C. W.; Zhao, C.; Lau, K. M.; Choi, H. W. Optical Crosstalk Analysis of Micro-Pixelated GaN-Based Light-Emitting Diodes on Sapphire and Si Substrates. *physica status solidi (a)* **2016**, *213* (5), 1193–1198.

11. Templier, F.; Dupré, L.; Tirano, S.; Marra, M.; Verney, V.; Olivier, F.; Aventurier, B.; Sarrasin, D.; Marion, F.; Catelain, T.; Berger, F.; Mathieu, L.; Dupont, B.; Gamarra, P. 75-1: Invited Paper: GaN-Based Emissive Microdisplays: A Very Promising Technology for Compact, Ultra-High Brightness Display Systems. *SID Symposium Digest of Technical Papers* **2016**, *47* (1), 1013–1016.

12. Lobo Ploch, N.; Rodriguez, H.; Stolmacker, C.; Hoppe, M.; Lapeyrade, M.; Stellmach, J.; Mehnke, F.; Wernicke, T.; Knauer, A.; Kueller, V.; Weyers, M.; Einfeldt, S.; Kneissl, M. Effective Thermal Management in Ultraviolet Light-Emitting Diodes with Micro-LED Arrays. *IEEE Transactions on Electron Devices* **2013**, *60* (2), 782–786.

13. Olivier, F.; Daami, A.; Licitra, C.; Templier, F. Shockley-Read-Hall and Auger Non-Radiative Recombination in GaN Based LEDs: A Size Effect Study. *Applied Physics Letters* **2017**, *111* (2), 022104.

14. Wong, M. S.; Hwang, D.; Alhassan, A. I.; Lee, C.; Ley, R.; Nakamura, S.; DenBaars, S. P. High Efficiency of III-Nitride Micro-Light-Emitting Diodes by

Sidewall Passivation Using Atomic Layer Deposition. *Optics Express* **2018**, *26* (16), 21324.

15. Konoplev, S. S.; Bulashevich, K. A.; Karpov, S. Yu. From Large-Size to Micro-LEDs: Scaling Trends Revealed by Modelling. *physica status solidi (a)* **2017**, *215* (10), 1700508.

16. Yang, C.-M.; Kim, D.-S.; Park, Y. S.; Lee, J.-H.; Lee, Y. S.; Lee, J.-H. Enhancement in Light Extraction Efficiency of GaN-Based Light-Emitting Diodes Using Double Dielectric Surface Passivation. *Optics and Photonics Journal* **2012**, *02* (03), 185–192.

17. Yiyun, Z.; Enqing, G.; Zhi, L.; Tongbo, W.; Jing, L.; Xiaoyan, Y.; Guohong, W. Light Extraction Efficiency Improvement by Curved GaN Sidewalls in InGaN-Based Light-Emitting Diodes. *IEEE Photonics Technology Letters* **2012**, *24* (4), 243–245.

18. Zuo, P.; Zhao, B.; Yan, S.; Yue, G.; Yang, H.; Li, Y.; Wu, H.; Jiang, Y.; Jia, H.; Zhou, J.; Chen, H. Improved Optical and Electrical Performances of GaN-Based Light Emitting Diodes with Nano Truncated Cone SiO_2 Passivation Layer. *Optical and Quantum Electronics* **2016**, *48* (5).

19. Hwang, D.; Mughal, A.; Pynn, C. D.; Nakamura, S.; DenBaars, S. P. Sustained High External Quantum Efficiency in Ultrasmall Blue III–Nitride Micro-LEDs. *Applied Physics Express* **2017**, *10* (3), 032101.

20. Templier, F.; Benaïssa, L.; Aventurier, B.; Nardo, C. D.; Charles, M.; Daami, A.; Henry, F.; Dupré, L. 19-6: Invited Paper: A Novel Process for Fabricating High-Resolution and Very Small Pixel-Pitch GaN LED Microdisplays. *SID Symposium Digest of Technical Papers* **2017**, *48* (1), 268–271.

21. Marchand, H.; Ibbetson, J. P.; Fini, P. T.; Keller, S.; DenBaars, S. P.; Speck, J. S.; Mishra, U. K. Mechanisms of Lateral Epitaxial Overgrowth of Gallium Nitride by Metalorganic Chemical Vapor Deposition. *Journal of Crystal Growth* **1998**, *195* (1-4), 328–332.

22. Kayser, O.; Westphalen, R.; Opitz, B.; Balk, P. Control of Selective Area Growth of InP. *Journal of Crystal Growth* **1991**, *112* (1), 111–122.

23. Coltrin, M. E.; Mitchell, C. C. Mass Transport and Kinetic Limitations in MOCVD Selective-Area Growth. *Journal of Crystal Growth* **2003**, *254* (1-2), 35–45.

24. Tanaka, A.; Chen, R.; Jungjohann, K. L.; Dayeh, S. A. Strong Geometrical Effects in Submillimeter Selective Area Growth and Light Extraction of GaN Light Emitting Diodes on Sapphire. *Scientific Reports* **2015**, *5* (1).

25. Sugiyama, M. Selective Area Growth of III-V Semiconductors: From Fundamental Aspects to Device Structures. *2010 22nd International Conference on Indium Phosphide and Related Materials (IPRM)* **2010**.

26. Lee, W.; Limb, J.; Ryou, J.-H.; Yoo, D.; Chung, T.; Dupuis, R. D. Influence of Growth Temperature and Growth Rate of P-GaN Layers on the Characteristics of Green Light Emitting Diodes. *Journal of Electronic Materials* **2006**, *35* (4), 587–591.

27. Oh, M.-S.; Kwon, M.-K.; Park, I.-K.; Baek, S.-H.; Park, S.-J.; Lee, S. H.; Jung, J. J. Improvement of Green LED by Growing P-GaN on $In_{0.25}GaN/GaN$ MQWs at Low Temperature. *Journal of Crystal Growth* **2006**, *289* (1), 107–112.

28. Day, J.; Li, J.; Lie, D. Y. C.; Bradford, C.; Lin, J. Y.; Jiang, H. X. Full-Scale Self-Emissive Blue and Green Microdisplays Based on GaN Micro-LED Arrays. *Quantum Sensing and Nanophotonic Devices IX* **2012**.

29. Zhang, L.; Ou, F.; Chong, W. C.; Chen, Y.; Li, Q. Wafer-Scale Monolithic Hybrid Integration of Si-Based IC and III-V Epi-Layers-A Mass Manufacturable Approach for Active Matrix Micro-LED Micro-Displays. *Journal of the Society for Information Display* **2018**, *26* (3), 137–145.

30. Meneghini, M.; Tazzoli, A.; Mura, G.; Meneghesso, G.; Zanoni, E. A Review on the Physical Mechanisms That Limit the Reliability of GaN-Based LEDs. *IEEE Transactions on Electron Devices* **2010**, *57* (1), 108–118.

31. Liu, S.; Zang, C.; Zhang, X.; Shen, D.; Yu, H.; Li, M.; Wang, H.; Tong, Z.; Lo, M.-F.; Zhang, L.; Xie, W.; Lee, C.-S. Centimeter-Scale Hole Diffusion and Its Application in Organic Light-Emitting Diodes for Reducing Efficiency Roll-off and Enhancing Operation Lifetime. **2021**.

32. Liu, C.; Jiang, Z.; Xu, H.; Son, W.; Wang, X. P-16: Turnaround Phenomenon of Threshold Voltage Shifts in Bias-Stressed A-Si:H Thin-Film Transistor under Extremely High Intensity Illumination. *SID Symposium Digest of Technical Papers* **2021**, *52* (1), 1112–1115.

Chapter 5

Direct Epitaxial Growth to Integrate μLEDs with Nanoporous DBRs

High-efficiency micro light-emitting diodes (μLEDs) with an ultrasmall dimension (i.e. less than 5 μm) and narrow spectral line width are required for microdisplays such as augmented reality (AR) and virtual reality (VR). However, the traditional μLED fabrication technology introduces unavoidable sidewall damages to μLED pixels during the dry-etching processes, thereby limiting the external quantum efficiency (EQE) of ultrasmall μLEDs. Moreover, the spectral line width of μLEDs that use InGaN as emitting layer tends to be broad. With the increase of emission wavelength, which is determined by the indium content in the emitting region, the spectral line width is further increased. In this chapter, a combination of epitaxial lattice-matched DBRs and confined selective epitaxy of μLEDs are developed to address all these challenges. As a result, a high peak EQE of 9% at around 500 nm emission has been achieved by our μLEDs with a dimension of 3.6 um and an interpatch of 2 μm. Most importantly, μLEDs produced by our method exhibit a spectral line width of 25 nm, which is the narrowest value of green μLEDs yet reported.

5.1 Introduction

A narrow spectral line width of μLEDs is necessary to achieve high-resolution microdisplays, and it is well known that III-nitride-based μLEDs using InGaN MQWs as emitting regions have broad spectral line width. This phenomenon is caused by indium segregation and alloy fluctuation.[1–3] To achieve a long emission wavelength like that of the green emission, a high indium composition is required. In this case, the indium segregation and alloy fluctuation become more severe, leading to the broader spectral line width.

As illustrated in Chapter 4, 3.6 μm μLEDs with an interpitch of 2 μm were achieved by the confined selective epitaxy approach, exhibiting a peak EQE of 6% at 515 nm.[4] In this approach, μLEDs are directly overgrown on a pre-patterned template. It is worth highlighting that the dry-etching processes are eliminated from this approach – which means that the sidewall damages incurred during the dry-etching processes are also eliminated. However, further improvements in EQE and spectral line width are still required for microdisplay applications.

One effective method for achieving those requirements is to involve a reflector below the active region (MQWs). Specifically, integration of μLEDs and high-reflectivity distributed Bragg reflectors (DBRs) achieved by MOCVD epitaxy would be ideal. This would not only enhance extraction efficiency but may also potentially reduce the line width of the emission spectra of μLEDs.

Many researchers have studied lattice-mismatched AlGaN/GaN or AlN/ GaN DBRs.[5–8] However, many severe problems persist, such as cracking and rough surfaces caused by strain accumulation.[9] Furthermore, to achieve high reflectivity, the number of DBR pairs must be increased because the refractive index difference between AlN and GaN is relatively small.[9,10] As a result, growth time is significantly increased, leading to high costs.

For lattice-matched DBRs, where the refractive index difference between two alternating layers in each pair is very high, a small number of DBR pairs can also meet the requirement of high reflectivity. Recently, nanoporous (NP) GaN achieved by electro-chemical (EC) etching has been widely employed for the fabrication of lattice-matched DBRs.[11–13] It has been shown that a small number of the NP-GaN/GaN DBR pairs can achieve high reflectivity, resulting in reduced epitaxial growth time and lower costs. Furthermore, the high crystal quality of GaN is also preserved through this approach, thus benefiting the subsequent growth of optoelectronic devices.

This chapter has demonstrated μLEDs achieved by a confined selective epitaxy approach integrated with lattice-matched DBRs. By this method, the EQE of μLEDs is significantly increased, and the spectral line width of μLEDs is reduced; both of these advances are ideal for microdisplay applications.

5.2 Experiment and Discussion

5.2.1 Growth of Lattice-Matched Nanoporous DBRs

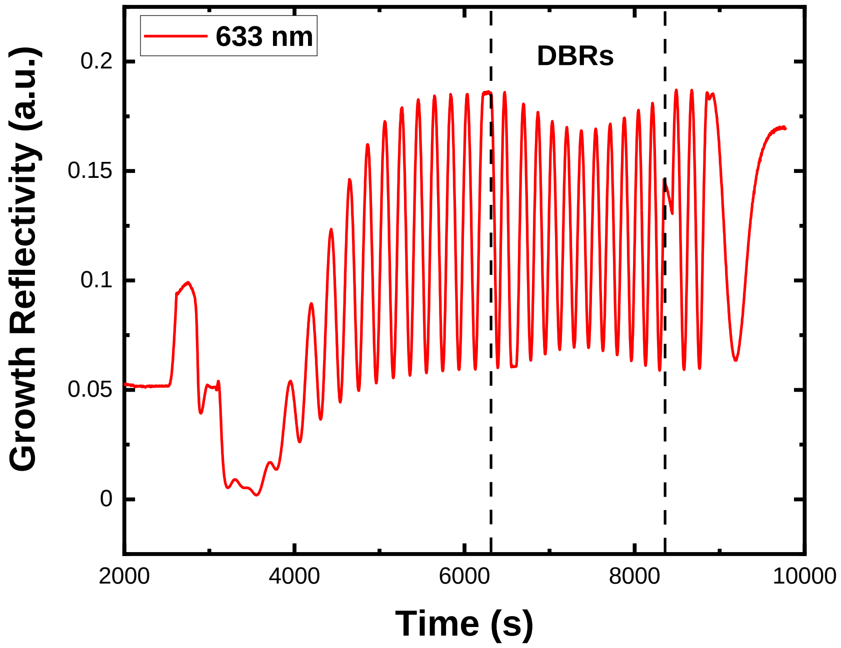

Figure 5.1. *Growth reflectivity of as-grown DBR template.*

Before applying the lattice-matched DBRs into the μLED, it is necessary to first conduct a detailed investigation into the DBRs – in terms of their material quality, reflectivity and centre wavelength. First, a standard two-step GaN with a thickness of 1.5 μm is grown on *c*-plane sapphire by MOCVD, followed by 11 pairs of alternating high-doped n-GaN (silicon-doped) and undoped GaN (u-GaN) layers. The doping level of high-doped n-GaN is normally higher than $5 \times 10^{19}/cm^3$. Figure 5.1 displays a typical growth reflectivity of the DBR template as measured by the LayTec EpiCurve TT in-situ monitoring system. The estimated growth rate is 0.767 nm/s. All high-doped n-GaN and undoped GaN layers of DBRs are grown under 175 torr at 1150 °C with a TMGa flow rate of 65 sccm and NH_3 flow rate of 3000 sccm. Additionally, by involving a small fraction of Al in the high-doped n-GaN to form high-doped n-$Al_{0.01}Ga_{0.99}N$, it is possible to further enhance the material quality and optical performance of DBRs.[14]

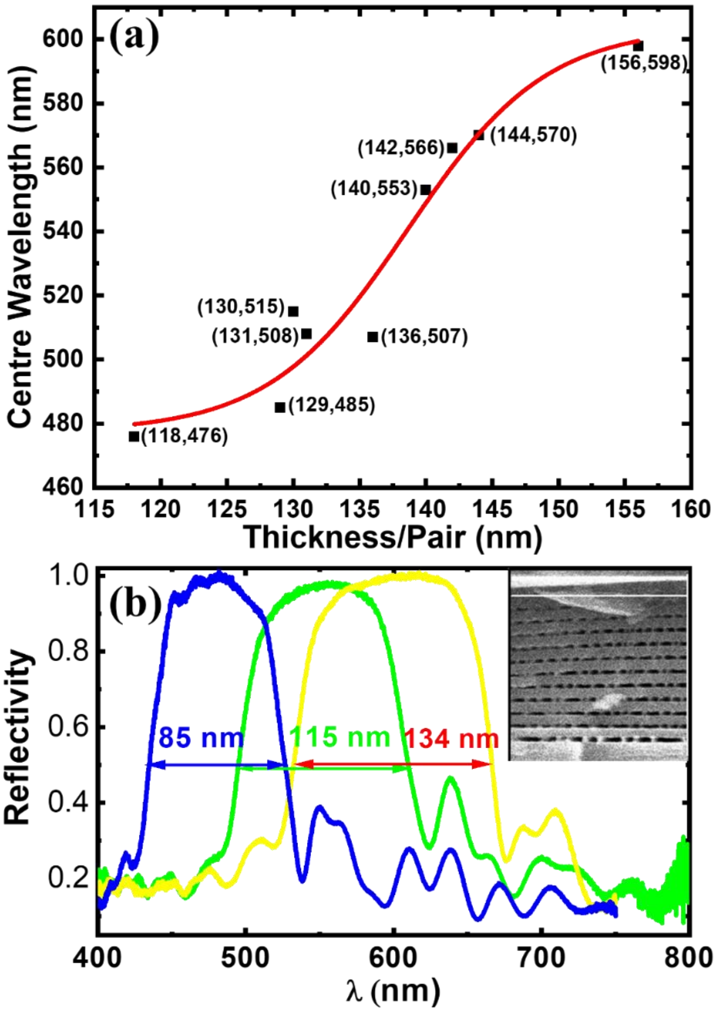

Figure 5.2. *(a) Reflectivity centre wavelength of NP-GaN/undoped GaN DBRs as a function of thickness per pair. (b) Reflective spectra of three NP-GaN/undoped GaN*

DBRs with high reflectivity above 96% covered from blue to amber region. Inset: Cross-sectional SEM image of NP-GaN/u-GaN DBRs for blue.

After growth, to form NP-GaN/u-GaN DBRs, a standard EC etching process was applied on the as-grown DBR samples, which were etched in 0.5 M nitric acid at 8 V bias with the GaN sample as an anode and a Pt plate as a cathode. The mechanism of EC etching is a combination of an oxidation process and a dissolution process under anodic bias.[15] Thus, the high-doped n-GaN layers with a doping density of around 5×10^{20} /cm^3 are etched, after which they become NP-GaN. Because of the high refractive index difference between NP-GaN and undoped GaN, 11 pairs of NP-GaN/u-GaN layers can form a lattice-matched DBR structure.

Figure 5.2a illustrates the relationship between the reflectivity centre wavelength of NP-GaN/undoped GaN DBRs and the thickness per pair. The EC etching conditions for all samples are identical. It is evident that, with the increase of total thickness per pair, the DBR reflectivity centre wavelength can be tuned from 476 nm to 598 nm, covering a wide spectral region from blue to red. The reflectance spectra of three DBRs in this experiment are shown in Figure 5.2b; the three DBRs show high reflectivity in excess of 96% and broad stopbands of 85 nm, 115 nm and 134 nm, respectively. The inset SEM image taken at high magnification also clearly indicates the periodical NP-GaN and undoped GaN for blue DBRs.

5.2.2 Epitaxial Growth and Characterisation of Integrated µLEDs with DBRs

Figure 5.3a indicates the integration of µLEDs and DBRs. After the growth of 11 pairs of high-doped n-GaN and undoped GaN layers, 600 nm standard n-GaN with a doping level of 5×10^{18}/cm^3 is further grown to make an as-grown template. Afterward, 500 nm SiO_2 is deposited on the top of n-GaN by PECVD. Then, standard photolithography and ICP dry-etching processes are applied to selectively etch SiO_2 and form µLED templates. Identically to the μLEDs illustrated in the last chapter, these μLEDs have a diameter of 3.6 μm and an interpitch of 2 μm.

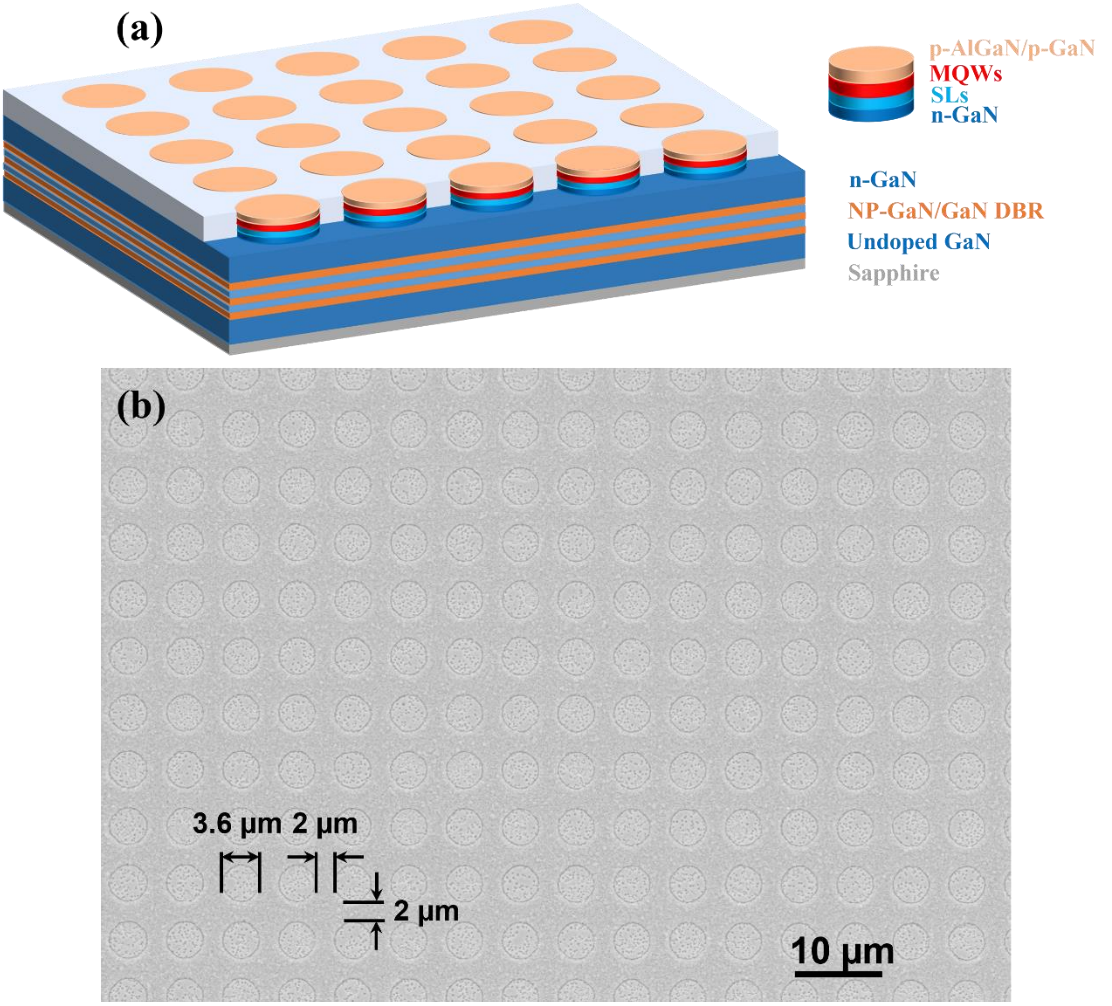

Figure 5.3. *(a) Schematic illustration of μLEDs integrated with DBRs. (b) Top-view SEM image of μLED wafer.*

After the cleaning processes, a standard III-nitride-based LED structure is overgrown on the pre-patterned template by MOCVD. First, 50 nm standard n-GaN is grown, followed by 30 periods of InGaN/GaN superlattices (SLS) with an indium composition of 5.5% and a total thickness of 198 nm (6.6 nm/period). Then, five periods of MQWs with a quantum well thickness of 2.5 nm and barrier thickness of 13.5 nm are grown as the active region. The details of SLS and MQWs are provided by the XRD omega-2theta measurements and fitting results, which are shown in Figure 5.4. Finally, 20 nm p-$Al_{0.2}Ga_{0.8}N$ EBL and 180 nm p-GaN are grown. The total growth thickness is approximately 500 nm, which is similar to the SiO_2 deposition thickness.

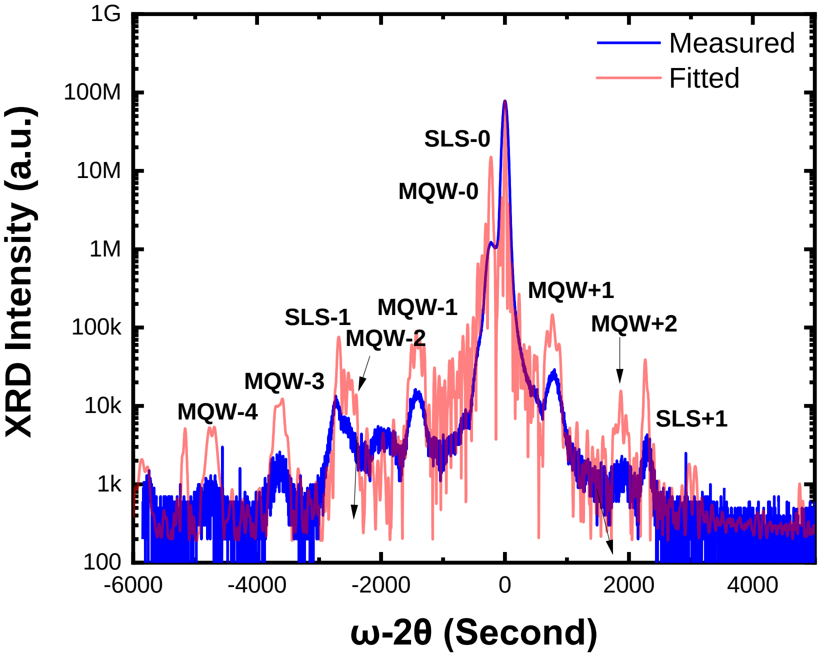

Figure 5.4. HRXRD omega-2theta measurement and fitting results.

Through the confined selective epitaxy technique, the growth of LED structure is restricted within the patterned area, forming μLED arrays naturally. Thus, all physical parameters – such as shape, diameter, interpitch and location – are entirely determined and controlled by the patterned SiO_2 mask. Figure 5.3b shows the SEM image of the μLED wafer. It is clear that all μLED arrays have a regular circular shape, a uniform diameter of 3.6 μm, and an identical interpitch of 2 μm. Moreover, our μLED arrays are totally compatible with the current pick-and-place technique.[16] They can also be integrated with transistors to achieve active-matrix switching, making them ideal for microdisplay applications. [17]

Afterward, the EC etching in 0.5 M nitric acid at 8 V bias is applied on the μLED wafer to form NP-GaN/u-GaN DBRs. During the EC etching, only high-doped n-GaN in

DBRs is etched and converted into NP-GaN, whereas the standard n-GaN is not etched because of the lower level of silicon doping. The cross-sectional SEM images of μLED wafers after EC etching are displayed in Figure 5.5. Eleven pairs of NP-GaN/u-GaN DBRs structure with a designed centre wavelength of 500 nm are observed.

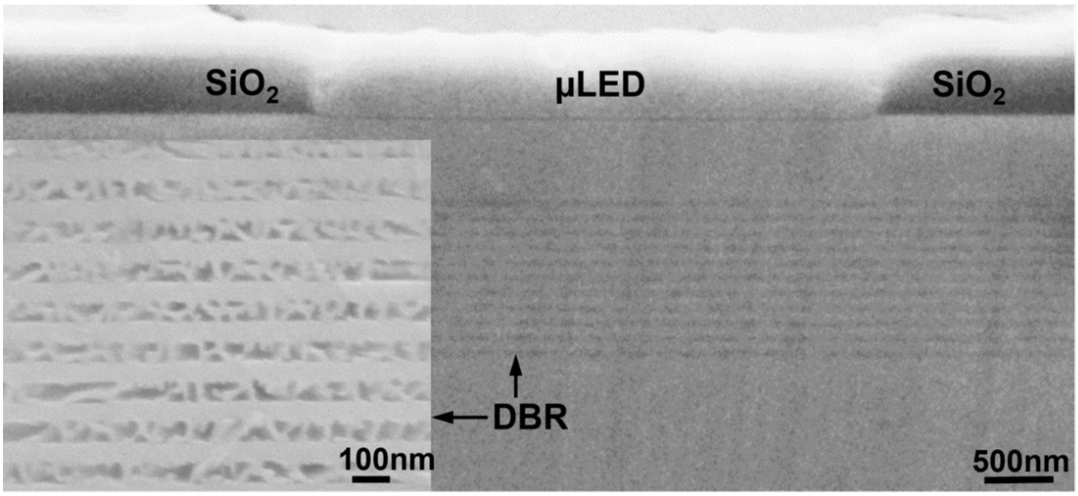

Figure 5.5. *Cross-sectional SEM images of μLEDs integrated with DBRs after EC etching.*

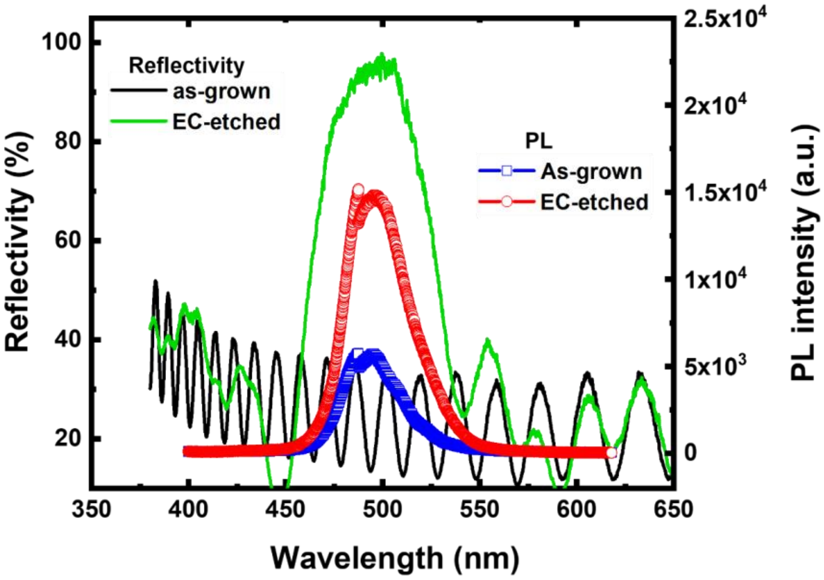

Figure 5.6. *Reflectance spectra and PL spectra of as-grown μLEDs and EC-etched μLEDs.*

The reflectance spectra of both as-grown µLEDs (without DBRs) and EC-etched µLEDs (with DBRs) are shown in Figure 5.6, which clearly shows that the DBRs exhibit a centre wavelength of 500 nm and high reflectivity of 97%, as designed. The photoluminescence (PL) measurements are also involved in comparing the optical performance of µLEDs, both with and without DBRs. A 375 nm laser diode is used as an excitation source, and a Horiba SPEX 500M monochromator is used to disperse the emission. The emission is then detected by an air-cooled CCD and transferred to the computer. As shown in Figure 5.6, compared with µLEDs without DBRs, the PL intensity of µLEDs with DBRs is 2.5 times that of µLEDs without DBRs – a dramatic increase. Thus, the DBRs below µLEDs can effectively enhance extraction efficiency.

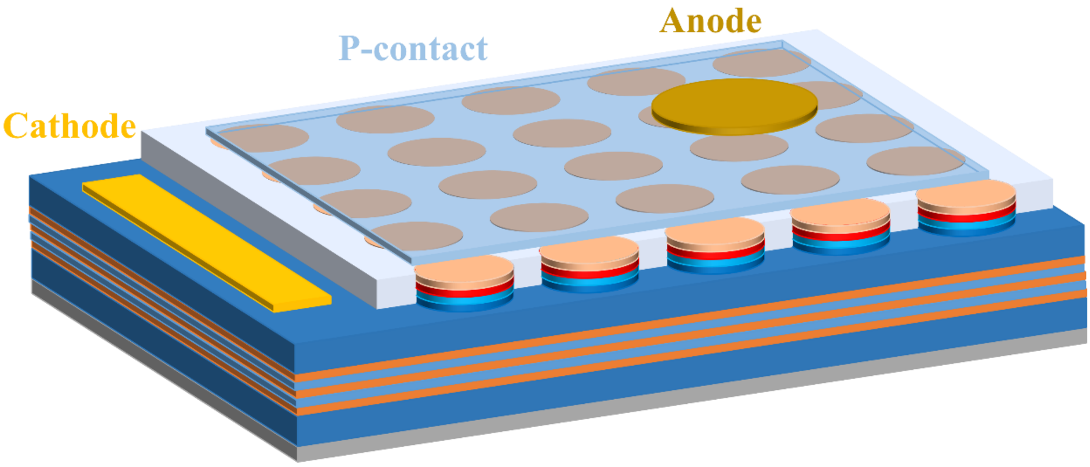

Figure 5.7. *Schematic of µLED device integrated with DBR.*

Afterward, as seen in Figure 5.7, µLED wafers – both with and without DBRs – are fabricated into µLED devices with a standard area of 330 × 330 µm in the same batch to make a comparison. Each µLED device contains thousands of µLED pixels. The transparent p-contact is formed by the deposition of indium tin oxide (ITO), followed by a 1-minute annealing process in the air at 600 °C. The n-contact is fabricated by Ti/Al/Ni/Au alloys; Ti/Au alloys are used to fabricate the anode and cathode.

The microscope images of the µLEDs with DBRs at an injection current density of 15 A/cm^2 are taken by a micro-electroluminescence (EL) system designed with two objective lenses. One is 10× magnification with a numerical aperture of 0.28; the other is 50× magnification with a numerical aperture of 0.43. Figures 5.8a and 5.8b, respectively, show the images taken by these two lenses. Clearly, the μLEDs with DBRs exhibit very bright emissions under a low injecting current density. It is worth mentioning that the typical injection current density of broad-area LEDs is 22 A/cm^2, which is higher than these μLEDs. Therefore, the lifetime of these μLEDs is expected to be at least same as conventional broad-area LEDs (typically over 100,000 h under normal operating conditions).[16] However, further characterisations about the lifetime of our μLEDs need to be done in the future to confirm this.

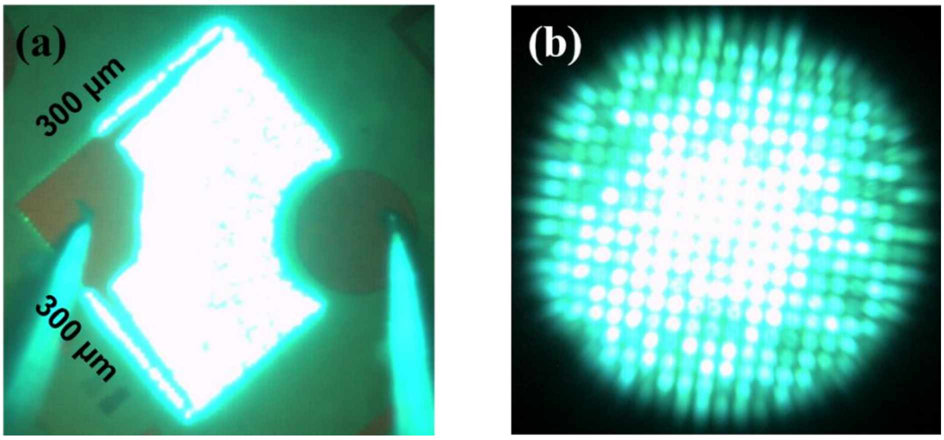

Figure 5.8. *(a) EL microscope image of the μLEDs with DBRs at an injection current density of 15 A/cm^2 under low magnification. (b) EL microscope image of the μLEDs with DBRs at an injection current density of 15 A/cm^2 under high magnification.*

The EL spectra of the μLEDs without DBRs and the μLEDs with DBRs under different injection currents are illustrated in Figures 5.9a and 5.9b. All measurements are taken in a continuous wave (CW) mode at room temperature. The corresponding injection current density ranges from 15 to 300 A/cm^2. Both devices display a strong single green emission at 500 nm. The EL intensity also increased with the increase of injection current. It is clear that the spectral line width – also known as the full-width at half-maximum (FWHM) – of μLEDs with DBRs is narrower than that of μLEDs without DBRs.

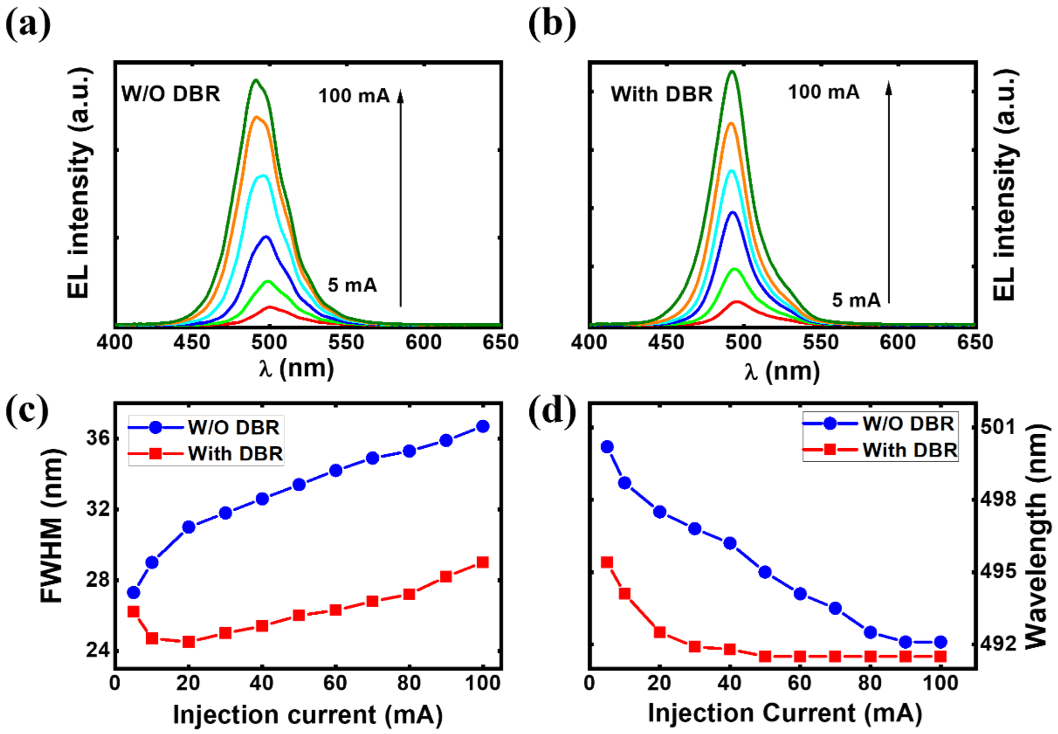

Figure 5.9. *EL spectra of the μLEDs (a) without and (b) with DBRs, both measured as a function of injection current from 5 mA to 100 mA at room temperature. (c) The FWHM of EL spectra for both devices as a function of injection current. (d) Peak emission wavelength of both devices as a function of injection current.*

The accurate FWHM values of the EL spectra for μLEDs with and without DBRs are summarised in Figure 5.9c. Clearly, compared with μLEDs without DBRs, there is a significant reduction of FWHM value when DBRs are employed below μLEDs. In detail, at an injection current of 20 mA, the FWHM of μLEDs with DBRs is only 25 nm, whereas this value rises to 31 nm for μLEDs without DBRs. With the added increase of injection current, the FWHM values of both devices are clearly increased. This phenomenon is frequently observed in III-nitride-based LEDs and is caused by the band filling effect.[18] When the injection current is raised to 100 mA, the μLEDs without DBRs exhibit a broad FWHM of 37 nm, and the FWHM is further reduced to 29 nm when DBRs are utilised.

The EL wavelengths of μLED devices with and without DBRs as a function of injection current are shown in Figure 5.9d. Both samples show a blue shift in terms of emission wavelength with the increase of injection current. This phenomenon is caused by the reduction of the quantum-confined Stark effect (QCSE) generated by the internal electric field.[19,20] Because the relaxation time of carriers is much higher than the lifetime of carriers, the number of free carriers in the active region is increased with the increase of injection current, thereby reducing the internal electric field. Consequently, the QCSE is decreased, leading to an increase in bandgap energy and a blue shift of emission wavelength. It is worth highlighting that the blue shift of μLEDs with DBRs is only 3.4 nm when the injection current is increased from 5 mA to 100 mA, whereas the blue shift of μLEDs without DBRs is 8.7 nm. One potential explanation is that the formation of NP-DBRs underneath may slightly relieve the strain in the active region, leading to a slight decrease in QCSE. A reduction of reflectivity of DBRs at edge wavelength might also contribute to this phenomenon.

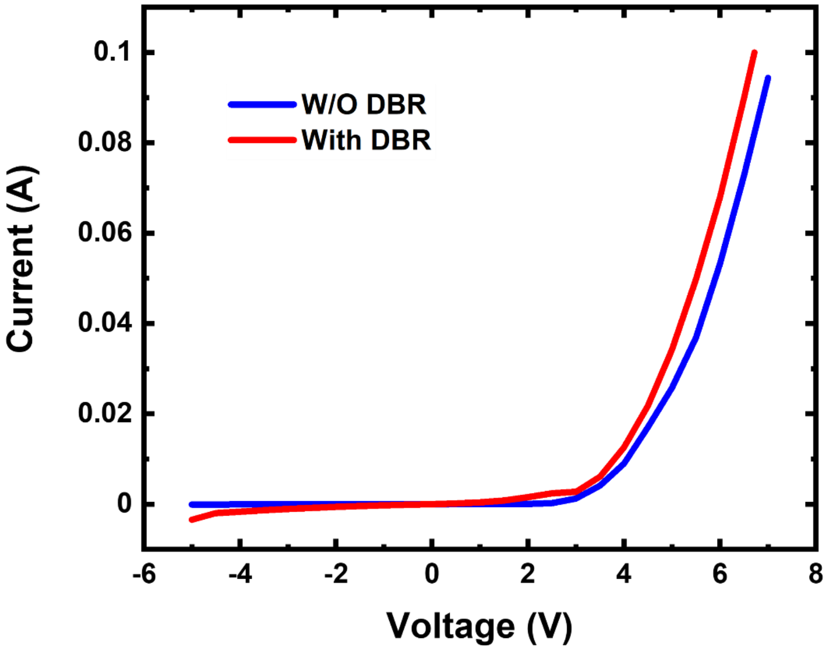

Figure 5.10. *I–V characterisation of μLEDs with and without DBRs.*

Figure 5.10 illustrates the current–voltage (I–V) curves of both μLED devices. The turn-on voltages of both devices are very similar. Meanwhile, both devices also present similar I–V curves without any breakdown at -4 V. Under forward bias, the μLEDs with

DBRs exhibit an injection current of 20 mA at 3.5 V, which is similar to that of conventional broad-area III-nitride-based LEDs. Under a reverse bias of 4 V, the leakage current is only 2.8 μA, corresponding to a leakage current density of 0.01 A/cm^2.

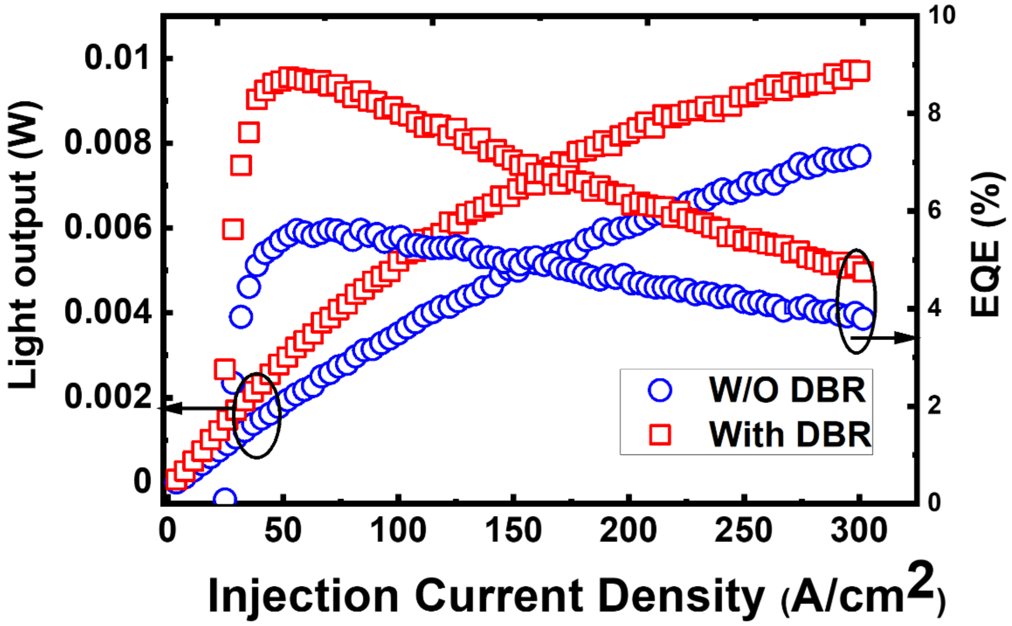

__Figure 5.11.__ Light output power and EQE of μLEDs with and without DBRs.

The light output power and EQE of μLEDs with and without DBRs as a function of injection current density are shown in Figure 5.11. The light output power of μLEDs with DBRs is much higher than that of μLEDs without DBRs. In detail, the light output power is μLEDs with DBRs is 2.0 mW at injection current density of 33 A/cm^2, but only 1.2 mW light output power is generated by μLEDs without DBRs at the same current density. This shows that the NP-DBRs provide a 67% enhancement in light output power. As shown in Figure 5.11, the EQE of both μLEDs devices is initially increased with the increase of injection current density; however, with further increases of injection current density, EQE begins to fall. This is commonly known as ‘efficiency droop’, which is a very common phenomenon in III-nitride-based LEDs. It is worth highlighting that the maximum EQE of μLEDs with DBRs is around 9% at an injection current density of 33 A/cm^2, which is 50% higher than that of μLEDs without DBRs (peak EQE ~6%). This is also attributed to the utilisation of DBRs. The highest EQE of green μLEDs with a diameter less than 5 μm reported from other groups before this work is only 5.8%. The efficiency droop of the μLEDs with DBRs is larger than μLEDs without DBRs. This may be caused by the low thermal dispersion of NP-DBRs due the air in voids. This is a potential issue which may also reduce the lifetime of our μLEDs.

5.3 Summary

In conclusion, we have demonstrated III-nitride-based μLEDs achieved by a confined selective epitaxy combined with epitaxial lattice-matched NP-GaN/u-GaN DBRs underneath, which exhibit narrow spectral line width and high EQE for microdisplay applications. The μLEDs (with a diameter of 3.6 μm and interpitch of 2 μm) with DBRs exhibit a narrow spectral line width of 25 nm, which is the narrowest reported value in the area of III-nitride-based μLEDs. The EQE of μLEDs is also enhanced from 6% to 9% by applying the NP-GaN/u-GaN DBRs underneath.

Reference

1. Duxbury, N.; Bangert, U.; Dawson, P.; Thrush, E. J.; Van der Stricht, W.; Jacobs, K.; Moerman, I. Indium Segregation in InGaN Quantum-Well Structures. *Applied Physics Letters* **2000**, *76* (12), 1600–1602.

2. Dmukauskas, M.; Mickevičius, J.; Dobrovolskas, D.; Kadys, A.; Nargelas, S.; Tamulaitis, G. Correlation between Growth Interruption and Indium Segregation in InGaN MQWs. *Journal of Luminescence* **2020**, *221*, 117103.

3. Soltani Vala, A.; Godfrey, M. J.; Dawson, P. Effects of Indium Segregation and Well-Width Fluctuations on Optical Properties of InGaN/GaN Quantum Wells. *physica status solidi (b)* **2001**, *228* (2), 453–456.

4. Bai, J.; Cai, Y.; Feng, P.; Fletcher, P.; Zhao, X.; Zhu, C.; Wang, T. A Direct Epitaxial Approach to Achieving Ultrasmall and Ultrabright InGaN Micro Light-Emitting Diodes (MLEDs). *ACS Photonics* **2020**, *7* (2), 411–415.

5. Nakada, N.; Nakaji, M.; Ishikawa, H.; Egawa, T.; Umeno, M.; Jimbo, T. Improved Characteristics of InGaN Multiple-Quantum-Well Light-Emitting Diode by GaN/AlGaN Distributed Bragg Reflector Grown on Sapphire. *Applied Physics Letters* **2000**, *76* (14), 1804–1806.

6. Waldrip, K. E.; Han, J.; Figiel, J. J.; Zhou, H.; Makarona, E.; Nurmikko, A. V. Stress Engineering during Metalorganic Chemical Vapor Deposition of AlGaN/GaN Distributed Bragg Reflectors. *Applied Physics Letters* **2001**, *78* (21), 3205–3207.

7. Yeh, P. S.; Yu, M.-C.; Lin, J.-H.; Huang, C.-C.; Liao, Y.-C.; Lin, D.-W.; Fan, J.-R.; Kuo, H.-C. GaN-Based Resonant-Cavity LEDs Featuring a Si-Diffusion-Defined Current Blocking Layer. *IEEE Photonics Technology Letters* **2014**, *26* (24), 2488–2491.

8. Lin, C. F.; Yao, H. H.; Lu, J. W.; Hsieh, Y. L.; Kuo, H. C.; Wang, S. C. Characteristics of Stable Emission GaN-Based Resonant-Cavity Light-Emitting Diodes. *Journal of Crystal Growth* **2004**, *261* (2-3), 359–363.

9. Huang, G. S.; Lu, T. C.; Yao, H. H.; Kuo, H. C.; Wang, S. C.; Lin, C.-W.; Chang, L. Crack-Free GaN⁄AlN Distributed Bragg Reflectors Incorporated with GaN⁄AlN Superlattices Grown by Metalorganic Chemical Vapor Deposition. *Applied Physics Letters* **2006**, *88* (6), 061904.

10. Wu, C. M.; Zhang, B. P.; Shang, J. Z.; Cai, L. E.; Zhang, J. Y.; Yu, J. Z.; Wang, Q. M. High-Reflectivity AlN/GaN Distributed Bragg Reflectors Grown on Sapphire Substrates by MOCVD. *Semiconductor Science and Technology* **2011**, *26* (5), 055013.

11. Park, J.; Kang, J.-H.; Ryu, S.-W. High Diffuse Reflectivity of Nanoporous GaN Distributed Bragg Reflector Formed by Electrochemical Etching. *Applied Physics Express* **2013**, *6* (7), 072201.

12. Shiu, G.-Y.; Chen, K.-T.; Fan, F.-H.; Huang, K.-P.; Hsu, W.-J.; Dai, J.-J.; Lai, C.-F.; Lin, C.-F. InGaN Light-Emitting Diodes with an Embedded Nanoporous GaN Distributed Bragg Reflectors. *Scientific Reports* **2016**, *6* (1).

13. Zhang, C.; Park, S. H.; Chen, D.; Lin, D.-W.; Xiong, W.; Kuo, H.-C.; Lin, C.-F.; Cao, H.; Han, J. Mesoporous GaN for Photonic Engineering—Highly Reflective GaN Mirrors as an Example. *ACS Photonics* **2015**, *2* (7), 980–986.

14. Tian, Y.; Feng, P.; Zhu, C.; Chen, X.; Xu, C.; Esendag, V.; Martinez de Arriba, G.; Wang, T. Nearly Lattice-Matched GaN Distributed Bragg Reflectors with Enhanced Performance. *Materials* **2022**, *15* (10), 3536.

15. Schwab, M. J.; Chen, D.; Han, J.; Pfefferle, L. D. Aligned Mesopore Arrays in GaN by Anodic Etching and Photoelectrochemical Surface Etching. *The Journal of Physical Chemistry C* **2013**, *117* (33), 16890–16895.

16. Lee, V. W.; Twu, N.; Kymissis, I. Micro-LED Technologies and Applications. *Information Display* **2016**, *32* (6), 16–23.

17. Day, J.; Li, J.; Lie, D. Y. C.; Bradford, C.; Lin, J. Y.; Jiang, H. X. III-Nitride Full-Scale High-Resolution Microdisplays. *Applied Physics Letters* **2011**, *99* (3), 031116.

18. Ju, Z. G.; Liu, W.; Zhang, Z.-H.; Tan, S. T.; Ji, Y.; Kyaw, Z. B.; Zhang, X. L.; Lu, S. P.; Zhang, Y. P.; Zhu, B. B.; Hasanov, N.; Sun, X. W.; Demir, H. V. Improved Hole Distribution in InGaN/GaN Light-Emitting Diodes with Graded Thickness Quantum Barriers. *Applied Physics Letters* **2013**, *102* (24), 243504.

19. Takeuchi, T.; Sota, S.; Katsuragawa, M.; Komori, M.; Takeuchi, H.; Amano, H.; Akasaki, I. Quantum-Confined Stark Effect due to Piezoelectric Fields in GaInN Strained Quantum Wells. *Japanese Journal of Applied Physics* **1997**, *36* (Part 2, No. 4A), L382–L385.

20. Bai, J.; Xu, B.; Guzman, F. G.; Xing, K.; Gong, Y.; Hou, Y.; Wang, T. (11-22) Semipolar InGaN Emitters from Green to Amber on Overgrown GaN on Micro-Rod Templates. *Applied Physics Letters* **2015**, *107* (26), 261103.

Chapter 6

Direct Epitaxial Growth to Achieving Ultrasmall (2 μm) III-Nitride Micro-LEDs in the Red Spectral Region

The microdisplays for augmented reality (AR) and virtual reality (VR) require ultrasmall micro light-emitting-diodes (μLEDs) with a dimension of ≤5 μm. Furthermore, such microdisplays also require three types of ultrasmall μLEDs (i.e. emitting red, green and blue) for full-colour display. Currently, in addition to posing a great challenge for achieving ultrasmall μLEDs based mainly on III-nitride semiconductors, another fundamental barrier is the extreme difficulty of growing III-nitride-based red LEDs. So far, no effective approach has been developed for obtaining high-indium-content InGaN as an active region required for a red LED while also preserving high optical performance.

In this chapter, we have demonstrated a confined selective epitaxy growth approach using a template that features microhole arrays. This approach allows us to not only obtain the natural formation of ultrasmall μLEDs, but also to achieve InGaN with enhanced indium content at an elevated growth temperature (at which it is impossible to obtain InGaN-based red LEDs on a standard planar surface). Via this approach, we have demonstrated red μLEDs (at an emission wavelength of 642 nm) with a dimension of 2 μm, exhibiting a high luminance of 3.5×10^7 cd/m^2 and a peak external quantum efficiency of 1.75% measured in a wafer form (i.e. without any packaging to enhance an extraction efficiency). In contrast, an LED grown under identical growth conditions, but on a standard planar surface, shows green emission at 538 nm. This highlights that our approach provides a simple solution that can address the two major challenges mentioned above.

6.1 Introduction

There is growing interest in developing microdisplays with compact screens of ≤1/4″ diagonal length, which have a wide range of applications in smart watches, smart phones, smart bands, AR, and VR devices.[1–5] Their individual pixel elements typically consist of a large number of visible microscale LEDs based mainly on III-nitride semiconductors, which are referred to as 'micro-LEDs' (μLEDs). For instance, the microdisplays for AR and VR require μLEDs with an ultrasmall dimension of ≤5 μm.[6–8] Such devices are typically utilised in scenarios where space is highly limited, or when the devices must be close to users' eyes. Therefore, such devices require high resolution, high contrast ratio, high luminance and high EQE.[9,10] Of course, a microdisplay needs three kinds of individual μLEDs as a single pixel each emitting red, green, and blue emission (i.e., RGB), respectively.

InGaN semiconductors have direct bandgaps across their entire composition, ranging from 0.7 eV for InN to 3.43 eV for GaN; these cover part of the infrared region, all of the visible spectrum, and part of the ultraviolet (UV) region. So far, InGaN-based μLEDs with reasonably good performance in the blue and green spectral region have been reported. However, red LEDs still rely on AlGaInP materials. Although a large-area AlGaInP red LED with a high efficiency (>50%) can be achieved,[11] the efficiency falls dramatically when its dimension is reduced to the microscale, namely, μLEDs. This is due to an enhancement in the surface recombination rate and the long carrier diffusion lengths.[12–15] Moreover, the efficiency of AlGaInP red LEDs is sensitive to their junction temperature,[16,17] and thus, AlGaInP red LEDs generally suffer from a severe leakage current at a high temperature, generating a severe efficiency thermal drop. All these fundamental issues indicate that it is indispensable to develop III-nitride-based red LEDs to meet the requirements for the fabrication of a full-colour microdisplay.

InGaN with high indium content (>20%) is necessary for obtaining long-wavelength emission. Unfortunately, it is very challenging to achieve high-indium-content InGaN while preserving high optical performance.[18,19] A typical method for achieving high indium content in InGaN is to lower the growth temperature for InGaN. However, this method is not ideal because it causes a significant degradation in crystal quality.

In general, vapour−solid thermodynamic equilibrium can be modified by stress, causing the solid-phase epitaxial composition to reduce toward lattice-matched conditions. This is the main reason why it is so difficult to increase indium incorporation into GaN.[20−24] Therefore, the growth of InGaN on a relaxed layer is beneficial for obtaining high indium content in InGaN. However, it must be borne in mind that the formation of a relaxed layer is often associated with the generation of extra defects if a heterostructure with a large lattice mismatch is used to generate a relaxed layer, which leads to degradation in optical performance. Furthermore, the stress status of an underlying layer plays a critical role in determining indium incorporation into GaN. In general, tensile stress tends to enhance indium incorporation into GaN, offering a unique advantage for growing red LEDs on silicon substrates as GaN grown on Si suffering tensile stress.[25,26] In contrast, GaN grown on sapphire substrates exhibits compressive strain.

The growth of InGaN-based red LEDs has been reported by means of inserting a thin AlN or AlGaN layer into each InGaN quantum well as an emitting region, leading to an enhancement in strain that pushes the emission wavelength of InGaN quantum wells toward longer wavelength.[27,28] That approach has become a popular method for the growth of long-wavelength emitters, especially red LEDs.[25−30] Furthermore, by combining the idea of inserting a thin AlN or AlGaN layer and further adjusting the in-plane strain of a GaN template by tuning the GaN thickness, 633 nm-wavelength red LEDs with an EQE of 1.6% have been reported in which an extremely thick GaN (8−10 μm) template has been employed.[26,29] A more recent report has shown that a peak EQE as high as 4.5% has been achieved on red InGaN μLEDs, albeit with a large dimension

($60 \times 60\ \mu m^2$).[31] However, it is worth noting that the approach based on enhanced strain also leads to a reduction in internal quantum efficiency.

We expect that an enhanced strain relaxation can be achieved by using confined selective epitaxy growth on a microhole-patterned template – which we have developed recently – where in μLEDs can be formed naturally without employing any dry-etching techniques, because confined selective epitaxy growth can take place only within these microholes.[7,8] In this work, we are proposing to employ this approach to achieve ultrasmall red μLED arrays with enhanced quantum efficiency, but without inserting any thin AlN or AlGaN into InGaN quantum wells as an emitting region. It is expected that no lateral confinement during the selective epitaxy growth process and it will effectively and naturally lead to strain relaxation. By this mechanism, 642 nm red μLEDs with a dimension of 2 μm have been achieved by our confined selective epitaxy growth conducted at an elevated temperature, at which a red LED cannot be achieved on a standard planar GaN surface. The resultant EQE is 1.75%. For comparison, only 538 nm green LEDs on a standard planar GaN template can be obtained, even under identical growth conditions. Our X-ray diffraction measurements have confirmed that a significant enhancement in indium content in InGaN has been achieved by our approach.

6.2 Experiment and Discussion

6.2.1 Comparative Study of Epitaxial Growth on a Planar Template and a Patterned Template

In this work, two different InGaN-based LED samples have been designed and then grown, aiming to study the influence of confined selective epitaxial growth on the optical performance of III-nitride LEDs grown on a pre-patterned template featuring microhole arrays. A μLED array sample is obtained by our confined selective epitaxy growth on the pre-patterned n-GaN template, as mentioned above, and is denoted as

LED A. The other one is a normal LED sample grown under identical growth conditions but on a standard planar n-GaN template without any features, and is denoted as LED B.

Figure 6.1a shows the schematics of our confined selective epitaxy growth approach, allowing us to naturally achieve μLED arrays without involving any dry-etching process (i.e. LED A). Silicon-doped n-GaN epiwafers are first grown on *c*-plane (0001) sapphire substrates using the standard two-step approach by a MOCVD technique. Initially, a 25 nm GaN nucleation layer is prepared at a low temperature after the substrate has been subjected to a thermal annealing process at a high temperature of 1150 °C, followed by a 1 μm GaN buffer layer, and then another 500 nm silicon-doped n-GaN layer – both grown at a high temperature of 1120 °C. For LED A, the n-GaN template is further patterned into microhole arrays using SiO_2 masks on its top, which is then used as a pre-patterned template for our selective epitaxial growth.

A 500 nm SiO2 dielectric film is deposited on the n-GaN template by a PECVD technique, followed by standard photolithography and then a dry-etching technique to selectively etch the SiO2 dielectric layer down to the n-GaN surface by inductively coupled plasma (ICP), thereby forming regularly arrayed microholes with a diameter of 2 μm and an interpitch of 1.5 μm. This pre-patterned template is then used for further selective epitaxy growth. Finally, selective growth takes place only within SiO2 microhole regions, naturally forming regularly arrayed μLEDs.

Afterward, a standard III-nitride LED structure is selectively grown on the micropatterned template by MOCVD. In detail, a silicon-doped n-GaN layer is first prepared, followed by an $In_{0.05}Ga_{0.95}N$/GaN superlattice (SLS) structure as a pre-layer, five periods of InGaN/GaN MQWs as an emitting region, then a 20 nm p-type $Al_{0.2}Ga_{0.8}N$ as an electron-blocking layer (EBL), and a final 150 nm p-type GaN layer. The total thickness of the overgrown layers is 500 nm, which matches the thickness of the SiO_2 masks. Due to the SiO_2 masks, the growth of the LED structure occurs only within the microholes, thus naturally forming regularly arrayed µLEDs.

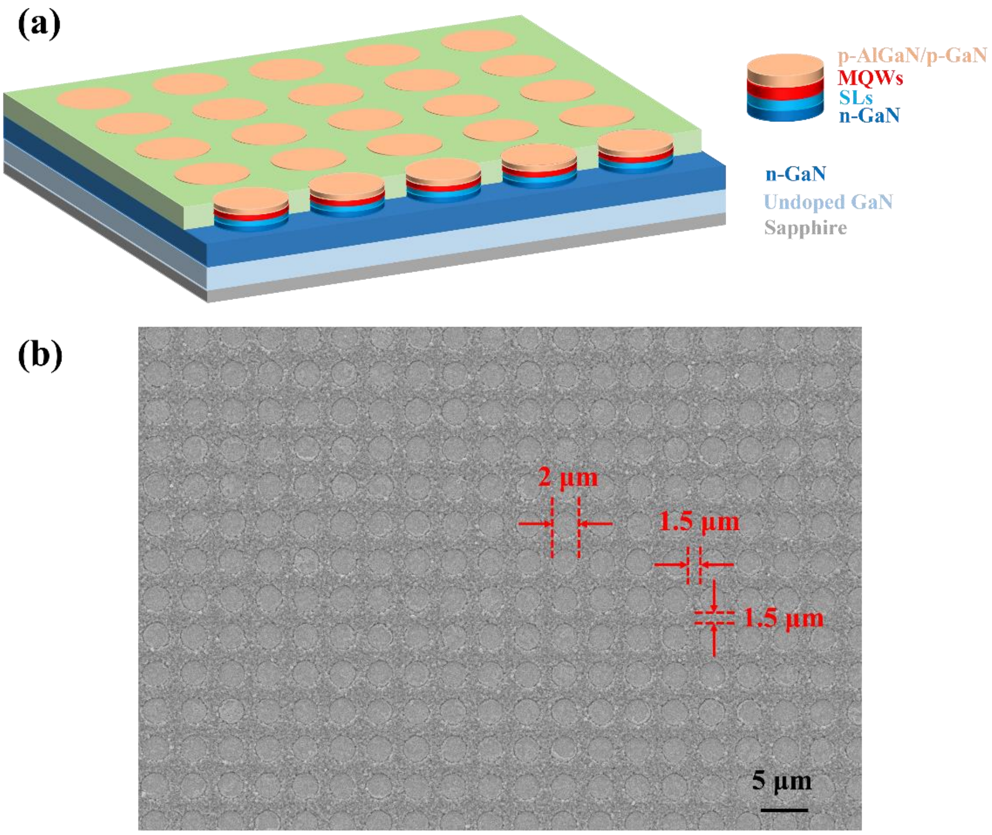

Figure 6.1. *(a) Schematic of selective epitaxy growth and (b) plan-view SEM image for the µLED array epiwafer (LED A), showing a diameter of 2 µm and an interpitch of 1.5 µm.*

6.2.2 Investigation of the Mechanism for Enhanced Indium Incorporation on a Patterned Template

A Raith 150 scanning electron microscopy (SEM) system has been used to characterise the surface morphology of our regularly arrayed µLEDs. Figure 6.1b shows a typical plan-view SEM image of our regularly arrayed µLEDs wafer (i.e. LED A), exhibiting a ideal circular shape with excellent uniformity in shape, diameter and interpitch. All µLEDs are 2 µm in diameter and only 1.5 µm in interpitch. Such a small diameter and an interpitch are crucial for manufacturing a high-resolution microdisplay in a compact manner. Furthermore, the µLED pixels share a common n-contact, whereas all the p-contacts are left open. As a result, our regularly arrayed μLED epiwafers well-match all existing techniques for manufacturing microdisplays, such as the widely used pick-and-place technology as well as the integrating technique using driving transistors based on the silicon CMOS IC to achieve individually addressable μLED-based microdisplays.[32,33]

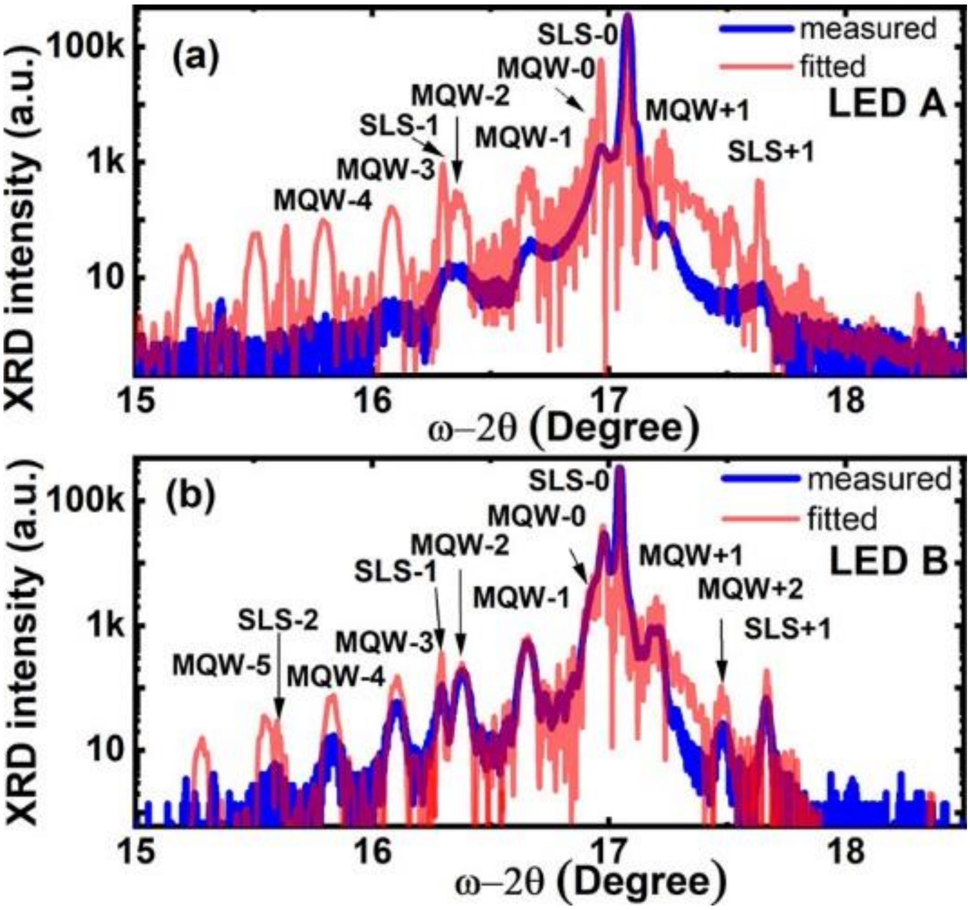

Figure 6.2. *HRXRD ω-2θ scan curves of the μLED array sample on a patterned template, i.e. (a) LED A, and the LED sample grown on a standard planar template, i.e. (b) LED B under identical conditions. Fittings have also been provided to determine the indium content in InGaN MQWs.*

A high-resolution X-ray diffractometer (HRXRD) (Bruker D8) has been employed to determine the indium content of the InGaN MQWs by performing ω-2θ scan measurements along the (002) direction, together with a fitting using the Bruker JV-RADS simulation software. Figures 6.2a and 6.2b shows the HRXRD ω-2θ scan curves of our regularly arrayed μLED wafer (i.e. LED A) and the standard LED wafer (i.e. LED B), respectively. In both cases, satellite peaks with up to four or five orders from the InGaN/GaN MQWs have been clearly observed. Satellite peaks from the SLS structure as a pre-layer have also been observed. Based on a detailed fitting, it can be determined that the indium content of the InGaN MQWs of LED A is 31% and that the thicknesses of the InGaN quantum well and the barrier are 2.2 and 13.8 nm, respectively. In contrast, LED B exhibits 24% indium content in the InGaN MQWs with a 2.6 nm quantum well and a 14.1 nm barrier. The fitting results have some uncertainties, because only total thickness of 1 pair QW and QB can be calculated from the XRD omega-twotheta curve. However, the accurate thickness can be measured by transmission electorn microscopy (TEM) in the future to investigate the QW and QB thickness and then we can get the accurate indium composition. The XRD fittings are conducted based on fully strained InGaN MQWs for both LEDs. It is well known that strain relaxation will reduce the strain-induced QCSE, leading to a blue shift in the emission, which means that if the InGaN MQWs are assumed to be strain-relaxed, the indium content should be higher still. In consideration of a higher chance of strain relaxation for the μLEDs, the fitted values of indium contents represent the least difference between the two LEDs. This direct comparison indicates that enhancing the indium content in InGaN MQWs can be obtained by using our selective epitaxy growth approach on a prepatterned template featuring microhole arrays.

Finally, both the regularly arrayed μLED wafer (i.e. LED A) and the standard LED wafer (i.e. LED B) have been fabricated into LED devices with an area of 330 × 330 μm^2. ITO is deposited and then undergoes an annealing process in air at 600 °C for 1 minute, forming transparent p-type contact, while Ti/Al/Ni/Au alloys are prepared as n-type contact. Ti/Au alloys are used as p-type and n-type electrodes.

For LED A, each LED device consists of several thousand connected 2 μm μLEDs. In this work, the μLEDs in LED A share a common p-contact and n-contact, which are driven simultaneously in all electroluminescence (EL) measurements. However, it is worth noting that our arrayed μLEDs are designed to make the p-contacts of each μLED left open, providing an opportunity in the future to allow indium bumps to be bonded to active-matrix driving transistors. This means that our regularly arrayed μLED structure completely matches any existing approach for the fabrication of individually addressable μLED microdisplays. For a direct comparison, the LED B wafer has also been processed under identical conditions in the same batch. All the characteristics of our μLED chips in the present study are conducted on bare chips – that is, with no coating, no passivation, no epoxy and no reflector, which are often used to obtain enhanced extraction efficiency. Current−voltage (I−V) characteristic and EL measurements have been performed at room temperature in a CW mode using a Keithley 2400 SourceMeter on a probe station equipped with an optical microscopy system.

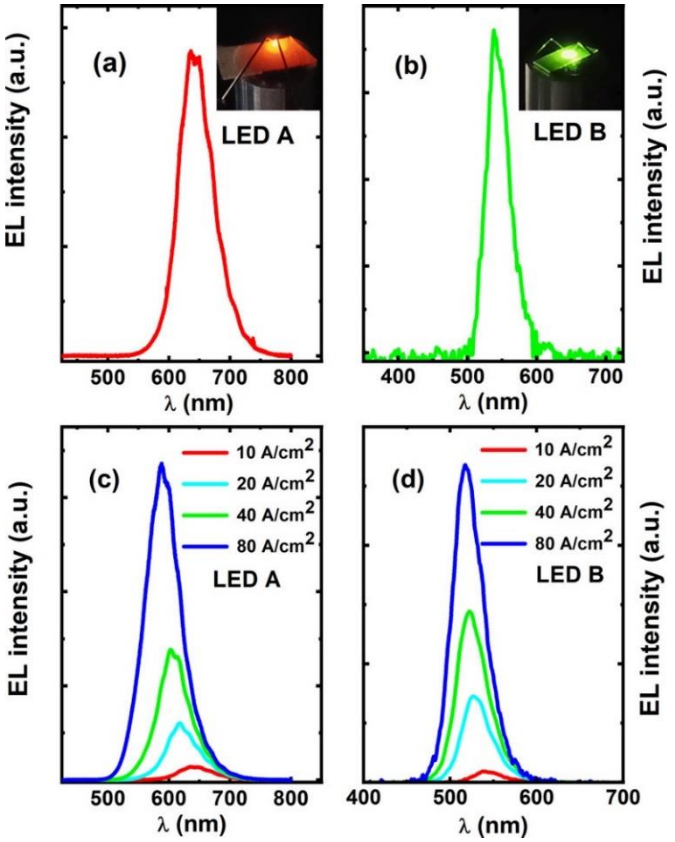

Figure 6.3. *EL spectra measured at 10 A/cm^2 for the μLED array device, i.e. (a) LED A and (b) LED B, where the insets show their respective emission images. EL spectra*

measured at increased current densities from 10 to 80 A/cm^2 for (c) LED A and (d) LED B, respectively.

The EL spectra have been measured on the two LED devices under identical conditions in order to facilitate a direct comparison. For instance, Figures 6.3a and b show the EL spectra of two LED devices, both measured at a current density of 10 A/cm^2. Both spectra exhibit a single emission peak. The μLED array device shows a strong emission at an emission wavelength of 642 nm in the red spectral region. The inset of Figure 6.3a exhibits an emission image of the μLED array chip, indicating red light. In contrast, Figure 6.3b displays a strong green emission at 538 nm from the LED B device, also measured at 10 A/cm^2, and the inset displays its emission image. This means that the selective epitaxial growth on a prepatterned template featuring regularly arrayed microholes results in a red shift of approximately 100 nm in emission wavelength, in comparison with the LED grown on a standard planar GaN surface, although both are grown under identical growth conditions. As discussed previously, the growth of InGaN on a relaxed layer is beneficial for obtaining high indium content in InGaN. Because there is no lateral confinement during the overgrowth within the microholes, the overgrown n-GaN is very likely strain-relaxed, which leads to an enhancement of the indium content in the overlying InGaN MQWs. Combined with the XRD results, it has been confirmed that our selective epitaxy growth approach can significantly enhance indium incorporation into GaN. Figures 6.3c and d show the EL spectra of LED A and LED B, both of which are measured as a function of injection current density ranging from 10 to 80 A/cm^2.

Figures 6.4a, b and c display the emission images of our μLED array chip taken under 4, 8, and 12 A/cm^2 current densities, respectively, while Figures 6.4d, e and f provide their corresponding emission images taken under high magnification, showing strong red emissions from individual 2 μm μLED pixels, even under low current densities. It is worth mentioning that such low current densities used for the operation of our μLEDs are lower than a typical current density (22 A/cm^2) for the operation of a conventional broad-area LED.

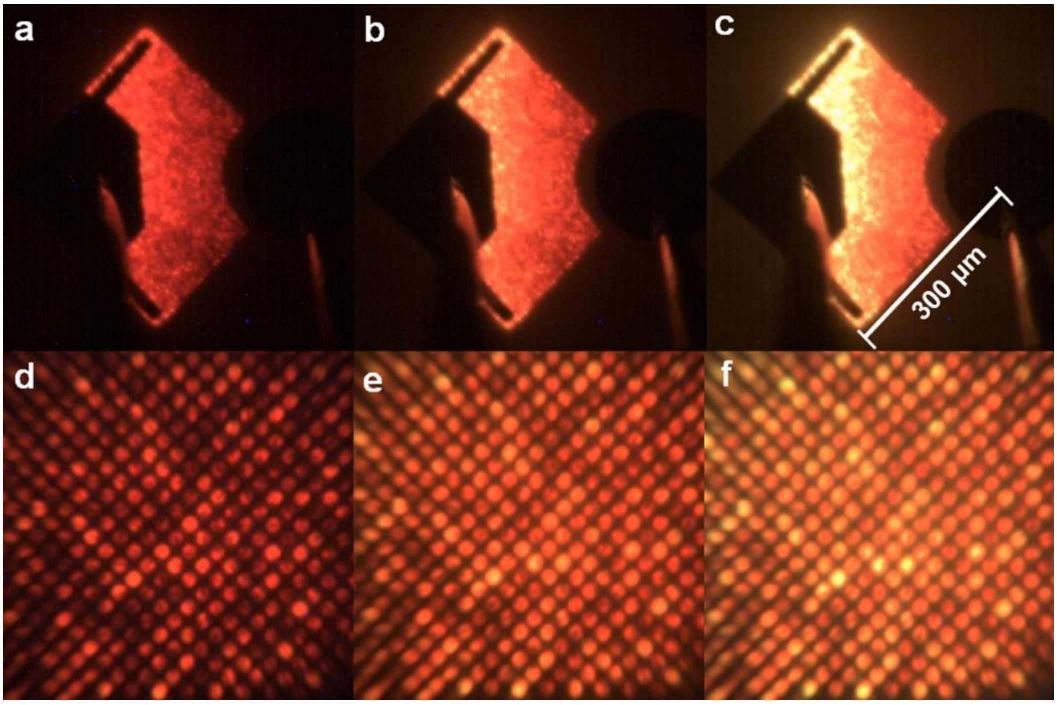

__Figure 6.4.__ Emission images of the μLED array device taken using an optical microscopy system as a function of injection current density (4, 8 and 12 A/cm^2) at low magnification (a−c) and high magnification (d−f), respectively.

Both light output power and luminous flux have been measured on the bare-chip LEDs bonded on TO5-headers in CW mode using an LCS-100 integrating sphere equipped with a CCD APRAR spectrometer. Figures 6.5a, b and c show the output power, luminance, and EQE of the μLED array device (i.e. LED A), respectively, as a function of injection current density. This shows that the output power and luminescence increase monotonically with increasing current density up to 450 A/cm^2 and that a high luminance of 3.5 × 10^7 cd/m^2 has been achieved. The peak EQE is approximately 1.75%. It is worth highlighting that although no heat-sink components are used, our ultrasmall μLEDs can still sustain a high current density above 450 A/cm^2, which also confirms the high crystal quality of our μLED array sample achieved by our selective epitaxy growth approach. Figure 6.5d displays the typical I−V characteristics of LED A measured as a function of bias, which is similar to that of the LED B device. This also shows the good electrical property of our μLED array device.

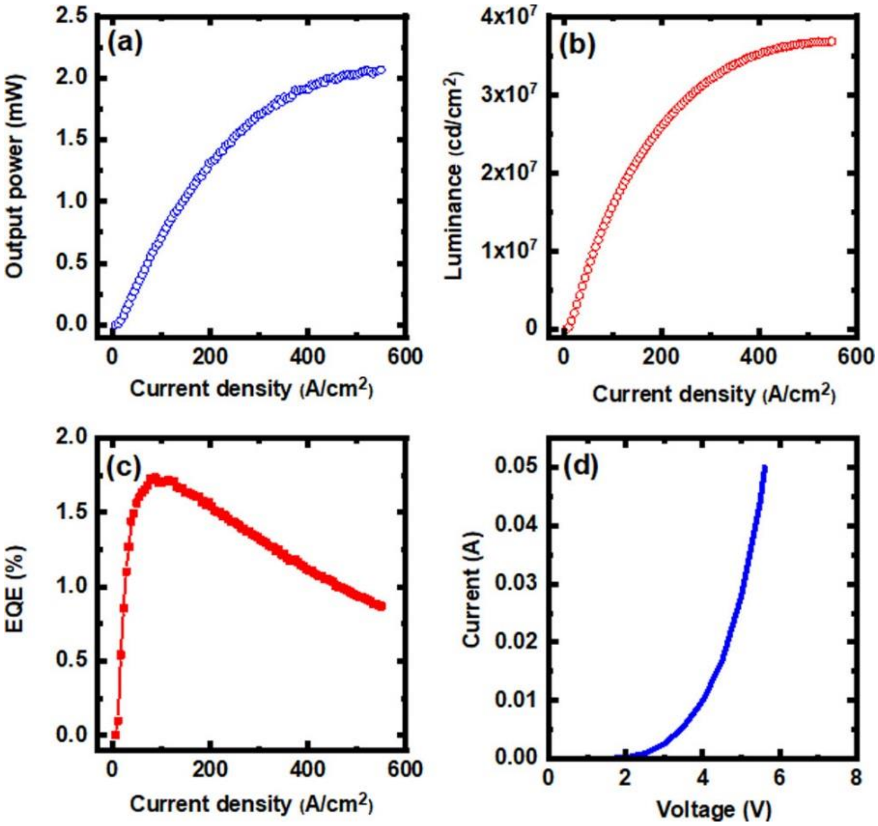

Figure 6.5. *(a) Output power, (b) luminance, (c) EQE, and (d) current−voltage characteristics of the μLED array device (i.e. LED A).*

6.3 Conclusions

In summary, we are proposing to employ a confined selective epitaxy growth approach on a microhole-patterned template to significantly enhance strain relaxation, allowing us to not only obtain the natural formation of regularly arrayed μLEDs, but also to achieve enhanced indium content in the InGaN/GaN MQWs used as an active region for the μLEDs. Via this approach, we have demonstrated red InGaN-based μLED arrays with a dimension of 2 μm and an interpitch of 1.5 μm. A high luminance of 3.5×10^7 cd/m^2 and a peak EQE of 1.75% have been achieved for the red μLED array chip in a wafer form without any packaging. In contrast, the standard LED grown under identical conditions – but on a standard planar GaN template – shows green emission. With this contribution, our approach paves the way toward achieving long-wavelength InGaN-based μLEDs with ultrasmall dimensions at an elevated growth temperature, at which it is impossible to obtain InGaN-based red LEDs on a standard planar template.

References

1. Meng, W.; Xu, F.; Yu, Z.; Tao, T.; Shao, L.; Liu, L.; Li, T.; Wen, K.; Wang, J.; He, L.; Sun, L.; Li, W.; Ning, H.; Dai, N.; Qin, F.; Tu, X.; Pan, D.; He, S.; Li, D.; Zheng, Y. Three-Dimensional Monolithic Micro-LED Display Driven by Atomically Thin Transistor Matrix. *Nature Nanotechnology* **2021**, *16* (11), 1231–1236.

2. Park, J.; Choi, J. H.; Kong, K.; Han, J. H.; Park, J. H.; Kim, N.; Lee, E.; Kim, D.; Kim, J.; Chung, D.; Jun, S.; Kim, M.; Yoon, E.; Shin, J.; Hwang, S. Electrically Driven Mid-Submicrometre Pixelation of InGaN Micro-Light-Emitting Diode Displays for Augmented-Reality Glasses. *Nature Photonics* **2021**, *15* (6), 449–455.

3. Huang, Y.; Hsiang, E.-L.; Deng, M.-Y.; Wu, S.-T. Mini-LED, Micro-LED and OLED Displays: Present Status and Future Perspectives. *Light: Science & Applications* **2020**, *9* (1).

4. Han, H.-V.; Lin, H.-Y.; Lin, C.-C.; Chong, W.-C.; Li, J.-R.; Chen, K.-J.; Yu, P.; Chen, T.-M.; Chen, H.-M.; Lau, K.-M.; Kuo, H.-C. Resonant-Enhanced Full-Color Emission of Quantum-Dot-Based Micro LED Display Technology. *Optics Express* **2015**, *23* (25), 32504.

5. Green, R. P.; McKendry, J. J. D.; Massoubre, D.; Gu, E.; Dawson, M. D.; Kelly, A. E. Modulation Bandwidth Studies of Recombination Processes in Blue and Green InGaN Quantum Well Micro-Light-Emitting Diodes. *Applied Physics Letters* **2013**, *102* (9), 091103.

6. Ley, R. T.; Smith, J. M.; Wong, M. S.; Margalith, T.; Nakamura, S.; DenBaars, S. P.; Gordon, M. J. Revealing the Importance of Light Extraction Efficiency in InGaN/GaN MicroLEDs via Chemical Treatment and Dielectric Passivation. *Applied Physics Letters* **2020**, *116* (25), 251104.

7. Bai, J.; Cai, Y.; Feng, P.; Fletcher, P.; Zhao, X.; Zhu, C.; Wang, T. A Direct Epitaxial Approach to Achieving Ultrasmall and Ultrabright InGaN Micro Light-Emitting Diodes (μLEDs). *ACS Photonics* **2020**, *7* (2), 411–415.

8. Bai, J.; Cai, Y.; Feng, P.; Fletcher, P.; Zhu, C.; Tian, Y.; Wang, T. Ultrasmall, Ultracompact and Ultrahigh Efficient InGaN Micro Light Emitting Diodes (μLEDs) with Narrow Spectral Line Width. *ACS Nano* **2020**, *14* (6), 6906–6911.

9. Zhan, T.; Yin, K.; Xiong, J.; He, Z.; Wu, S.-T. Augmented Reality and Virtual Reality Displays: Perspectives and Challenges. *iScience* **2020**, *23* (8), 101397.

10. Liu, Z.; Lin, C.-H.; Hyun, B.-R.; Sher, C.-W.; Lv, Z.; Luo, B.; Jiang, F.; Wu, T.; Ho, C.-H.; Kuo, H.-C.; He, J.-H. Micro-Light-Emitting Diodes with Quantum Dots in Display Technology. *Light: Science & Applications* **2020**, *9* (1), 83.

11. Krames, M. R.; Ochiai-Holcomb, M.; Höfler, G. E.; Carter-Coman, C.; Chen, E. I.; Tan, I.-H. .; Grillot, P.; Gardner, N. F.; Chui, H. C.; Huang, J.-W. .; Stockman, S. A.; Kish, F. A.; Craford, M. G.; Tan, T. S.; Kocot, C. P.; Hueschen, M.; Posselt, J.; Loh, B.; Sasser, G.; Collins, D. High-Power Truncated-Inverted-Pyramid $(Al_xGa_{1-X})_{0.5}In_{0.5}P/GaP$ Light-Emitting Diodes Exhibiting >50% External Quantum Efficiency. *Applied Physics Letters* **1999**, *75* (16), 2365–2367.

12. Boroditsky, M.; Gontijo, I.; Jackson, M.; Vrijen, R.; Yablonovitch, E.; Krauss, T.; Cheng, C.-C.; Scherer, A.; Bhat, R.; Krames, M. Surface Recombination Measurements on III–v Candidate Materials for Nanostructure Light-Emitting Diodes. *Journal of Applied Physics* **2000**, *87* (7), 3497–3504.

13. Royo, P.; Stanley, R. P.; Ilegems, M.; Streubel, K.; Gulden, K. H. Experimental Determination of the Internal Quantum Efficiency of AlGaInP Microcavity Light-Emitting Diodes. *Journal of Applied Physics* **2002**, *91* (5), 2563–2568.

14. Oh, J.-T.; Lee, S.-Y.; Moon, Y.-T.; Moon, J. H.; Park, S.; Hong, K. Y.; Song, K. Y.; Oh, C.; Shim, J.-I.; Jeong, H.-H.; Song, June-O.; Amano, H.; Seong, T.-Y. Light Output Performance of Red AlGaInP-Based Light Emitting Diodes with Different Chip Geometries and Structures. *Optics Express* **2018**, *26* (9), 11194–11200.

15. Wong, M. S.; Kearns, J. A.; Lee, C.; Smith, J. M.; Lynsky, C.; Lheureux, G.; Choi, H.; Kim, J.; Kim, C.; Nakamura, S.; Speck, J. S.; DenBaars, S. P. Improved Performance of AlGaInP Red Micro-Light-Emitting Diodes with Sidewall Treatments. *Optics Express* **2020**, *28* (4), 5787.

16. adav, A.; Titkov, I. E.; Sokolovskii, G. S.; Karpov, S. Yu.; Dudelev, V. V.; Soboleva, K. K.; Strassburg, M.; Pietzonka, I.; Lugauer, H.-J.; Rafailov, E. U. Temperature Effects on Optical Properties and Efficiency of Red AlGaInP-Based Light Emitting Diodes under High Current Pulse Pumping. *Journal of Applied Physics* **2018**, *124* (1), 013103.

17. Oh, C.-H.; Shim, J.-I.; Shin, D.-S. Current- and Temperature-Dependent Efficiency Droops in InGaN-Based Blue and AlGaInP-Based Red Light-Emitting Diodes. *Japanese Journal of Applied Physics* **2019**, *58* (SC), SCCC08.

18. El-Masry, N. A.; Piner, E. L.; Liu, S. X.; Bedair, S. M. Phase Separation in InGaN Grown by Metalorganic Chemical Vapor Deposition. *Applied Physics Letters* **1998**, *72* (1), 40–42.

19. Wakahara, A.; Tokuda, T.; Dang, X.-Z.; Noda, S.; Sasaki, A. Compositional Inhomogeneity and Immiscibility of a GaInN Ternary Alloy. *Applied Physics Letters* **1997**, *71* (7), 906–908.

20. Inatomi, Y.; Kangawa, Y.; Ito, T.; Suski, T.; Kumagai, Y.; Kakimoto, K.; Koukitu, A. Theoretical Study of the Composition Pulling Effect in InGaN Metalorganic

Vapor-Phase Epitaxy Growth. *Japanese Journal of Applied Physics* **2017**, *56* (7), 078003.

21. Wang, T. Topical Review: Development of Overgrown Semi-Polar GaN for High Efficiency Green/Yellow Emission. *Semiconductor Science and Technology* **2016**, *31* (9), 093003.

22. Pereira, S.; Correia, M. R.; Pereira, E.; O'Donnell, K. P.; Alves, E.; Sequeira, A. D.; Franco, N.; Watson, I. M.; Deatcher, C. J. Strain and Composition Distributions in Wurtzite InGaN/GaN Layers Extracted from X-Ray Reciprocal Space Mapping. *Applied Physics Letters* **2002**, *80* (21), 3913–3915.

23. Shimizu, M.; Kawaguchi, Y.; Hiramatsu, K.; Sawaki, N. Metalorganic Vapor Phase Epitaxy of Thick InGaN on Sapphire Substrate. *Japanese Journal of Applied Physics* **1997**, *36* (Part 1, No. 6A), 3381–3384.

24. Sonderegger, S.; Feltin, E.; Merano, M.; Crottini, A.; Carlin, J. F.; Sachot, R.; Deveaud, B.; Grandjean, N.; Ganière, J. D. High Spatial Resolution Picosecond Cathodoluminescence of InGaN Quantum Wells. *Applied Physics Letters* **2006**, *89* (23), 232109.

25. Tawfik, W. Z.; Hyun, G. Y.; Ryu, S.-W.; Ha, J. S.; Lee, J. K. Piezoelectric Field in Highly Stressed GaN-Based LED on Si (1 1 1) Substrate. *Optical Materials* **2016**, *55*, 17–21.

26. Iida, D.; Zhuang, Z.; Kirilenko, P.; Velazquez-Rizo, M.; Ohkawa, K. High-Color-Rendering-Index Phosphor-Free InGaN-Based White Light-Emitting Diodes by Carrier Injection Enhancement via V-Pits. *Applied Physics Letters* **2020**, *117* (17), 172103.

27. Hwang, J.-I.; Hashimoto, R.; Saito, S.; Nunoue, S. Development of InGaN-Based Red LED Grown on (0001) Polar Surface. *Applied Physics Express* **2014**, *7* (7), 071003.

28. Hashimoto, R.; Hwang, J.; Saito, S.; Nunoue, S. High-Efficiency Yellow Light-Emitting Diodes Grown on Sapphire (0001) Substrates. *physica status solidi (c)* **2014**, *11* (3-4), 628–631.

29. Zhuang, Z.; Iida, D.; Ohkawa, K. InGaN-Based Red Light-Emitting Diodes: From Traditional to Micro-LEDs. *Japanese Journal of Applied Physics* **2021**, *61* (SA), SA0809.

30. Li, P.; Li, H.; Zhang, H.; Lynsky, C.; Iza, M.; Speck, J. S.; Nakamura, S.; DenBaars, S. P. Size-Independent Peak External Quantum Efficiency (>2%) of InGaN Red Micro-Light-Emitting Diodes with an Emission Wavelength over 600 Nm. *Applied Physics Letters* **2021**, *119* (8), 081102.

31. Li, P.; Li, H.; Zhang, H.; Yang, Y.; Wong, M. S.; Lynsky, C.; Iza, M.; Gordon, M. J.; Speck, J. S.; Nakamura, S.; DenBaars, S. P. Red InGaN Micro-Light-Emitting Diodes (>620 Nm) with a Peak External Quantum Efficiency of 4.5% Using an Epitaxial Tunnel Junction Contact. *Applied Physics Letters* **2022**, *120* (12), 121102.

32. Day, J.; Li, J.; Lie, D. Y. C.; Bradford, C.; Lin, J. Y.; Jiang, H. X. III-Nitride Full-Scale High-Resolution Microdisplays. *Applied Physics Letters* **2011**, *99* (3), 031116.

Chapter 7

Conclusion and Future Work

This thesis has presented ultrasmall, high-efficient and high-brightness III-nitride green μLEDs with a diameter of 3.6 µm, which were achieved via a novel confined selective epitaxy technology. Moreover, by employing an epitaxial DBR structure comprising 11 periods of nanoporous GaN/un-doped GaN underneath, the green μLEDs have demonstrated a much narrower spectral width as well as enhanced EQE and output power than μLEDs without DBRs. Furthermore, ultrasmall red μLEDs with a 2 µm diameter have been achieved by means of enhanced indium incorporation (due to the increased strain relaxation) during the confined selective epitaxy. These achievements contribute a novel method by which full-colour microdisplay, integrated on a single wafer, may be achieved in the future.

7.1 Conclusion

7.1.1 Direct Epitaxy to Achieve Green μLEDs

First, a confined selective epitaxy of LED structures on prepatterned GaN templates, as well as corresponding patterned template designs, were investigated and optimised, leading to the successful achievement of green μLEDs with a dimension of 3.6 μm and an interpitch of 2 μm. This technology totally eliminated the etching damages associated with traditional μLED fabrication processes, resulting in reduced non-radiative recombination rate and enhanced optical efficiency. The TDPL results indicated that green μLEDs with an IQE of 28% had been achieved directly via confined selective epitaxy. Moreover, green μLED devices exhibited a high luminance of 1×10^7 cd/m^2 and a high EQE of 6% at 515 nm.

7.1.2 Direct Epitaxy to Integrate Green μLEDs with DBRs

In order to form an epitaxial GaN DBR, a GaN structure composed of multiple periods of highly doped n-GaN as well as undoped GaN was investigated. The highly doped n-GaN layers became nanoporous through EC etching, leading to the formation of a nanoporous GaN (NP-GaN)/GaN DBR. By optimising the EC etching conditions and tuning the thicknesses of each layer in the DBR period, the centre wavelength could be adjusted from 476 nm to 598 nm, covering a broad spectral region from blue to red. A nanoporous DBR structure with a centre wavelength of 500 nm was integrated below the green μLEDs in Chapter 4, exhibiting a narrow spectral line width of 25 nm and an enhanced EQE of 9%, while those of the μLEDs without DBRs were 31 nm and 6%, respectively. These results showed that the employment of the DBRs underneath μLEDs can effectively enhance the optical performance of μLEDs.

7.1.3 Direct Epitaxy to Achieve Red μLEDs with Enhanced Indium Content

Ultrasmall red μLEDs with a dimension of 2 μm and an interpitch of 1.5 μm have been achieved by confined selective epitaxy technology in this study. Because there is no lateral confinement during the confined selective epitaxy, the overgrown n-GaN is nearly strain-relaxed and the indium composition in InGaN MQWs is significantly increased. This was supported by comparison with a planar LED grown under the same MOCVD growth conditions. The XRD ω-2θ scan curves indicate that the InGaN MQWs of μLEDs have a high indium content of 31%, and the planar sample is only 24%. As for EL measurements, the planar LED exhibits a strong green emission at 538 nm, while the emission wavelength of μLEDs is 642 nm. A high luminance of 3.5×10^7 cd/m^2 and a high EQE of 1.75% have been obtained for the bare red μLEDs.

7.2 Future Work

To further enhance the EQE of red μLEDs, high-reflectivity nanoporous DBRs with a centre wavelength of >600 nm will be integrated into our current red μLEDs. Moreover, the structure of MQWs active region can be further optimised. First, an AlGaN interlayer would be utilised because it has been shown to be effective by other groups. Second, the thermal annealing of quantum wells may also enhance optical performance. Finally, hybrid MQWs which consist of blue QWs and red QWs in the active region merit further investigation.

It has been shown that the confined selective epitaxy of μLEDs on prepatterned templates favours indium incorporation in InGaN MQWs. In theory, by tuning the dimension of μLEDs, the indium composition may be adjusted, thereby altering emission wavelength. Generally, smaller μLEDs have longer emission wavelength. The relationship between indium composition and μLED dimension would be investigated in the future to achieve RGB full-colour μLED display. The diameter of μLEDs could be further reduced to 1 μm to achieve higher resolution for microdisplays.

Appendix

Figure 1. *Gas circuit of Thomas Swan MOCVD system.*